ULTRASONIC ACOUSTIC WAVE DETECTION OF SINGLE OR CAPILLARY ELECTROPHORETICALLY RESOLVED UNDERIVATIZED AMINO ACIDS

by

Wa Lok (Jacky) Chou
B.Sc., Simon Fraser University, 2003

THESIS SUBMITTED IN PARTIAL FULFILLMENT OF
THE REQUIREMENTS FOR THE DEGREE OF

MASTER OF SCIENCE

In the Department of Chemistry

© Wa Lok (Jacky) Chou 2007

SIMON FRASER UNIVERSITY

Summer 2007

All rights reserved. This work may not be
reproduced in whole or in part, by photocopy
or other means, without permission of the author.

APPROVAL

Name: Wa Lok(Jacky) Chou

Degree: Master of Science

Title of Thesis: Ultrasonic Acoustic Wave Detection of Single or Capillary Electrophoretically Resolved Underivatized Amino Acids

Examining Committee:

Dr. Vance E. Williams
Chair
Assistant Professor, Department of Chemistry

Dr. Paul C.H. Li
Senior Supervisor
Associate Professor, Department of Chemistry

Dr. Michael E. Hayden
Supervisor
Associate Professor, Department of Physics

Dr. Gary W. Leach
Supervisor
Associate Professor, Department of Chemistry

Dr. Hua-Zhong(Hogan) Yu
Internal Examiner
Associate Professor, Department of Chemistry

Date Approved: May 3, 2007

SFU SIMON FRASER UNIVERSITY
LIBRARY

Declaration of Partial Copyright Licence

The author, whose copyright is declared on the title page of this work, has granted to Simon Fraser University the right to lend this thesis, project or extended essay to users of the Simon Fraser University Library, and to make partial or single copies only for such users or in response to a request from the library of any other university, or other educational institution, on its own behalf or for one of its users.

The author has further granted permission to Simon Fraser University to keep or make a digital copy for use in its circulating collection (currently available to the public at the "Institutional Repository" link of the SFU Library website <www.lib.sfu.ca> at: <http://ir.lib.sfu.ca/handle/1892/112>) and, without changing the content, to translate the thesis/project or extended essays, if technically possible, to any medium or format for the purpose of preservation of the digital work.

The author has further agreed that permission for multiple copying of this work for scholarly purposes may be granted by either the author or the Dean of Graduate Studies.

It is understood that copying or publication of this work for financial gain shall not be allowed without the author's written permission.

Permission for public performance, or limited permission for private scholarly use, of any multimedia materials forming part of this work, may have been granted by the author. This information may be found on the separately catalogued multimedia material and in the signed Partial Copyright Licence.

While licensing SFU to permit the above uses, the author retains copyright in the thesis, project or extended essays, including the right to change the work for subsequent purposes, including editing and publishing the work in whole or in part, and licensing other parties, as the author may desire.

The original Partial Copyright Licence attesting to these terms, and signed by this author, may be found in the original bound copy of this work, retained in the Simon Fraser University Archive.

Simon Fraser University Library
Burnaby, BC, Canada

Revised: Summer 2007

ABSTRACT

Acoustic wave detection of various underivatized amino acids that were injected into and electrokinetically migrated along a capillary tube has been achieved. Acoustic wave detection of underivatized leucine was obtained in the ultrasonic frequency range of 100 kHz - 20 MHz. This was accomplished by measuring the insertion loss from the vector ratio of the signal voltage to the source voltage obtained at the generating and receiving piezoelectric transducers. Linear concentration dependence of the insertion loss of underivatized leucine was established. The effects of capillary internal diameter, capillary geometry (square/circular), buffer composition and acoustic wave frequency on the insertion loss were investigated. Subsequently, separations of underivatized amino acids (leucine/histidine, and leucine/tryptophan) were performed under different buffer conditions and different capillary geometry. The principle of acoustic wave detection will be discussed.

ACKNOWLEDGEMENTS

I offer my enduring gratitude to the faculty, staff and my fellow students at the SFU Department of Chemistry, who have combined to create a stimulating synergy for research in our field. I would like to thank my senior supervisor, Dr. Paul C. H. Li, for the opportunity to work in his research group. Throughout my research project, he provided innovative ideas, directions and guidance for difficulties encountered. I would like to thank my supervisory committee member, Dr. Gary Leach and Dr. Mike Hayden for their helpful discussions and suggestions.

Thanks to my lab mates James Li, Leon Wang, Dr. Larry Peng, Michael Sung, Wei Xiao, Dr. Hong Chen and Dr. Te-Chun Wu for their ideas, suggestions and friendships. Thanks to Dr. Zuo-Guang Ye and Mr. Bill Woods for gold sputtering on pinducer surfaces.

Special thanks are owed to my parents, whose support throughout my education years has been unbroken, and multi-faceted.

Thanks to SFU for financial support.

TABLE OF CONTENTS

LIST OF FIGURES

Chapter 1

Chapter 2

Chapter 3

Chapter 4

Chapter 5

Chapter 6

LIST OF TABLES

Chapter 2

Chapter 5

LIST OF PLATES

LIST OF ABBREVIATIONS

α	ultrasonic absorption coefficient
α_{cl}	classical ultrasonic absorption coefficient
α_{ex}	excess ultrasonic absorption coefficient
α_l	liquid ultrasonic absorption coefficient
α_s	solid ultrasonic absorption coefficient
χ	particle displacement
ε_o	vacuum permittivity
ε	relative permittivity
ϕ	acoustic phase
κ_s	liquid bulk modulus
λ	wavelength
ν	acoustic wave velocity
ν_S	solid-state acoustic wave velocity
ν_L	liquid-state acoustic wave velocity
ν_{EOF}	electro-osmotic velocity
ν_{EPF}	electrophoretic velocity
ν_{total}	sum of ν_{EOF} and ν_{EP}
ρ	density of sample
ρ_s	density of solid
τ	relaxation time
ω	angular frequency
ξ	extent of reaction
ζ	zeta potential
f	frequency
f_r	relaxation frequency
$\Im$	transmission coefficient
$\Re$	reflection coefficient
η	viscosity
σ	conductivity
ψ	dielectric constant of the buffer
A_o	maximum particle displacement
A	unattenuated amplitude from the source
A'	attenuated amplitude after wave propagated through medium
a	internal radius of capillary
b	external radius of capillary
B	constant associated with classical absorption
C	constant associated with excess absorption of analyte
C'	constant associated with excess absorption of buffer
CE	capillary electrophoresis

CGE	capillary gel electrophoresis
CMC	critical micelle concentration
CZE	capillary zone electrophoresis
d	thickness of piezoelectric material in the transducer
dB	decibel
E	electric field strength
EOF	electro-osmotic flow
EP	electrophoresis
f	measuring frequency
f_r	resonance frequency of analyte
f_r'	resonance frequency of buffer
g	acceleration due to gravity
H	height that the sample is raised relative to outlet end of capillary
HEPES	4-(2-Hydroxyethyl)-1-piperazineethanesulfonic acid
HPLC	high-performance liquid chromatography
j	$\sqrt{-1}$
k	electromechanical coupling constant
k_f	forward reaction rate
k_b	backward reaction rate
L	total length of capillary
L_p	sample plug length
I	current
IL	insertion loss
M	adiabatic compressibility at infinite dilution
MS	mass spectrometry
N	coefficient associated with concentration
O	coefficient associated with concentration
P	pressure difference across capillary
PDMS	poly (dimethylsiloxane)
PZT	lead zirconium titanate
Q	volumetric flow rate (Poiseulle)
q	charge of the ionized solute
R	resistance
R1	reference port
r	radius of hydrated analyte ions
s	elastic compliance
S1	source port
S/N	signal-to-noise
SDS	sodium dodecyl sulfate
T	period of acoustic wave
T1	test port
t	time of sample introduction
$t_{propagation}$	wave propagation time
TAW	tube acoustic wave
TRAW	thin rod acoustic wave
U	thermodynamic energy
UV-Vis	ultraviolet visible
V	electric potential
V_i	input voltage signal
V_o	ouput voltage signal

v	volume
v_i	stoicheiometries of reactants and products
x	distance
Y	Young's modulus
Z	impedance

CHAPTER ONE:
INTRODUCTION

1.1 Capillary electrophoresis

Electrophoresis was developed by Tiselius as a method of protein separation in 1937[1]. This separation technique has been developed rapidly in the past two decades. The most significant of these advances allows electrophoretic separations to be performed inside a capillary tube, which gives rise to capillary electrophoresis (CE)[2,3]. By performing the separation in CE, only small amounts of analytes were needed. Furthermore, the high surface-to-volume ratio of capillaries allows for efficient dissipation of Joule heat which is generated from the electric current passing through the capillary. CE has become one of the most important techniques available for the analysis of chemical and biological samples. CE has been shown to be an effective tool for the separation of various analytes including metal ions, amino acids, proteins, nucleic acids and explosives[2,3]. Depending on the requirements of the analysis, CE can be coupled to different types of detection methods such as ultraviolet-visible (UV-Vis) absorbance, fluorescent spectroscopy, electrochemical measurement and mass spectroscopy (MS).

Fused silica capillaries employed in CE typically have internal diameters of 20 to 100 μm. Therefore, the amount of reagents and buffer solutions can be reduced by the small diameter of the capillary. A typical CE system is shown in Figure 1.1. It consists of a capillary tube with its two ends placed in two buffer reservoirs. A high voltage power supply is connected to the buffer reservoirs to create an electric potential difference (V) across the capillary, thus creating an electric field (E). E is given by equation (1),

$$E = \frac{V}{L} \tag{1}$$

where E is the magnitude of the electric field, V is the electric potential applied and L is the length of the capillary.

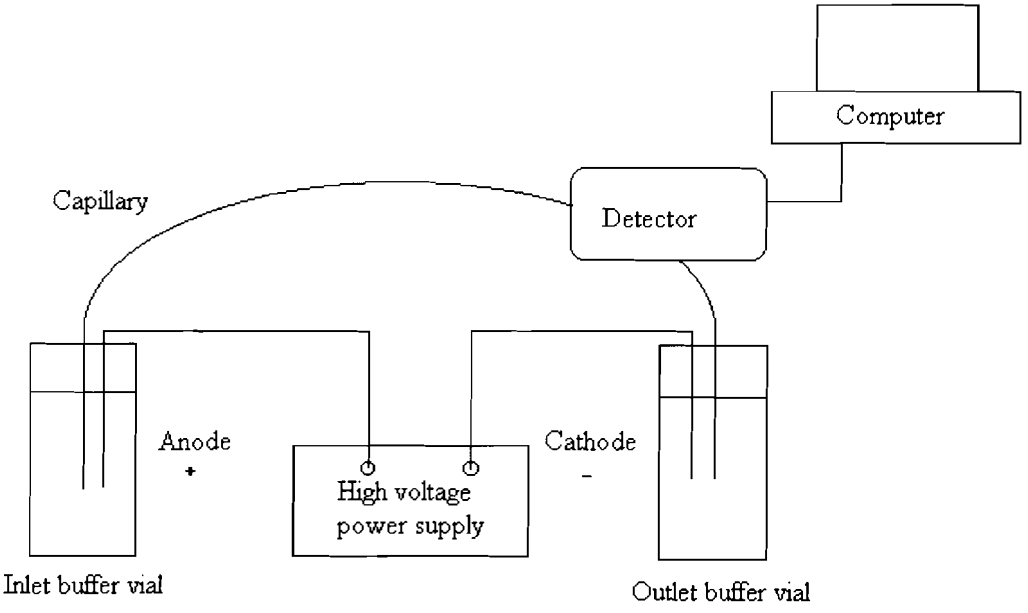

Figure 1.1. Schematic diagram of a CE system

Under the influence of this electric field, the electro-osmotic flow (EOF) occurs. The formation of EOF is due to the negatively charged surface on the inner wall of the fused silica capillary (see Figure 1.2). When the solution pH is above 3, ionization of the surface silanol group (SiOH) occurs. This makes the inner wall of the fused silica capillary negatively charged. This wall thus attracts cations in the buffer solution, creating an electrical double layer (see Figure 1.2). This double layer is considered as a static layer, whereas the cations further away from the capillary wall form a diffuse layer. When an electric potential is applied, the hydrated cations in the diffuse layer migrate to the cathode and carry solvent molecules in the same direction. A driving force is thus generated inside the capillary to pull the bulk solution towards the cathode. This

flow of solution, generated inside the capillary when an electric field is applied, is called EOF. EOF drives all ions, analytes and buffer towards the cathode, with an electro-osmotic velocity (v_{EOF}) inside the capillary given as follows[2]:

$$v_{EOF} = \frac{\psi \zeta E}{4\pi\eta} \qquad (2)$$

where ψ is the dielectric constant of the buffer, ξ is the zeta potential of the electrical double layer, E is the electric field and η is the viscosity of the buffer.

According to equation (2), v_{EOF} is related to the dielectric constant and viscosity of the buffer, zeta potential of the electrical double layer and the electric field applied to the system. The zeta potential of the electrical double layer is created by an electrical imbalance between the two layers which have a potential difference across the layers[2].

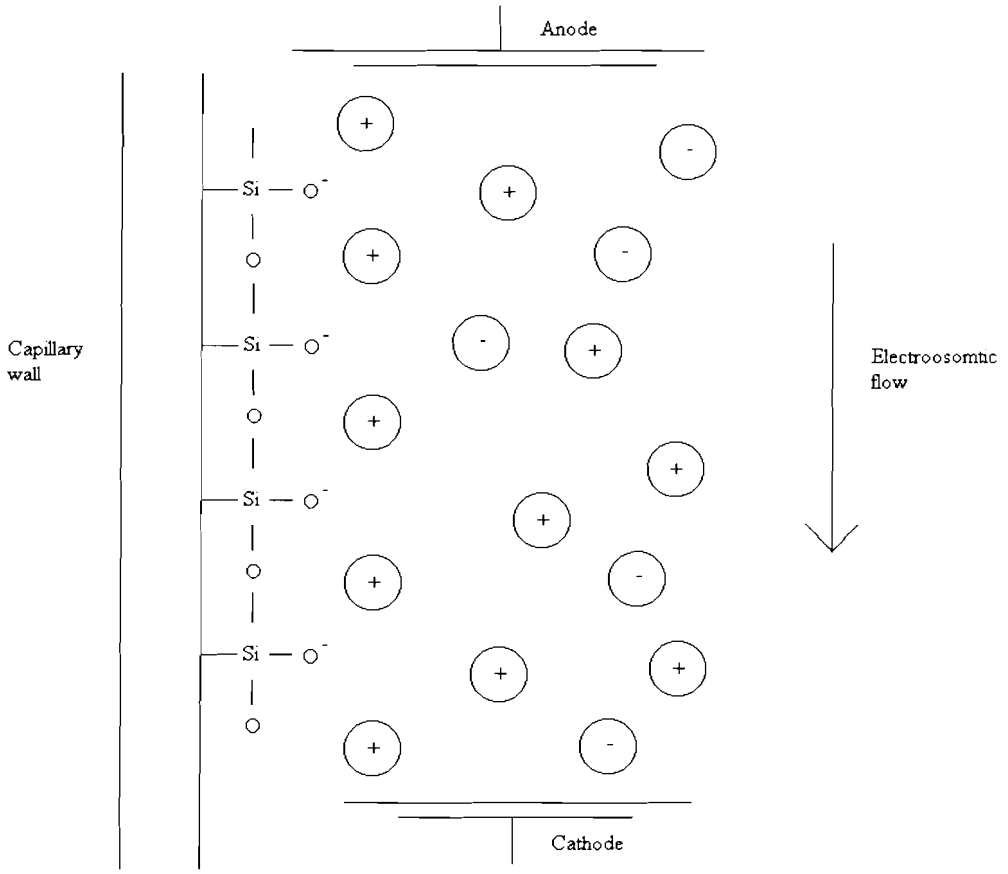

Figure 1.2. Electrical double layer at the fused silica/solution interface and the electro-osmotic flow

Besides EOF, charged chemical species move under the influence of an electric field thereby generating electrophoretic flow (EPF), v_{EPF}. The electrophoretic flow velocity depends on the charge-to-size ratio of different chemical species; therefore, different chemical species have different electrophoretic velocities and thus can be separated from each other. The magnitude of v_{EPF} is shown as follows:

$$v_{EPF} = \frac{qE}{6\pi\eta r} \tag{3}$$

where q is the charge of the ionized solute, E is the applied electric field, η is the viscosity of the buffer and r is the solute hydrated radius.

Accordingly, cations with the greatest charge-to-size ratio migrate towards the cathode with the greatest electrophoretic velocity, followed by cations with a smaller ratio (see Figure 1.3). In other words, cations are separated by differences in their electrophoretic velocities. Neutral molecules do not have a charge, so they are not separated. Similarly, anions with different charge-to-size ratios are separated.

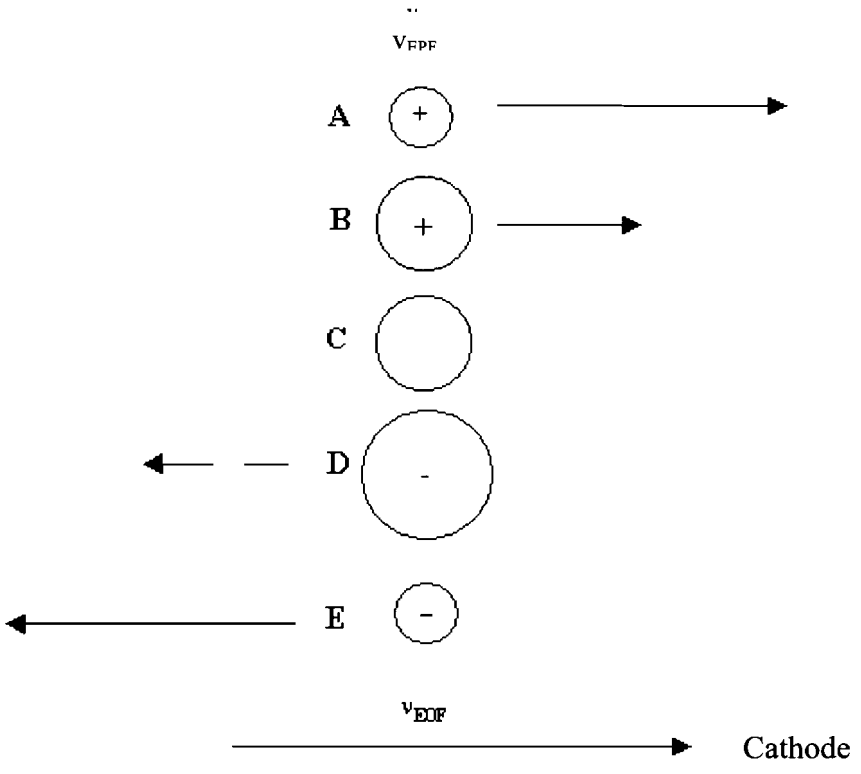

Figure 1.3. Ion migration during electrophoresis (where cathode is to the right, the arrows represent the sign and magnitude of the analytes according to their different EPF)

The net migration velocity of the analyte (v_{total}) is the vector sum of the EOF and EPF (see Equation (4)), which allows the migration order of the ions to be predicted. In the majority of CE separations, the magnitude of EOF is greater than that of EPF. So, the ions will move towards cathode according to the charge-to-size ratio. Figure 1.4a shows the migration order of ions in a CE system. The cation with the largest charge migrates the fastest, followed by cations with smaller charges. All neutral charged species migrate at the same speed after all cations.

Although anions tend to migrate towards the anode with EPF, the magnitude of EOF is greater than that of EPF; therefore, anions still migrate towards cathode with slower migration velocities. Anions with a smaller charge migrate faster towards the cathode with respect to anions with a larger charge. Hence, separation of various species can be achieved as shown in Figure 1.4b.

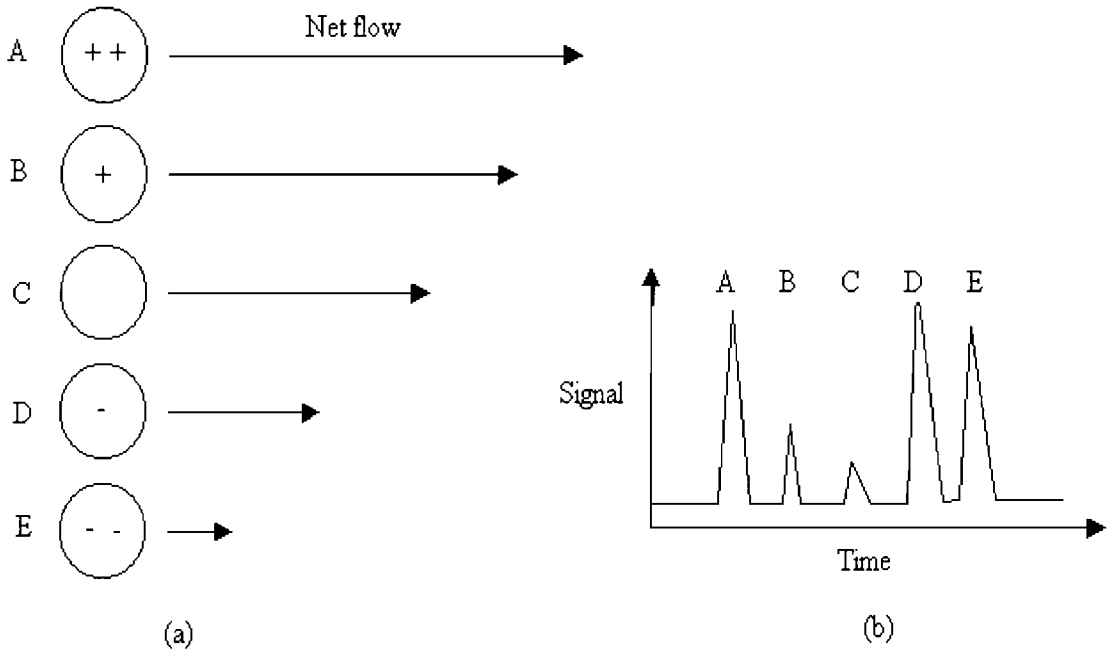

Figure 1.4. a) Migrations of ions due to the sum of EOF and EPF, b) Theoretical electropherogram showing the elution order (the cathode is to the right)

$$v_{total} = v_{EOF} + v_{EPF} \qquad (4)$$

The modes of CE separation include capillary zone electrophoresis (CZE), micellar electrokinetic capillary chromatography (MECC), and capillary gel electrophoresis (CGE). These modes are selected for different chemical and biological separations.

The particular mode for separating neutral compounds or compounds with similar charge-to-size ratio is MECC, which was developed by Terabe *et al* [4] and refined by Cohen *et al.*[5]. MECC is

widely used in the separation of neutral analytes, such as, noble metal ions[6] and drugs.[7,8] The basic principle of MECC is based on the use of surfactant-formed micelles to alter the mobility of the analytes inside the capillary. This method extends the enormous separation power of CE to the separation of neutral analytes.

The surfactant is an amphiphilic molecule, which consists of a polar or ionic head group and a hydrophobic tail. Above the critical micelle concentration (CMC), surfactants begin to form aggregates, called micelles. At room temperature, the CMC for the anionic surfactant sodium dodecyl sulfate (SDS) is about 8 mM[9]. The chemical and micellar structures of SDS are shown in figure 1.5.

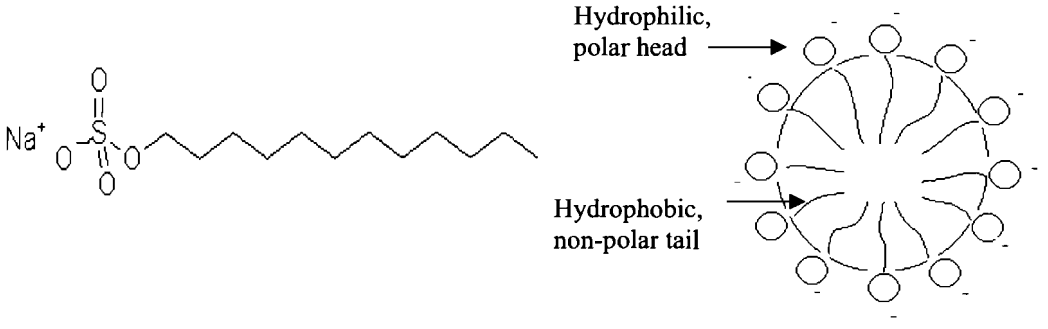

Figure 1.5. Chemical (left) and micelle (right) structures of SDS

Brij 35 and Triton X-100 are other types of surfactants (see Figures 1.6 and 1.7). Both of these are non-ionic surfactants with CMC of 0.07mM and 1.09mM, as stated in reference 9 and 10, respectively. The micellar structures of Brij 35 and Triton X-100 are quite different from that of SDS because they possess hydrophilic and hydrophobic faces as opposed to polar head groups and nonpolar tails in SDS.

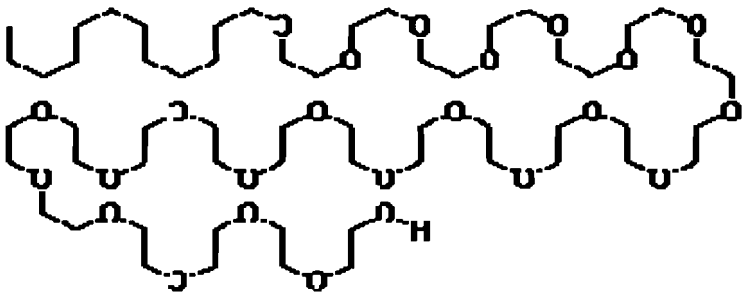

Figure 1.6. Chemical structure of Brij 35

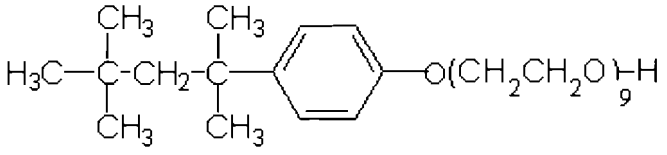

Figure 1.7. Chemical structure of Triton X-100

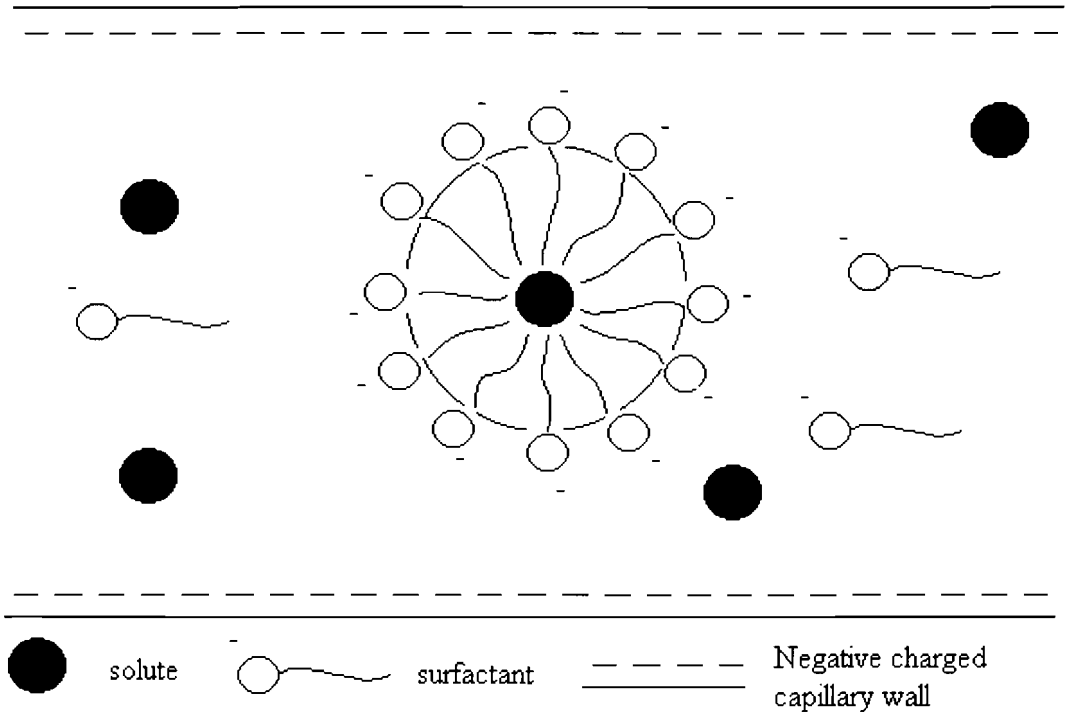

Figure 1.8. Schematic diagram of the principle of MECC separation

When a surfactant, such as SDS, is employed in the CE buffer system, some neutral analytes are incorporated into the micelle structure and migrate at the same velocity as the micelle, while other neutral analytes that remain free from the micelle migrate at the electro-osmotic velocity (see Figure 1.8). Under the influence of an electric field, the negatively charged micelles should move towards the positive electrode. However, with the larger magnitude of EOF, micelles end up migrating towards the negative electrode, but with a slower velocity. The difference in velocities of micelle-incorporated neutral analytes and free neutral analytes may allow for the separation of different neutral analytes. Highly polar neutral solutes, such as water and ethanol that do not interact with the micelles are often used as an EOF marker to indicate the EOF velocity.

The selection of surfactants is important in the CE separation because the surfactant molecules, if charged, will lead to an increase in the capillary current. SDS, which is an ionic surfactant, indeed causes an additional current when a high voltage is applied for CE separation. Unlike SDS, Brij 35 and Triton X-100 are non-ionic surfactants. The non-ionic property of the surfactant does not result in an excess current. However, the solutes in neutral non-ionic surfactant migrate in a similar manner as the free neutral solutes, resulting in no inherent separation enhancement.

1.2 Detection of unlabelled chemical species

Different methods of detection have been developed to detect various chemical species having different physiochemical properties[11]. The modes of detection are classified into electrical and spectroscopic. Electrical modes include conductivity and amperometric detection. Spectroscopic modes include ultraviolet-visible (UV-Vis) absorbance, fluorescence detection and mass spectrometry (MS). These well-established methods of detection are currently used in commercial instruments.

The use of these detection modes requires that the analytes must be either UV absorbing, fluorescent, or electroactive. Those analytes which do not have these physical properties are not detectable. Therefore, a method for detecting unlabelled species is needed. For instance, refractive index measurement is used to detect unlabelled sucrose[12,13] and alkaline earth ions[14]. Most of the amino acids are non-UV absorbing but having ultrasonic absorption properties. There are some reports that focus on the detection of underivatized amino acids using mass spectrometry[15, 16, 17]. Indirect detection methods, such as, chemiluminescence[18] and fluorescence[19] have also been reported. The detection limits were about 450 nM, 10 μM, and 32.9 μM for mass spectrometry[15], chemiluminescence[18] and fluorescence[19], respectively. Other than these methods, there is always great interest to detect analytes without using derivatization which would alter their structures and properties. Therefore, we explore a label-free method based on the ultrasonic acoustic wave absorption for the detection of underivatized amino acids.

1.3. Acoustic wave sensor

Acoustic wave sensors have been developed over the last few decades for measuring change of mass or density on a surface. Piezoelectric materials such as crystalline quartz and lead-zirconate-titanate (PZT) are commonly used in conventional acoustic wave devices. The pattern of the acoustic wave generated is governed by the pattern of the electrode deposited on the piezoelectric material with different crystalline orientations.

Thin rod acoustic wave (TRAW) and tube acoustic wave (TAW) devices are recently developed acoustic wave sensors[20]. The idea is to use external piezoelectric transducers to generate and receive the waves within the rod or tube structure. As opposed to conventional acoustic wave sensors, the rod or tube does not have to be fabricated from piezoelectric materials. The orientation of the transducers and the surface of the rod or tube govern the mode of the waves generated.

Our detector is constructed by coupling two piezoelectric transducers opposite to each other to obtain the ultrasonic acoustic wave signals. A small section of capillary, referred to as the detection zone, is sandwiched between the generating and receiving transducers (see Figure 1.9). Any mass or density change in the detection zone will perturb the acoustic wave propagation.

In addition to the mass and density changes, there is also ultrasonic absorption which depends on the analyte property such as the relaxation frequency which falls into the range of ultrasonic detection. These changes will be employed for the development of a label-free detector. The detection principle will be further described in Chapter two.

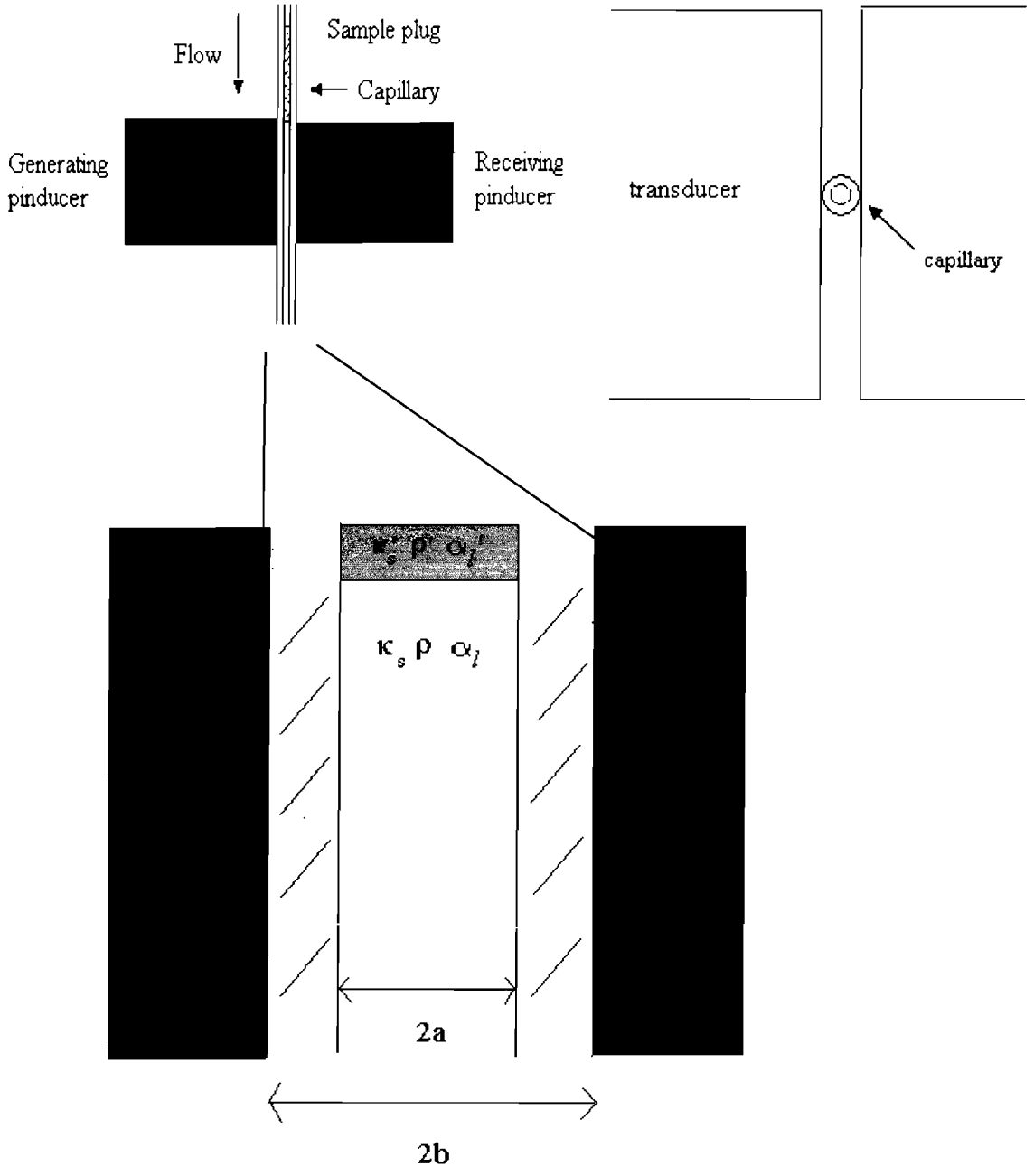

Figure 1.1. Schematic diagram of the acoustic wave detector in which the generating and receiving transducers are directly opposite each other. (Top left) side-view diagram (top right) cross-section diagram. (Bottom) The close-up diagram of the detection zone. κ_s, κ_s' are the isoentropic bulk moduli of buffer and sample, respectively. ρ and ρ' are the densities of buffer and sample, respectively. α_l and α_l' are the ultrasonic absorption coefficients of buffer and sample, respectively. a and b are the internal and external radius of the capillary, respectively.

1.4 Research Objectives

The author tried to develop an ultrasonic acoustic wave detector for CE separations. A small section of capillary, referred to as the detection zone, is sandwiched between the generating and receiving transducers. An acoustic wave is generated and transmitted through the capillary wall to the solution in the capillary. When the samples migrate through the capillary to the detection zone, they induce changes in the acoustic signals between the transducers coupled to the capillary. The difference between the sample and the run buffer perturbs acoustic wave propagation, which leads to a phase change or insertion loss change of acoustic wave transmission. This acoustic wave detection could be related to the change of material properties of the samples introduced into the capillary.

Temperature and current measurements are also used for the detection of analytes. The arrival of the sample at the detection zone will be indicated in these measurements. By combining the acoustic, thermal and current measurements, the acoustic detector can be validated.

The goals of this project:

- To construct an in-house CE instrument coupled with acoustic wave detector
- To use the acoustic wave method to detect various amino acids hydrodynamically introduced into the capillary
- To optimize the signal obtained in the acoustic detector in terms of the transducer type, acoustic frequency, capillary internal dimension, and capillary geometry
- To optimize the CE separation of amino acids in terms of buffer composition and electric voltage.

In this project, an in-house CE system with acoustic wave detector was constructed. The system was optimized in terms of transducer type, acoustic wave frequency, capillary internal dimension and capillary geometry. Single or capillary electrophoretically resolved amino acids had been detected by the acoustic wave detection system. Basic principles of acoustic wave propagation, wave transmission and reflection, and ultrasonic absorption of amino acids will be discussed in detail in chapter two. Experimental procedures and setup will be described in chapters three and four. Experimental results and discussion will be explained in detail in chapter five. In addition, conclusion and future work will be stated in chapter six.

CHAPTER TWO:
BASIC PRINCIPLE AND THEORY

2.1 Acoustic wave propagation

An acoustic wave, which is different from an electromagnetic wave, cannot travel through vacuum, but can travel in a medium. As the wave propagates in the medium, there are periodic disturbances or oscillation of the particles in the medium[21]. These waves can be classified into two types: longitudinal and transverse. In a longitudinal wave, the oscillations of the particles inside the medium are in the same direction as the direction that the wave propagates (see Figure 2.1).

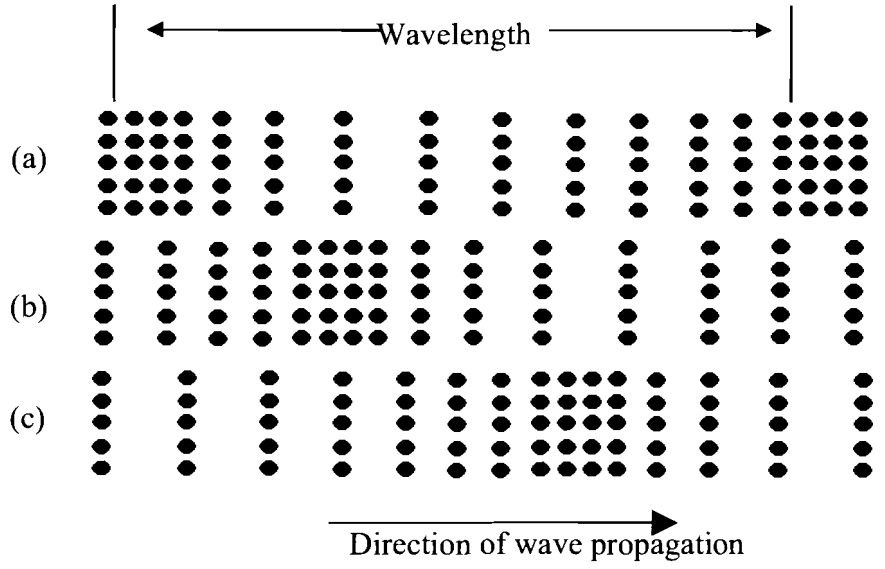

Figure 2.1. Schematic diagram of longitudinal wave propagation. The distance between two compression zones (i.e. where particles are close to each other) is defined as one wavelength. (a) to (c) illustrates the particle displacements at three different time points, showing the particle oscillations are in the same direction as the wave propagation.

As the longitudinal acoustic wave travels through different media (e.g. solids and fluids), individual particles in the medium vibrate back and forth in the direction that the wave travels, forming regions of compression and rarefaction. The distance between two consecutive compressions (or rarefactions) is defined as the acoustic wavelength (λ). The multiplication product of λ with the acoustic frequency (f) gives the acoustic wave velocity (v).

If f is in the audible range (200 - 20,000 Hz), the acoustic wave is called a sound wave. Besides longitudinal wave, the transverse wave is another wave type in which the particles oscillate perpendicularly to the direction the wave advances. Although longitudinal wave can propagate in both solids and liquids, only solids can support shear waves, a type of transverse wave, while fluids cannot. In fluids (i.e. liquid and gas), the particle disturbances cause a local pressure change, therefore the acoustic wave is also called the pressure wave.

The acoustic wave velocity depends on the physical properties (e.g. density) of the propagation medium. In a solid medium, the solid-state acoustic wave velocity (v_S) is given by:

$$v_s = \sqrt{\frac{Y}{\rho_s}} \tag{5}$$

where Y is the Young's modulus of the solid and ρ_s is the density of the solid.

In a liquid medium, the liquid-state acoustic wave velocity (v_L) is given by:

$$v_L = \sqrt{\frac{\kappa_s}{\rho}} \tag{6}$$

where ρ is the density of liquid inside the capillary and κ_s is the isoentropic bulk modulus of liquid.

The acoustic velocities in various media (in the audible frequencies) are summarized in table 1.

Table 1. The speed of sound in various media at 25°C [22,23,24]

Medium	Speed (m/sec)
Air	343
Glass	5640
Water, distilled	1498
Water, sea	1531

When the acoustic or pressure wave propagates at high frequency in a liquid medium, the particles oscillate so fast that the condition is considered to be adiabatic. Under this circumstance, there is no heat gain or loss in the system, and the isoentropic bulk modulus, κ_s, is defined as follows,[22]

$$\kappa_s = -\mathrm{v}\left(\frac{\partial p}{\partial \mathrm{v}}\right)_s \tag{7}$$

where v is the volume of the medium and p is pressure.

In the literature, the adiabatic compressibility (b_s) which is the reciprocal of κ_s, is usually given. This parameter can be related to the molecular concentration of the analyte (c_m) which is expressed in moles per unit volume.[25]

$$b_s = -\frac{1}{\mathrm{v}}\left(\frac{\partial \mathrm{v}}{\partial p}\right)_s = M + Nc_m + Oc_m^{3/2} \tag{8}$$

where M is the adiabatic compressibility at infinite dilution and N and O are coefficients associated with concentration. As an example of how the solution concentration, c_m affects b_s, for 0.1 mol/m^3 sodium chloride solution, the relative change of compressibility, $\Delta b_s/b_s$, is about 1%.[25]

These parameters of κ_s and b_s are in addition to the change in density that affects the phase change, as discussed later in section 2.6.

During particle oscillation as depicted in Figure 2.1, the time-dependent displacement (A) is given as follows[22],

$$RE(A) = A_{\circ} \exp(j\omega t) \tag{9}$$

where A_o is the maximum displacement of the particle; $j = \sqrt{-1}$; $\omega = 2\pi f$ is the angular frequency; t represents time.

In the ideal case, in which there is no energy loss in wave propagation, there is interchange between the kinetic and potential energies of the oscillating particles. At the particle displacement maximum A_o, the potential energy is maximized and the kinetic energy is zero. Therefore, the total energy density (total energy per unit volume) (e), can be given by the potential energy density at maximum displacement, which is defined as follows,[22]

$$e = \frac{1}{2}\rho A_{\circ}^{2} \ . \tag{10}$$

The power intensity density (total rate of energy transport per unit volume) (I), is defined as:

$$I = ev = \frac{1}{2}\rho v A_{\circ}^{2} \tag{11}$$

where v is the acoustic wave velocity.

Equation (11) will be used in section 2.4 that describes the transmission and reflection of acoustic waves at interfaces.

2.2 Amino acids

Amino acids belong to the class of organic compounds that are given by the general formula: $NH_2CHRCOOH$. Amino acids can be linked together by peptide bonds and act as the basic building blocks of peptides, and proteins. There are 20 amino acids commonly found in animals (listed in Figure 2.2). Their physical properties are listed in Table 2. Every amino acid, except glycine, has two optically active stereoisomers, D and L, in which the L-form is naturally occurring. The main reason for choosing amino acids as the analyte in the development of the acoustic wave detector is the existence of the proton-transfer reaction of amino acids in aqueous solution. This proton-transfer reaction results in a molar volume change, which gives the ultrasonic absorption property of amino acid in aqueous solutions.

Table 2. Physical properties of amino acids

Name	Symbol	Mol. Formula	Molar Weight	pK_a	pK_b	pI
Alanine	Ala	$C_3H_7NO_2$	89.09	2.34	9.69	6
Arginine	Arg	$C_6H_{14}N_4O_2$	174.2	2.17	9.04	10.76
Asparagine	Asn	$C_4H_8N_2O_3$	132.12	2.02	8.8	5.41
Aspartic acid	Asp	$C_4H_7NO_4$	133.1	1.88	9.6	2.77
Cysteine	Cys	$C_3H_7NO_2S$	121.16	1.96	10.28	5.07
Glutamine	Gln	$C_5H_{10}N_2O_3$	146.15	2.17	9.13	5.65
Glutamic acid	Glu	$C_5H_9NO_4$	147.13	2.19	9.67	3.22
Glycine	Gly	$C_2H_5NO_2$	75.07	2.34	9.6	5.97
Histidine	His	$C_6H_9N_3O_2$	155.16	1.82	9.17	7.59
Isoleucine	Ile	$C_6H_{13}NO_2$	131.17	2.36	9.6	6.02
Leucine	Leu	$C_6H_{13}NO_2$	131.17	2.36	9.6	5.98
Lysine	Lys	$C_6H_{14}N_2O_2$	146.19	2.18	8.95	9.74
Methionine	Met	$C_5H_{11}NO_2S$	149.21	2.28	9.21	5.74
Phenylalanine	Phe	$C_9H_{11}NO_2$	165.19	1.83	9.13	5.48
Proline	Pro	$C_5H_9NO_2$	115.13	1.99	10.6	6.3
Serine	Ser	$C_3H_7NO_3$	105.09	2.21	9.15	5.68
Threonine	Thr	$C_4H_9NO_3$	119.12	2.09	9.1	5.6
Tryptophan	Try	$C_{11}H_{12}N_2O_2$	204.23	2.83	9.39	5.89
Tyrosine	Tyr	$C_9H_{11}NO_3$	181.19	2.2	9.11	5.66
Valine	Val	$C_5H_{11}NO_2$	117.15	2.32	9.62	5.96

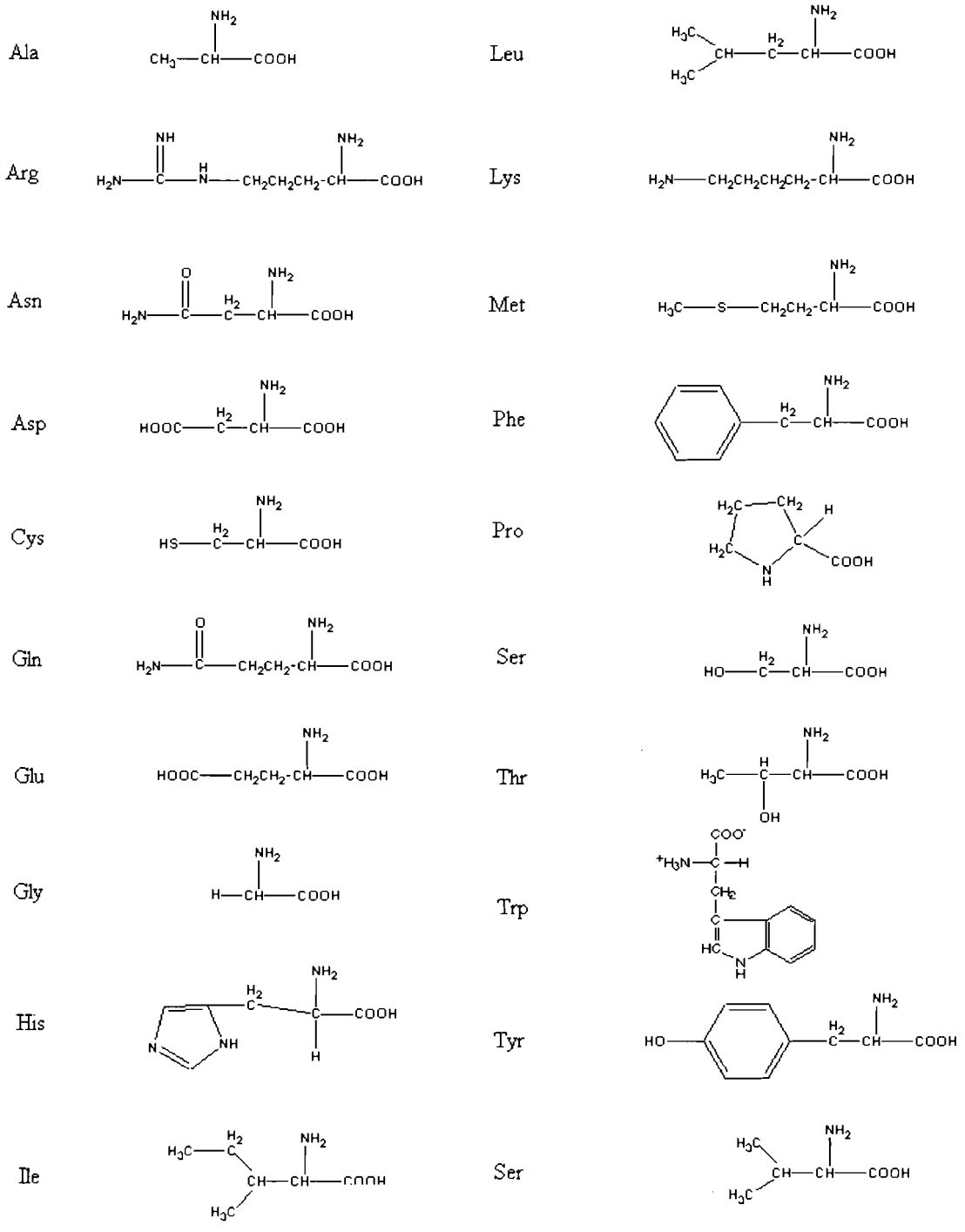

Figure 2.2. Structures of twenty naturally occurring amino acids

2.3 Ultrasonic Absorption

When acoustic waves propagate through any medium, the energy is absorbed and converted into heat. Such absorption will continuously attenuate the amplitude of the acoustic wave as it propagates through the medium. Therefore, the amplitude of the wave can be related to the ultrasonic absorption coefficient (α) and the propagation path (x) as follows:

$$\text{Differential form: } \frac{dA'}{A'} = -\alpha dx \tag{12}$$

$$\text{Integrated form: } A' = A\exp(-\alpha x) \tag{13}$$

where A' is the amplitude of acoustic wave after attenuation and A is the unattenuated amplitude from the source.

There are two major mechanisms of ultrasonic absorption, and they are termed as classical and excess ultrasonic absorption. The classical absorption is related to the physical processes (e.g. internal viscous friction and finite thermal conductivity) of the liquid solvent as described in section 2.3.1; whereas the excess absorption is related to the chemical processes (e.g. chemical relaxation) of the solutes as described in section 2.3.2.

2.3.1 Classical Ultrasonic Absorption

The classical absorption of acoustic energy is caused by internal viscous friction and the finite thermal conductivity of the solvent molecules. In the latter case, under the influence of the ultrasonic wave, the heat transfer, which is not infinitely fast or does not have an infinite thermal conductivity, is considered to occur under adiabatic conditions. For comparison, thermal conduction in aqueous solution without the influence of acoustic waves usually occurs under the constant temperature or isothermal conditions.

During adiabatic compression of a unit volume of the system by the ultrasonic wave, the average translational energy of the molecules in this volume increases.[22] This energy is coupled through and distributed between other molecular energy components, such as vibrational energy, conformational energy, and structural energy. At low frequency, since the energy interchange can keep up with the pressure change, all the energy gained by the molecules in compression is returned back to the acoustic wave during rarefaction. However, if the compression occurs faster than the rate of energy exchange, the energy will be returned out-of-phase, and therefore, an energy loss occurs during each compression/rarefaction cycle. Such a process results in ultrasonic absorption because the induced density changes do not occur in phase with the pressure changes caused by the ultrasonic wave propagation.[26]

The classical ultrasonic absorption due to the above change can be described by an ultrasonic absorption coefficient (α_{cl}), as given by[26]

$$\alpha_{cl} = Bf^2 \tag{14}$$

where B is a constant of the classical absorption and f is the acoustic frequency. It is clear that the value of α_{cl} increases as the frequency increases.

For instance, the classical absorption coefficient of water at 25 °C, is given by B = 21.2 x 10^{-15} s^2 m^{-1}.[27, 28] At high frequency, the classical absorption is usually the dominant process of ultrasonic absorption.

2.3.2 Excess Ultrasonic Absorption

There are excess energy losses in each compression/rarefaction cycle when there are solutes (e.g. amino acids) that undergo chemical change with a concomitant volume change. In chemical reactions, the molecules (reactants and products) are displaced from their equilibrium

concentrations in response to perturbations, such as the changes of pressure and temperature. When the perturbation is removed, the molecular concentrations relax back to their equilibrium values. As an analogy, the relaxation of electrons in molecules from the excited state to the ground state occurs, as studied in molecular spectroscopy. Such additional energy loss during each compression/rarefaction cycle causes excess ultrasonic absorption which also depends on how fast the relaxation processes occur.

One example of the chemical change is the proton-transfer reaction of an amino acid, as shown in Figure 2.3 and given by the following:[29]

$$ZH + OH^- \underset{k_b}{\overset{k_f}{\leftrightarrow}} Z^- + H_2O \qquad (15)$$

where ZH is $^-OOC\text{-}R\text{-}NH_3^+$ and k_f and k_b are the forward and backward reaction rate constants, respectively.

According to Le Chatelier's principle, any process involving a change of molar enthalpy (ΔH) will respond to the perturbation of local temperature. Similarly, any process involving a change in molar volume (Δv) will respond to the perturbation of local pressure. As an example, for glutamic acid, there is a decrease in molar volume of 20-30 mL per mole of the dissociation equilibrium of the amino hydrogen of amino acid[26]. The changes in molar volume can be caused by the changes in the compositions, and the fact that the ability of Z^- to attract water molecules is lower than that of Z and OH^-. Therefore, as the equilibrium system is undergoing a compression, the system tends to decrease the volume by shifting the equilibrium to the side with the smaller molar volume, i.e. the right hand side in equation (15).

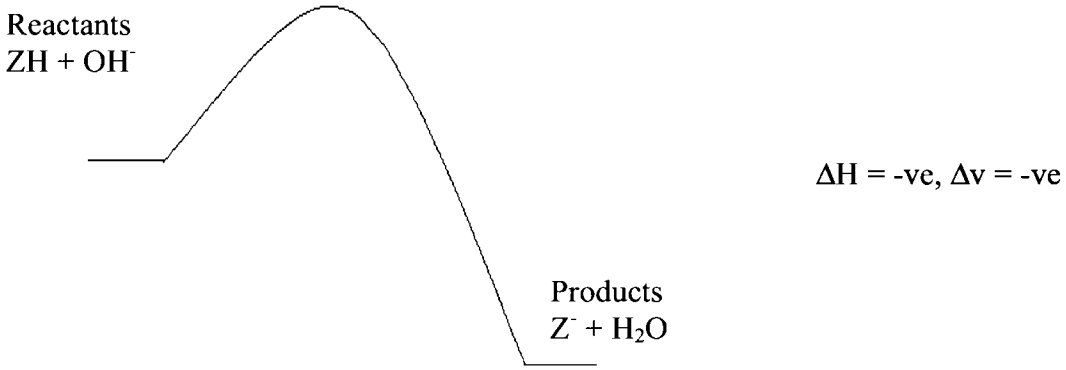

Figure 2.3. **Changes in enthalpy and volume in the proton-transfer equilibrium**

To mathematically describe the change in composition due to the pressure perturbation, we define the concentration displacement of [ZH] to be ξ. Upon a perturbation, the concentrations of the 3 chemical species become,[26]

$$[ZH] = [ZH]_0 - \xi \tag{16}$$

$$[Z^-] = [Z^-]_0 + \xi \tag{17}$$

$$[OH^-] = [OH^-]_0 - \xi \tag{18}$$

where $[ZH]_0$, [Z-] and $[OH^-]_0$ are the equilibrium concentrations of ZH, Z^- & OH^-, respectively.

Now, we have

$$\begin{aligned} \frac{d[Z^-]}{dt} &= \frac{d\xi}{dt} = k_f[ZH][OH^-] - k_b[Z^-] \\ &= k_f([ZH]_0 - \xi)([OH^-]_0 - \xi) - k_b([Z^-]_0 + \xi) \end{aligned} \tag{19}$$

Neglecting the ξ^2 term and noting that, at equilibrium,

$$k_f[ZH]_\circ[OH^-]_\circ - k_b[Z^-]_\circ = 0 \quad . \tag{20}$$

Equation 19 becomes

$$\frac{d\xi}{dt} = -\left\{k_f\left([ZH]_\circ + [OH^-]_\circ\right) + k_b\right\}\xi . \tag{21}$$

The solution to the above differential equation can be given by

$$\xi = \xi_\circ \exp\left(\frac{t}{\tau}\right) \tag{22}$$

where τ is the relaxation time given by,

$$\tau = \frac{1}{k_f\left([ZH]_\circ + [OH^-]_\circ\right) + k_b} \tag{23}$$

where k_f and k_b are the rate constants defined in equation (15). This relaxation time is related to the duration required for the relaxation or return of the product concentration to the equilibrium concentration. Such a chemical relaxation process, which is the cause of excess ultrasonic absorption, depends on the two rate constants as well as the initial amino acid concentration and the solution pH.

The excess ultrasonic absorption coefficient (α_{ex}) can be mathematically expressed as follows,[26]

$$\alpha_{ex} = \frac{C\tau \cdot f^2}{1+\left(\frac{f}{f_r}\right)^2} = \left(\frac{C\tau \cdot f^2}{1+\left(\frac{f}{\frac{1}{2\pi\tau}}\right)^2}\right) = \left(\frac{C\tau}{1+(2\pi f\tau)^2}\right) f^2 \tag{24}$$

where f is the ultrasonic wave frequency (Hz); C is a constant of excess absorption and τ is the relaxation time and f_r is the relaxation frequency expressed as [30]

$$f_r = \frac{1}{2\pi\tau} \tag{25}$$

where τ is the relaxation time associated with the perturbation of the acid-base equilibrium by the acoustic wave as given by equation (23).

For the usual chemical relaxation processes, the relaxation time constants range from

10^{-5} to 10^{-10} s (in reference 26), which translate to the relaxation frequencies ranging from 16 kHz to 1.6 GHz.

From equation (24), we notice that as the frequency increases from a low value, the excess absorption first starts to increase. When the frequency reaches the relaxation frequency, the amount of energy absorbed will be maximized. Any further increase in frequency will result in a decrease in ultrasonic absorption. By combining equations (14) and (24), the total ultrasonic absorption (α) is given as follows:

$$\alpha = \alpha_{ex} + \alpha_{cl} = \frac{C\tau \cdot f^2}{1 + \left(\frac{f}{f_r}\right)^2} + B \cdot f^2 . \qquad (26)$$

The study of the relaxation processes using ultrasonic wave detection is referred to as ultrasonic relaxation spectroscopy. It has been used to study various chemical processes such as protolysis, hydrolysis, conformation changes, dimerization, and complexation.[31] Usually, the longitudinal ultrasonic wave is used since it probes compression and rarefaction, and is more relevant in the studies of solutions.[32]

2.4 Reflection at interface

Now, we consider the ultrasonic wave propagation along an interface between two media in the acoustic detector. As previously shown in Figure 1.9, the wave passes through the capillary wall and solution. We note that the capillary is of a finite dimension in the cross-section direction, but the capillary is considered infinite along the axial direction. As a first step to study the complicated physics problem, we describe the wave propagation using a one-dimensional approximation. This is an over-simplified treatment for the actual 2-dimensional case of acoustic propagation in a cylindrical shell, as previously reported.[33,34]

As shown in Figure 2.3, wave reflection (to the left) occurs along with transmission (to the right). The incident acoustic amplitude is given by A_{1+}. The transmitted acoustic amplitude in medium 2 and the reflected amplitude in medium 1 are given by A_{2+} and A_{1-}, respectively. The relative extent of reflection and transmission are related to material properties, as given by a parameter known as the acoustic impedance.[26] The acoustic impedance (Z) is defined as ρv (where ρ is the density of the medium and v is the acoustic velocity) as follows:

$$Z_1 = \rho_1 v_1 \tag{27}$$

$$Z_2 = \rho_2 v_2 . \tag{28}$$

The amplitude-based reflection coefficient ($\Re_a$) is defined as the ratio of the reflected amplitude to the incident amplitude and is given as follows,[26]

$$\Re_a = \frac{A_{1-}}{A_{1+}} = \frac{Z_2 - Z_1}{Z_1 + Z_2} . \tag{29}$$

The transmission coefficient ($\Im_a$) is defined as the ratio of the transmitted amplitude to the incident amplitude, and is given by the following equation:

$$\Im_a = \frac{A_{2+}}{A_{1+}} = \frac{2Z_2}{Z_1 + Z_2}. \tag{30}$$

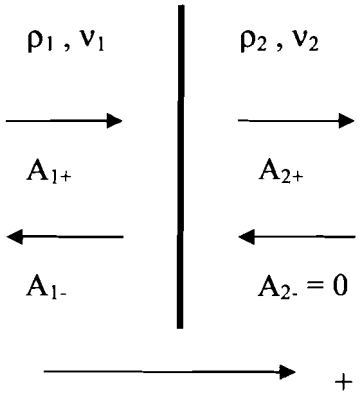

Figure 2.4. Pressure wave travelling across an interface between medium 1 and medium 2. The direction to the right is assigned as positive. The densities and velocities in the two media are given as ρ_1, v_1, and ρ_2, v_2, respectively. The incident acoustic amplitude is A_{1+}. The transmitted amplitude in medium 2, and the reflected amplitude in medium 1 are given by A_{2+} and A_1, respectively. Since there is no reflected amplitude in medium 2, A_{2-} is zero.

The acoustic energy is conserved at the interface, and the intensity function as defined in equation (11) will be invoked. Accordingly, the intensity-based reflection coefficient ($\Re_I$) and transmission coefficients ($\Im_I$) are defined as follows,[26]

$$\Re_I = \frac{I_{1-}}{I_{1+}} = \left(\frac{A_{1-}}{A_{1+}}\right)^2 = \Re_a^2 \tag{31}$$

$$\Im_I = \frac{I_{2+}}{I_{1+}} = \left(\frac{Z_1}{Z_2}\right)\left(\frac{A_{2+}}{A_{1+}}\right)^2 = \frac{\rho_1 v_1}{\rho_2 v_2}\Im_a^2. \tag{32}$$

The conservation of energy requires that

$$\Re_I + \Im_I = 1. \tag{33}$$

2.5 Transmission and attenuation of acoustic waves

For acoustic propagation in solids, scattering from grain boundaries also occurs. The scattering effect adds onto the ultrasonic absorption. Both scattering and ultrasonic absorption depend on the distance of the wave propagates through the solid medium. In order to combine the scattering and ultrasonic absorption, ultrasonic attenuation is used and is expressed as follows:

$$A' = A\exp(-\alpha_s x) \tag{34}$$

where A' is the attenuated amplitude after the wave has propagated through the solid medium over a distance x, A is the unattenuated amplitude from the source and α_s is the attenuation coefficient in the solid medium.

For acoustic propagation in solutions, there is no scattering unless there are particles suspended in the solutions. Ultrasonic attenuation is then caused only by ultrasonic absorption.

In our case of ultrasonic propagation across a capillary tube in which a liquid is passed, there are five media, as shown in Figure 2.5. This 5-media consideration is one-dimensional along the capillary axis for simplicity, without considering the finite size of the capillary (see Figure 1.9). As already stated in section 2.4, this is an over-simplified treatment for the actual 2-dimensional case. The five consecutive media which the plane wave propagates from left to right is numbered as 5,4,3,2 and 1. The wave propagates from left to right; the initial amplitude of the generating transducer is A_5. After wave absorptions within various media and reflections at various boundaries, the wave amplitude is reduced to A_{5a} at the receiving transducer. For instance, at the boundary between media 5 and 4, i.e. 5-4, reflection occurs, and the transmission component is notated as A_4 and the reflection component as B_5. Similarly, at the boundary 4-3, the

transmission component is named as A_3 and the reflection component as B_4. Finally, the wave amplitude obtained at the receiving transducer is A_{1a}.

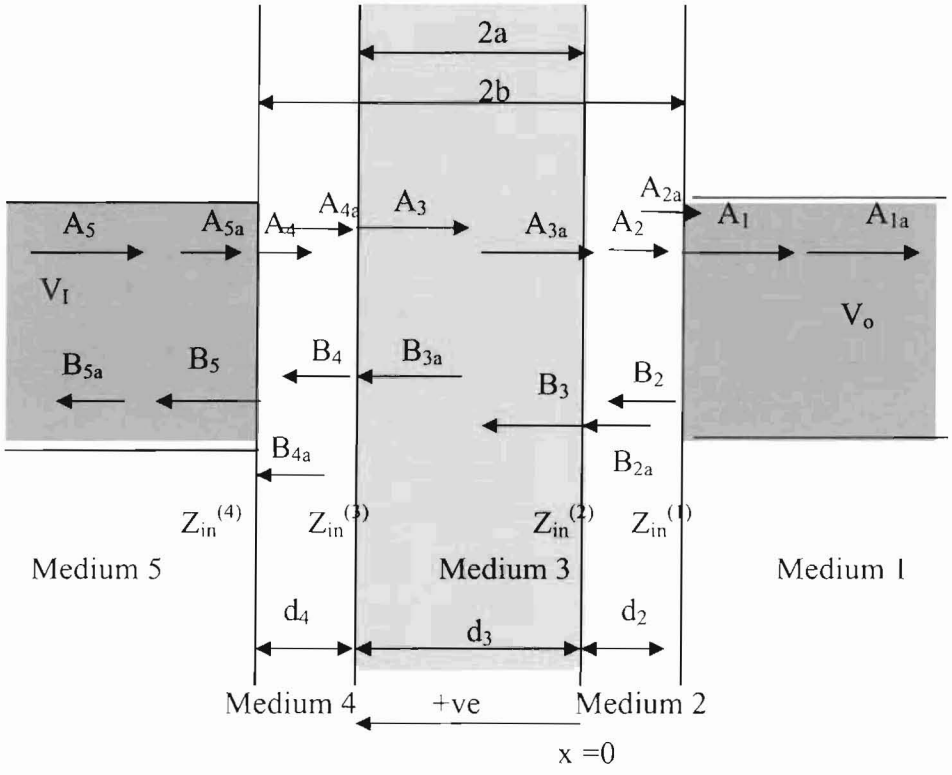

Figure 2.5. The close-up diagram of the detection zone. V_I is the source voltage supplied to the generating transducer and V_o is the signal voltage obtained at the receiving transducer; a and b are the internal and external radius of the capillary, respectively; d is the thickness of the piezoelectric material in the pinducers; α_s and α_l are the solid ultrasonic attenuation coefficient and liquid ultrasonic absorption coefficient, respectively; A_5 is the incident acoustic amplitude; A_x and B_x are the transmitted amplitude in medium x and the reflected amplitude in medium x, respectively, where x = 1-5; A_{1a} is the acoustic amplitude received from the receiving pinducer.

The distance of the wave traveled is denoted as x, and the x-coordinate runs from right to the left. At the boundary between media 2 and 1, x is set to be zero. The thickness of each layer is defined, i.e. d_2, and d_4 are the thickness of the capillary wall, and d_3 is the thickness of the capillary. As we mentioned previously, the wave amplitude reduces from the initial amplitude, A_5 to the final amplitude, A_{1a}. We denote this reduction by insertion loss (IL), which is defined as,

$$IL = 10\log_{10}\left(\frac{A_{1a}}{A_5}\right)^2, \tag{35}$$

In order to get $\frac{A_{1a}}{A_5}$, we use the equations of the wave transmission coefficients and absorption.

The local specific input impedance of the layers, i.e. the impedances of the boundaries (between layer n+1 and n) are named $Z_{in}^{(n)}$, n=1,2,3,4; and the intrinsic specific impedance for the plane wave in medium n are Z_n, n=1,2,3,4,5.

Z_n is defined as[35]:

$$Z_n = \frac{\rho_n v_n}{\cos\vartheta_n}, \tag{36}$$

where ρ is the density of the medium, θ is the angle of the incidence of the wave and c is the velocity of propagation of the wave.

In our experiments, we assume the wave is normal incidence, i.e. $\theta_n = 0^\circ$, and so

$$Z_n = \rho_n v_n \tag{36a}$$

Since there are multiple reflections from the boundaries of the layers, two resulting waves are found inside each layer, with opposite directions of propagation. Such wave propagation can be expressed by the acoustic pressure. For instance, the expression for the acoustic pressure in medium 2 can be written as[35]

$$p_2 = \left[Ae^{-ik_{2x}x} + Be^{ik_{2x}x}\right] \tag{37}$$

where $k_{2x} = \frac{\omega}{v_2}$, A and B are constants, ω is the wave frequency , and k is the propagation vector.

In the x direction, the x-component of the velocity υ_2 in medium 2, or υ_{2x} is given by[35]

$$v_{2x} = \left(\frac{1}{i\omega\rho_2}\right)\left(\frac{\partial p_2}{\partial x}\right) \tag{38}$$

Therefore, by differentiating equation 36, we have

$$v_{2x} = \frac{k_{2x}}{\omega\rho_2}\left[Be^{ik_{2,x}x} - Ae^{-ik_{2,x}x}\right] = \left(\frac{1}{Z_2}\right)\left[Be^{ik_{2,x}x} - Ae^{-ik_{2,x}x}\right] \text{where } Z_2 = \frac{\omega\rho_2}{k_{2x}} = \frac{\rho_2 v_2}{\cos\theta_2} \tag{38a}$$

Now, we assume medium 1 to be semi-infinite, and from the continuity of the impedance on the boundary between media 2 and 1, i.e. x=0, we have[35]

$$-\left(\frac{p_2}{v_{2,x}}\right)_{x=0} = Z_1 \tag{39}$$

where $Z_1 = \rho_1 c_1$.

Substituting the equation (37) and (38a) into (39) and rearrange, we have

$$\frac{B}{A} = \frac{(Z_1 - Z_2)}{(Z_1 + Z_2)}, \tag{40}$$

where $Z_2 = \dfrac{\rho_2 v_2}{\cos\theta_2}$

The local specific input impedance at the left boundary between media 3 and 2 is, by definition[35],

$$Z_{in}^{(2)} = -\left(\frac{p_2}{v_{2,x}}\right)_{x=d_2}. \tag{41}$$

Substituting equations (37), (38a) into (41). Then, take equation (40) into account, and use the relation, $e^{ikd} = \cos kd + i\sin kd$, we find[35]

$$Z_{in}^{(2)} = \left(\frac{Z_1 - iZ_2 \tan k_{2x} d_2}{Z_2 - iZ_1 \tan k_{2x} d_2} \right) Z_2 . \tag{41a}$$

This expression allows us to calculate the transmission coefficient at this boundary using equation 35.

In our five media and four boundaries system, we have four $Z_{in}^{(n)}$ values, which can be calculated by means of 3-fold application of equation (41a). For instance, by setting $Z_{in}^{(1)} = Z_1$, we obtain $Z_{in}^{(2)}$,

$$Z_{in}^{(2)} = \left(\frac{Z_{in}^{(1)} - iZ_2 \tan k_{2x} d_2}{Z_2 - iZ_{in}^{(1)} \tan k_{2x} d_2} \right) Z_2 . \tag{41b}$$

Similarly, we obtain

$$Z_{in}^{(n)} = \left(\frac{Z_{in}^{(n-1)} - iZ_n \tan k_{nx} d_n}{Z_n - iZ_{in}^{(n-1)} \tan k_{nx} d_n} \right) Z_n \tag{41c}$$

where n =3, 4, 5.

Without the consideration of acoustic absorption, the acoustic pressure in each medium is

$$p_1 = A_1 e^{ik_{1x}x}, \tag{42a}$$

$$p_2 = \left(A_2 e^{-ik_{2x}x} + B_2 e^{ik_{2x}x} \right), \tag{42b}$$

$$p_3 = \left(A_3 e^{-ik_{3x}(x-d_2)} + B_3 e^{ik_{3x}(x-d_2)} \right), \tag{42c}$$

$$p_4 = \left(A_4 e^{-ik_{4x}(x-d_2-d_3)} + B_4 e^{ik_{4x}(x-d_2-d_3)} \right), \tag{42d}$$

$$p_5 = \left(A_5 e^{-ik_{5x}(x-d_2-d_3-d_4)} + B_5 e^{ik_{5x}(x-d_2-d_3-d_4)} \right) \tag{42e}$$

Note that d_2=(b-a), d_3=2a, d_4=(b-a).

where p_1 and p_5 represent the acoustic pressures in the receiving and generating transducers; p2 and p4 represent those in the capillary wall, and p3 in the liquid medium inside the capillary.

In the presence of acoustic absorption, the acoustic pressures are augmented with an absorption factor, the acoustic pressures in the five media are therefore given by,

$$p_1 = A_1 e^{ik_{1x}x} e^{\alpha_{s1}x}, \tag{42f}$$

$$p_2 = A_2 e^{-ik_{2x}x} e^{\alpha_{s2}(x-d_2)} + B_2 e^{ik_{2x}x} e^{-\alpha_{s2}x}, \tag{42g}$$

$$p_3 = A_3 e^{-ik_{3x}(x-d_2)} e^{\alpha_l(x-d_2-d_3)} + B_3 e^{ik_{3x}(x-d_2)} e^{-\alpha_l(x-d_2)}, \tag{42h}$$

$$p_4 = A_4 e^{-ik_{4x}(x-d_2-d_3)} e^{\alpha_{s2}(x-d_2-d_3-d_4)} + B_4 e^{ik_{4x}(x-d_2-d_3)} e^{-\alpha_{s2}(x-d_2-d_3)}, \tag{42i}$$

$$p_5 = A_5 e^{-ik_{5x}(x-d_2-d_3-d4)} e^{\alpha_{s1}(x-d_2-d_3-d_4-d_5)} + B_5 e^{ik_{5x}(x-d_2-d_3-d4)} e^{-\alpha_{s1}(x-d_2-d_3-d_4)} \tag{42j}$$

where α_{s1} , α_{s2} and α_l are the ultrasonic absorption coefficients for transducer material, capillary wall and liquid, respectively.

The pressure should be continuous at the boundary[35], therefore,

$$A_j e^{-ik_j d_j} e^{-\alpha_j d_j} + B_j e^{ik_j d_j} e^{\alpha_j d_j} = A_{j+1} + B_{j+1}, \tag{43a}$$

$$Z_j \frac{\left(A_j e^{-ik_j d_j} + B_j e^{ik_j d_j}\right)}{\left(A_j e^{-ik_j d_j} - B_j e^{ik_j d_j}\right)} = Z_{in}^j, \tag{43b}$$

$$Z_{j+1} \frac{\left(A_{j+1} + B_{j+1}\right)}{\left(A_{j+1} - B_{j+1}\right)} = Z_{in}^j, \tag{43c}$$

where Z_j is given by the equation (37). From the last two equations we find

$$\left(\frac{B_j}{A_j}\right) e^{2ik_j d_j} = \frac{\left(Z_{in}^j - Z_j\right)}{\left(Z_{in}^j + Z_j\right)}, \tag{43d}$$

$$\left(\frac{B_{j+1}}{A_{j+1}}\right) = \frac{\left(Z_{in}^j - Z_{j+1}\right)}{\left(Z_{in}^j + Z_{j+1}\right)}. \tag{43e}$$

Therefore, equation (43a) can be written as

$$A_j e^{ik_j d_j} e^{\alpha_j d_j} \left[1 + \left(\frac{B_j}{A_j} \right) e^{2ik_j d_j} \right] = A_{j+1} \left(1 + \frac{B_{j+1}}{A_{j+1}} \right). \tag{44}$$

Substituting equations (43d) and (43e) therein,

$$\frac{A_j}{A_{j+1}} = \frac{\left(Z_{in}^j + Z_j \right)}{\left(Z_{in}^j + Z_{j+1} \right)} e^{ik_j d_j} e^{-\alpha_j d_j}. \tag{45}$$

We finally obtain the following equation,

$$\frac{A_1}{A_n} = \prod_{j=1}^{n} \frac{\left(Z_{in}^j + Z_j \right)}{\left(Z_{in}^j + Z_{j+1} \right)} e^{ik_j d_j} e^{-\alpha_j d_j}. \tag{46}$$

where n =1,2,3,4,5. d_1 *and* d_5 is the thickness of the piezoelectric material which equals to 4.6 mm, d_2 and d_4 are the thickness of the capillary which is 55 μm and d_3 is the internal diameter of the capillary which is 250 μm. α_j are the absorption coefficient for the piezoelectric material and the capillary wall which is around 2.3 m^{-1} [36]and α_3 is the absorption coefficient in which the liquid absorption is calculated by equation (26).

If there is no absorption considered in the system, we have

$$\frac{A_1}{A_n} = \prod_{j=1}^{n} \frac{\left(Z_{in}^j + Z_j \right)}{\left(Z_{in}^j + Z_{j+1} \right)} e^{ik_j d_j}, \tag{46a}$$

where all the absorption coefficients are equal to zero.

2.6 Phase and insertion loss

Both attenuation and reflection reduces the amplitude of the detected signal, leading to the change in energy loss. In addition, time delays or phase changes are encountered which is related to the wave velocity. In our study, the acoustic wave measurement is based on monitoring changes in two parameters. First, density changes lead to alterations in the acoustic wave velocity, which in turn cause a change in the propagation time across the capillary cross-section. This is ultimately detected as a change in the phase angle. Second, ultrasonic absorption results in a change in the acoustic wave amplitude, which can be characterized in terms of energy loss. In our experiment, we determine changes in acoustic phase angle and energy loss by measuring the changes in electrical phase change and insertion loss using a network analyzer. The following section illustrates how these two measured parameters are related to some physical constants of the system.

Phase ϕ is given as,

$$\phi = \tan^{-1}\left(\frac{\left(V_{90^\circ}\right)_o}{\left(V_{0^\circ}\right)_o}\right) - \tan^{-1}\left(\frac{\left(V_{90^\circ}\right)_i}{\left(V_{0^\circ}\right)_i}\right) \tag{47}$$

where V_{90}° and V_0° are the two orthogonal components of the voltage vector and the subscripts o and i represent the output and input, respectively.

The phase is related to the propagation time ($t_{propagation}$) for the acoustic path traveled by the wave from the generating transducer, through the capillary wall and the liquid, to the receiving transducer. The phase (ϕ) can also be given as,

$$\phi = \frac{2\pi \cdot t_{propagation}}{T} \tag{48}$$

T, which is the period of the acoustic wave, is given by

$$T = \frac{1}{f} \tag{49}$$

where f is the acoustic frequency.

The propagation time is the total time the wave propagated in the solid and liquid phases, therefore, $t_{propagation}$ can be written as,

$$t_{propagation} = \frac{2(b-a)}{v_s} + \frac{2a}{v_L} \tag{50}$$

where a and b are the internal and external radius of the capillary tube, respectively.

By substituting the wave velocity equations (5) and (6) into equation (50), we have

$$t_{propagation} = \frac{2(b-a)}{\sqrt{(Y/\rho_s)}} + \frac{2a}{\sqrt{\kappa_s/\rho}}. \tag{51}$$

Combining equations (48), (49) and (51), we have

$$\phi = 2\pi ft = 2\pi f\left[\frac{2(b-a)}{\sqrt{Y/\rho_s}} + \frac{2a}{\sqrt{\kappa_s/\rho}}\right]. \tag{52}$$

For a change in phase ($\Delta\phi$) caused by the replacement of solution 1 (buffer) by solution 2 (sample), the following equation is obtained:

$$\Delta\phi = 2\pi f\left(\frac{2a}{\sqrt{\kappa_s'/\rho'}} - \frac{2a}{\sqrt{\kappa_s/\rho}}\right) \tag{53}$$

where ρ and ρ' are the density of liquid 1 (buffer) and liquid 2 (sample) inside the capillary, respectively; κ_s and κ_s' are the corresponding bulk moduli, as described in equations (7) and (8).

The second measured parameter is insertion loss, IL, which is given by:

$$IL = 10\log_{10}\frac{V_{1a}^2}{V_5^2} \tag{54}$$

where V_5 is the voltage applied to the generating transducer and V_{1a} is the voltage obtained at the receiving transducer (see also Figure 2.5).

The two electric voltages are related to the acoustic amplitude by the electromechanical coupling constant, k, of the transducer.[37] This parameter is related to the conversion of mechanical and electrical energies within the generating and receiving transducers, which we assume to be identical. At the generating transducer, where the electrical energy is converted to mechanical energy,

k^2 = (mechanical energy)/(Input electrical energy)

$$k^2 = \frac{\left(\frac{1}{2}\right)\left(\frac{A_5^2}{s}\right)}{\left(\frac{1}{2}\right)\left(\varepsilon_\circ\varepsilon_r\left(\frac{V_5}{d}\right)^2\right)} \tag{55}$$

where s is the elastic compliance; ε_0 is the vacuum permittivity; ε_r is the relative permittivity; V_5 is the input electric voltage; d is the thickness of the piezoelectric material.

Rearranging equation (55), we have,

$$V_5^2 = \frac{A_5^2 d^2}{s\varepsilon_\circ \varepsilon_r k_1^2}. \tag{56}$$

On the other hand, at the receiving transducer, the mechanical energy is converted to electrical energy[37], we have

k^2 = (electrical energy)/ (Input mechanical energy)

$$k^2 = \frac{\left(\frac{1}{2}\right)\left(\varepsilon_\circ \varepsilon_r \left(\frac{V_{1a}}{d}\right)^2\right)}{\left(\frac{1}{2}\right)\left(\frac{A_{1a}^2}{s}\right)}. \tag{57}$$

Rearranging, we have

$$V_{1a}^2 = \frac{A_{1a}^2 d^2}{s\varepsilon_\circ \varepsilon_r k_2^2}. \tag{58}$$

Now we combine equations (56) and (58) with the definition of IL or equation (54), we have

$$IL = 10\log_{10}\frac{A_{1a}^2}{A_5^2} \quad . \tag{59}$$

We combine equations (59) and (45), we have

$$IL = 10\log_{10}\left\{\prod_{j=1}^{n}\frac{\left(Z_{in}^j + Z_j\right)}{\left(Z_{in}^j + Z_{j+1}\right)} e^{ik_j d_j} e^{-\alpha_j d_j}\right\}^2 \quad . \tag{60}$$

The insertion loss difference between the reflection only and absorption with reflection cases are

$$\Delta IL = 10\log_{10}\left\{e^{-\alpha_l d_3}\right\}^2 = \frac{-20(\alpha_l d_3)}{\ln 10}. \tag{60a}$$

By calculating the insertion loss from equation (60a) assuming that all conditions are the same, the theoretical insertion loss curves for reflection only and reflection with absorption are shown in Figure 2.6. The difference of the insertion losses between reflection only and reflection with absorption cases is shown in Figure 2.7. This difference shoes the effect of the absorption term (α term) in the sample, that is, the B and C terms. The difference is below zero which means that when absorption terms applied to the equation, the insertion loss becomes more negative.

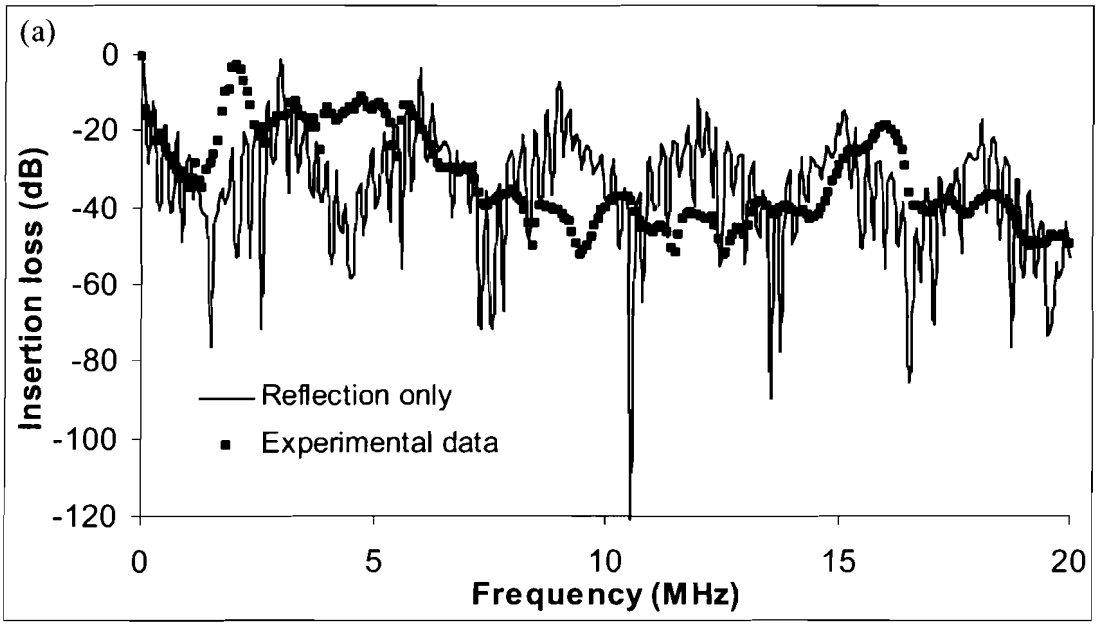

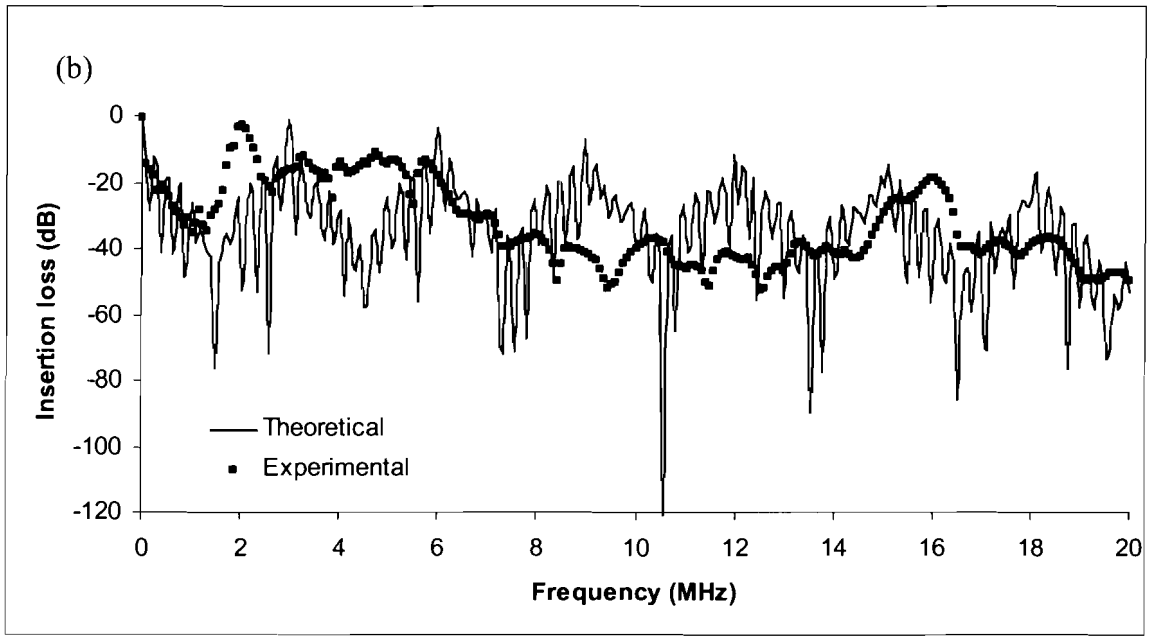

Figure 2.6. The calculated insertion loss of (a) reflection only and (b) reflection and absorption with experimental data in a 250 μm internal diameter capillary.

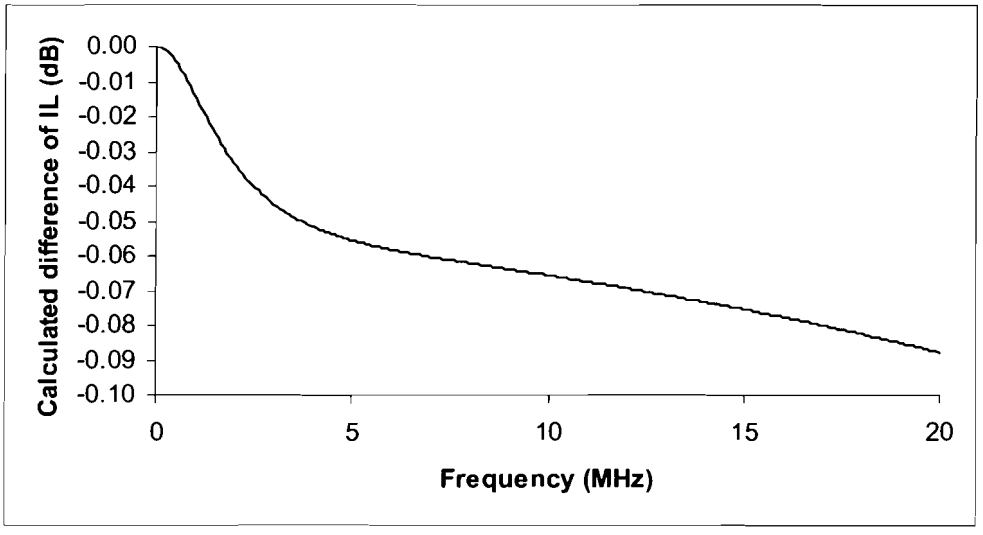

Figure 2.7. The difference of calculated insertion loss between reflection only case (Fig 2.6a) and reflection with absorption estimation case (Fig 2.6b)

Furthermore, the insertion loss estimation shows that the pattern of the curve could be changed due to the dimensions of the capillary and the thickness of the piezoelectric material. There are two kinds of periodic patterns shown in the insertion loss which are governed by the internal diameter of the capillary and the thickness of the piezoelectric material. The destructive

interference of the wave causes a high negative insertion loss, which means that most of the wave energy is not transmitted from one end to the other. Figure 2.8a shows the overlay insertion loss curves of calculated 100μm and 250μm capillary internal diameter. When the internal diameter gets larger, the periodic pattern of insertion loss due to destructive interference becomes more frequent. In addition, the thickness of the piezoelectric material also cause different pattern of the insertion loss profile (see Figure 2.8b). When the piezoelectric disc thickness gets smaller, the periodic pattern of insertion loss becomes more closely spaced on the frequency scale.

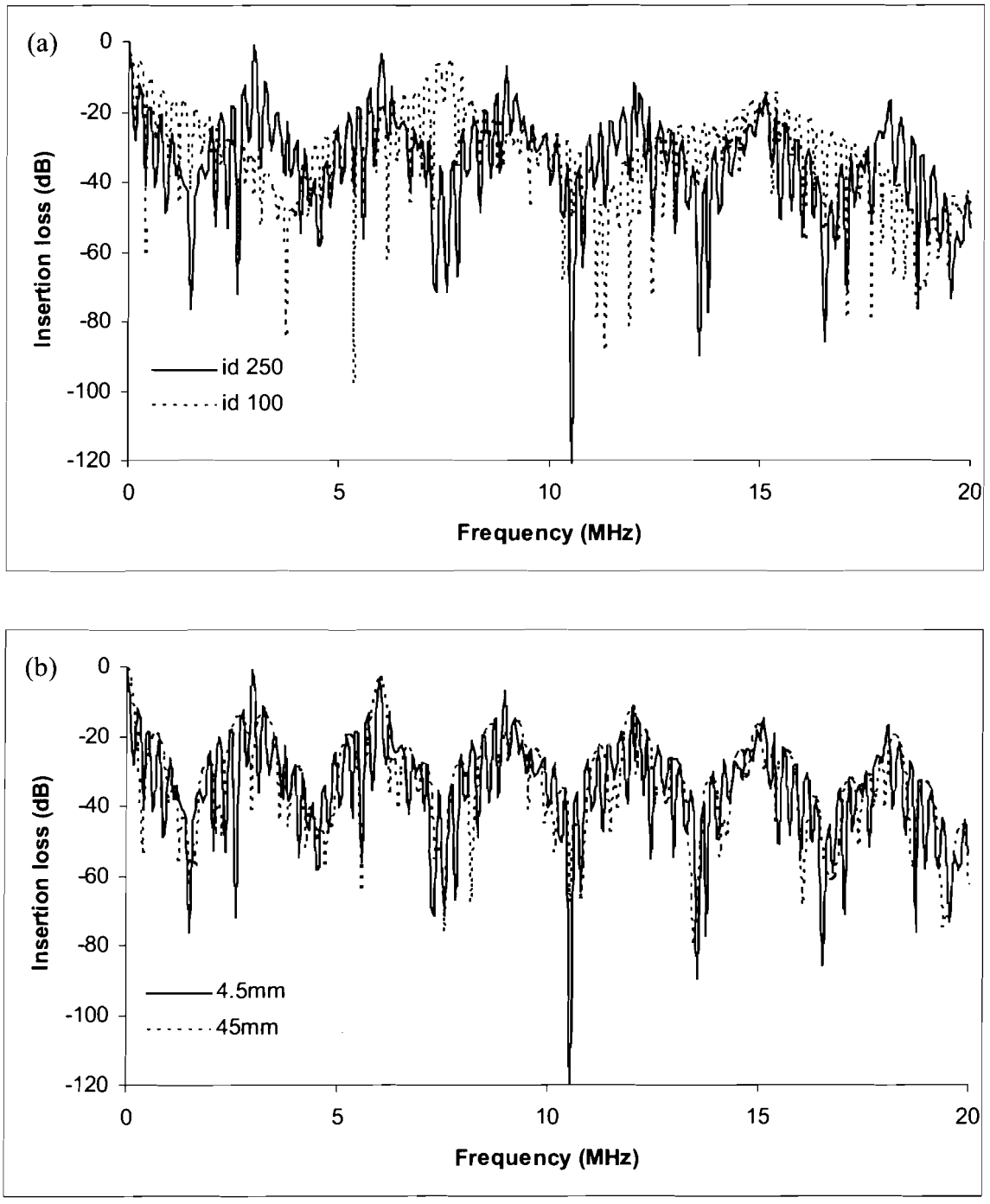

Figure 2.8. (a)The insertion loss profile of 250 μm and 100 μm internal diameter capillary and (b) the insertion loss profile of 4.5 mm and 45 mm thick of piezoelectric material. Experimental condition same as stated in Figure 2.6.

For a change in IL caused by the replacement of liquid 1 (buffer) by liquid 2 (sample),

$$\Delta IL=10\log_{10}\left\{\frac{\left\{\prod_{j=1}^{n}\frac{\left(Z_{in}^{j}+Z_{j}\right)}{\left(Z_{in}^{j}+Z_{j+1}\right)}e^{ik_jd_j}e^{-\alpha_jd_j}\right\}_{sample}}{\left\{\prod_{j=1}^{n}\frac{\left(Z_{in}^{j}+Z_{j}\right)}{\left(Z_{in}^{j}+Z_{j+1}\right)}e^{ik_jd_j}e^{-\alpha_jd_j}\right\}_{buffer}}\right\}^{2} \tag{61}$$

Equation (61) is simplified to give,

$$\Delta IL = 10\log_{10}\left\{\frac{\left\{\frac{\left(Z_{in}^{2}+Z_{2}\right)\left(Z_{in}^{3}+Z_{3}\right)}{\left(Z_{in}^{2}+Z_{3}\right)\left(Z_{in}^{3}+Z_{4}\right)}e^{-\alpha_3d_3}\right\}_{sample}}{\left\{\frac{\left(Z_{in}^{2}+Z_{2}\right)\left(Z_{in}^{3}+Z_{3}\right)}{\left(Z_{in}^{2}+Z_{3}\right)\left(Z_{in}^{3}+Z_{4}\right)}e^{-\alpha_3d_3}\right\}_{buffer}}\right\}^{2}. \tag{62}$$

Equation (62) can be insolated into frequency-dependent and frequency-independent parts, and the equation can be rearrange as,

$$\Delta IL = 20\log_{10}\left\{\frac{\left\{\frac{\left(Z_{in}^{2}+Z_{2}\right)\left(Z_{in}^{3}+Z_{3}\right)}{\left(Z_{in}^{2}+Z_{3}\right)\left(Z_{in}^{3}+Z_{4}\right)}\right\}_{sample}}{\left\{\frac{\left(Z_{in}^{2}+Z_{2}\right)\left(Z_{in}^{3}+Z_{3}\right)}{\left(Z_{in}^{2}+Z_{3}\right)\left(Z_{in}^{3}+Z_{4}\right)}\right\}_{buffer}}\right\} + 20\log_{10}\frac{\left(e^{-\alpha_3d_3}\right)}{\left(e^{-\alpha_3'd_3}\right)}, \tag{63}$$

where α_3' is the absorption coefficient for buffer.

This is further simplified to give

$$\Delta IL = \frac{-20d_3\left(\alpha_3-\alpha_3'\right)}{\ln 10} + 20\log_{10}\left\{\frac{\left\{\frac{\left(Z_{in}^{2}+Z_{2}\right)\left(Z_{in}^{3}+Z_{3}\right)}{\left(Z_{in}^{2}+Z_{3}\right)\left(Z_{in}^{3}+Z_{4}\right)}\right\}_{sample}}{\left\{\frac{\left(Z_{in}^{2}+Z_{2}\right)\left(Z_{in}^{3}+Z_{3}\right)}{\left(Z_{in}^{2}+Z_{3}\right)\left(Z_{in}^{3}+Z_{4}\right)}\right\}_{buffer}}\right\}. \tag{64}$$

This is the relationship correlating the change in the insertion loss, ΔIL, and the various physical constants (α_l', α_l, d_3) based on an oversimplified 1-dimensional approximation. By combining equation (64) with the total acoustic absorptions for the sample and buffer, according to equation (26), we have,

$$\Delta IL = \frac{-20af^2\left\{\left[\frac{(C\tau)}{1+\left(\frac{f}{f_r}\right)^2}-\frac{(C'\tau)}{1+\left(\frac{f}{f_r'}\right)^2}\right]+(B-B')\right\}}{\ln 10}+20\log_{10}\left\{\frac{\left\{\frac{\left(Z_{in}^2+Z_2\right)\left(Z_{in}^3+Z_3\right)}{\left(Z_{in}^2+Z_3\right)\left(Z_{in}^3+Z_4\right)}\right\}_{sample}}{\left\{\frac{\left(Z_{in}^2+Z_2\right)\left(Z_{in}^3+Z_3\right)}{\left(Z_{in}^2+Z_3\right)\left(Z_{in}^3+Z_4\right)}\right\}_{buffer}}\right\} \quad (65)$$

where B', C' and f_r' are the constants of the classical and excess absorption and the relaxation frequency of the buffer, respective, and B, C and f_r are parameters associated with the sample.

We consider the term ($B - B'$) to vanish since the sample and buffer are made in water and the temperatures of both the sample and buffer are the same. This is achieved using a low concentration buffer and a cooling system to suppress Joule heating. Furthermore, the excess ultrasonic absorption due to the buffer, which is $Na_2CO_3/NaHCO_3$, which is the term associated with C' in equation (65), is considered negligible, as confirmed by no observable difference in the signal when comparing the ultrasonic absorption of the buffer and water.

Therefore, equation (65) can be simplified as follows,

$$\Delta IL = \frac{-20d_3f^2\left\{\left[\frac{(C\tau)}{1+(2\pi f\tau)^2}\right]\right\}}{\ln 10}+20\log_{10}\left\{\frac{\left\{\frac{\left(Z_{in}^2+Z_2\right)\left(Z_{in}^3+Z_3\right)}{\left(Z_{in}^2+Z_3\right)\left(Z_{in}^3+Z_4\right)}\right\}_{sample}}{\left\{\frac{\left(Z_{in}^2+Z_2\right)\left(Z_{in}^3+Z_3\right)}{\left(Z_{in}^2+Z_3\right)\left(Z_{in}^3+Z_4\right)}\right\}_{buffer}}\right\}. \quad (66)$$

Hence, the measurements of insertion loss, and of phase, are related to the geometry of the capillary in terms of internal capillary diameters as well as the frequency of the acoustic wave and the acoustic impedance of the buffer and sample solutions.

Using equation (66), the theoretical value of ΔIL between sample and buffer could be estimated. Since the values of B and C for leucine could not be found, the estimation was conducted using the values for glutamic acid. By using the values of

$B = 31.8 \times 10^{-15}$ sec^2 /m, $C\tau = 140 \times 10^{-15}$ sec^2 /m for 0.5 M glutamic acid, the theoretical value of the change of IL can be calculated.[29] C value was calculated to be

1.12×10^{-5} sec/m by the given $C\tau$ and τ values. By equation (66) without the consideration of the second term in the equation, the theoretical absolute value of ΔIL for an amino acid (i.e. 0.5 M glutamic acid) at 16.46 MHz in a 250μm internal diameter capillary was estimated to be 0.273 dB by the values of d_3, f and τ.

The change of IL values is also related to the concentration of the amino acid (see equation 23). The ΔIL of different concentration of glutamic acid was estimated by their own τ, which is related to their concentrations of the amino acid and hydroxide ions, k_f and k_b (see equation 23). The estimated absolute value of the ΔIL for 50mM glutamic acid was found to be 0.066dB. Figure 2.9 shows the ΔIL for 50mM glutamic acid under the influence of different frequencies applied to the system. Figure 2.9 and figure 2.7 have similar shape but the curve in figure 2.9 is less negative due to the addition of the classical absorption term, B.

A ten-time decrease of concentration of the glutamic acid (from 0.5M to 50mM) causes approximately four-time decrease of ΔIL from the model(see figure 2.10). The relationship between the concentration of the amino acid glutamic acid and the difference of insertion loss

will be discussed in section 5.2.3. The experimental value of 50 mM of leucine was found to be 2.2 dB which is higher in absolute value than the estimated value.

In the foregoing discussion, the coupling between the transducer and the capillary is assumed to be perfect. In fact, there is glue between the transducers' and capillaries' surfaces, and air may get trapped between the two surfaces during gluing. These conditions could result in more than five media with more reflections occurring at the various interfaces. In this regard, the square capillary will provide a better coupling than the circular capillary.

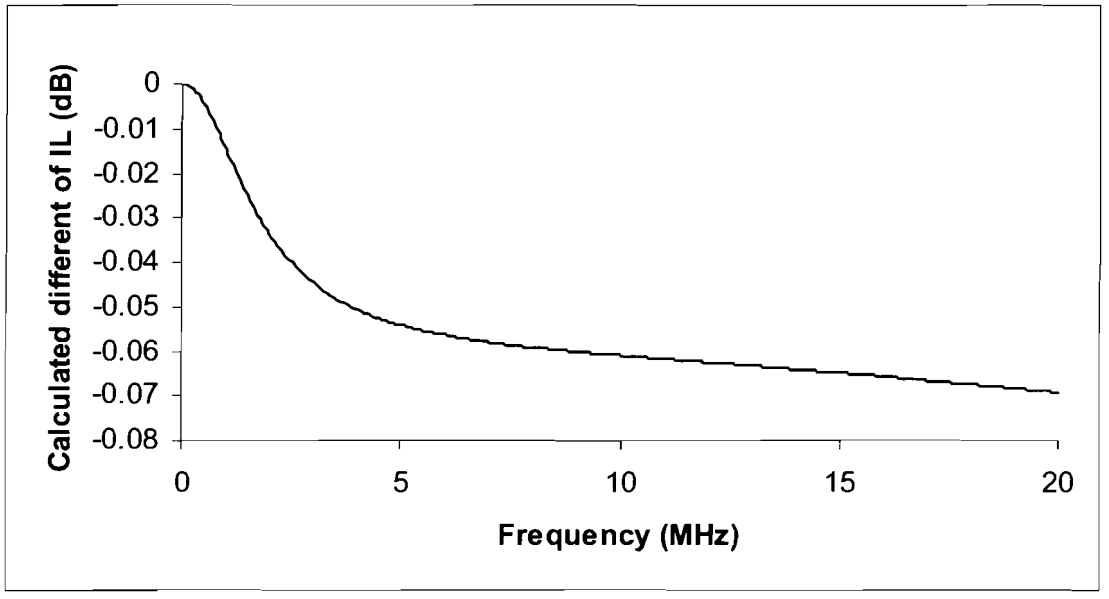

Figure 2.9. The difference of insertion loss between buffer and sample in a 250 μm internal diameter capillary.

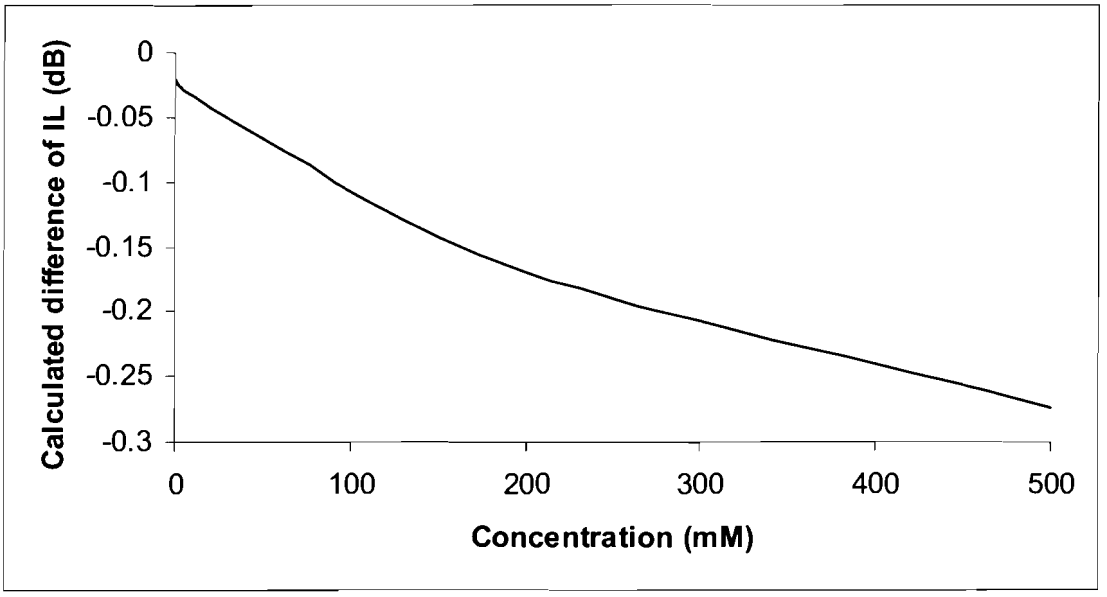

Figure 2.10. Calculated insertion loss difference plotted against concentration of amino acid with the difference of insertion loss in a 250 μm internal diameter capillary (based on equation 23 and 24).

CHAPTER THREE:
MATERIALS AND INSTRUMENTATION

3.1 Chemicals and reagents

All solutions were prepared using Nanopure ultrapure water (Barnstead, Dobuque, IA). CE running buffers were prepared from reagent-grade sodium carbonate, $Na_2CO_3 \cdot H_2O$, sodium hydrogen carbonate, $NaHCO_3$ (BDH Inc.), borax, $Na_2B_4O_7.10H_2O$ (Sigma), and 4-(2-Hydroxyethyl)-1-piperazineethanesulfonic acid (HEPES). TLC-grade L-amino acid (Sigma) solutions were prepared as samples. Sodium dodecyl sulfate, Brij 35 and Triton X-100 (Sigma) were used as buffer additives.

3.2 Instrumentation

The acoustic wave detector was coupled to the capillary electrophoretic system built in-house. Three different kinds of capillaries (1.circular capillary with 100μm internal diameter and 166μm external diameter; 2. circular capillary with 250μm internal diameter and 360μm external diameter; 3. square capillary with 100μm x 100μm internal dimension and 300μm x 300μm external dimension) were used to perform capillary electrophoresis. A high voltage power supply (Spellman CZE2000, Hauppauage, NY) was used to generate electrokinetic migration of chemical species[38].

The general instrument setup, which includes the CE system, the acoustic wave detector and the temperature measurement system, is shown in figure 3.1. The two ends of the capillary tubing were placed into two buffer vials with Pt electrodes. A high voltage power supply was used to

generate a liquid flow inside the capillary tube to carry the analytes to the detection zone. The two acoustic wave transducers sandwiched the capillary at the detection zone which is situated at 41.1 cm from the capillary inlet. The close-up of the detection zone has previously been shown in figure 1.9.

The acoustic wave detection apparatus was constructed using two piezoelectric transducers for generating and receiving ultrasonic acoustic waves. Two different kinds of transducers were used in this study. First, two 2 MHz piezoelectric longitudinal transducers (Valpey Fisher, Hopkintion, MA) made of lead zirconate titanate (PZT), were used. Glass horns were employed to facilitate the coupling between the larger surface of the transducer (1cm) and the small contact surface of the capillary. The glass horns were 4 mm in diameter and were bonded to the transducer surfaces using a cyanoacrylate adhesive: Loctite 495 instant adhesive super bonder (Loctite, Mississauga, ON). The tips of the glass horns were bonded to the outer surface of the capillary using the same cyanoacrylate adhesive. The two glass horns were aligned opposite each other to maximize the signal transmission.

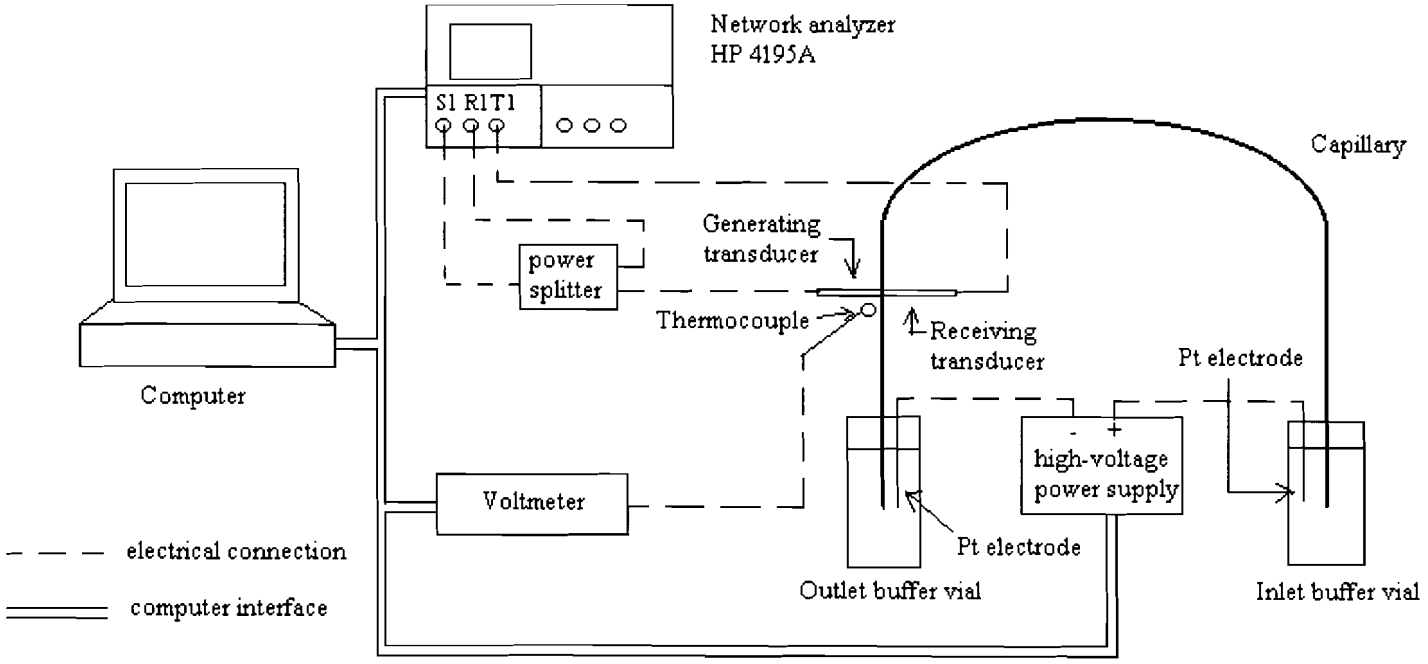

Figure 3.1. Schematic diagram of the entire experimental setup

Second, instead of using 2MHz piezoelectric longitudinal transducers, 10 MHz piezoelectric longitudinal pinducers were used. Because of the small sizes (1.6mm in diameter), the ends of the pinducers were directly bonded to the surface of the outer wall of the capillary. In a similar manner to the transducer-glass horn assembly, the two pinducers were aligned opposite each other to obtain the signals. Real-time insertion loss and phase profiles were obtained from the network analyser to ensure there was wave propagation from the generating pinducer through the capillary to the receiving pinducer.

A network/spectrum analyzer (HP4195A, Agilent Technologies, Palo Alto, CA) was connected to the generating and receiving transducers. The source electric voltage was split and one was directed to the reference port R1 as a control, and the other part supplied to the generating transducer and recorded as input electric voltage (V_i) (see Figure 3.1). This electric voltage was supplied to the generating transducer to generate the acoustic waves. These waves propagated across the detection zone to the receiving transducer, and an electric voltage was measured at the receiving transducer (V_o). The electric voltage from the receiving transducer was amplified before being fed to detector port T1. The network analyzer was used to measure changes in insertion loss and phase angle between the two electric voltages (V_o and V_i) at the two transducers. The voltages of the reference R1 and of the receiving transducer T1 were compared to generate the insertion loss and phase angle data, as illustrated in Figure 3.1. These changes in insertion loss and phase angle were used to qualify the acoustic properties of the solute.

Since an electric current passing through the capillary would generate Joule heat, temperature measurement was necessary. In order to measure the temperature near the detector zone, a thermocouple was placed at 2 mm beside the capillary at the detection zone. The thermocouple

was connected to a voltmeter for measurement. An electrical fan was also mounted and placed close to the detection zone (~5 mm) to dissipate the Joule heat generated by CE near this area.

All the data from the acoustic detector and thermocouple were collected by a computer via a GPIB card and a NI-DAQ card, respectively. An instrument control and data acquisition program, LabVIEW 5.1 (National Instruments, Austin, TX), was used to display the insertion loss and phase angle acoustic wave signals at three selected frequencies as well as the voltage, current, and temperature measurements in real-time.

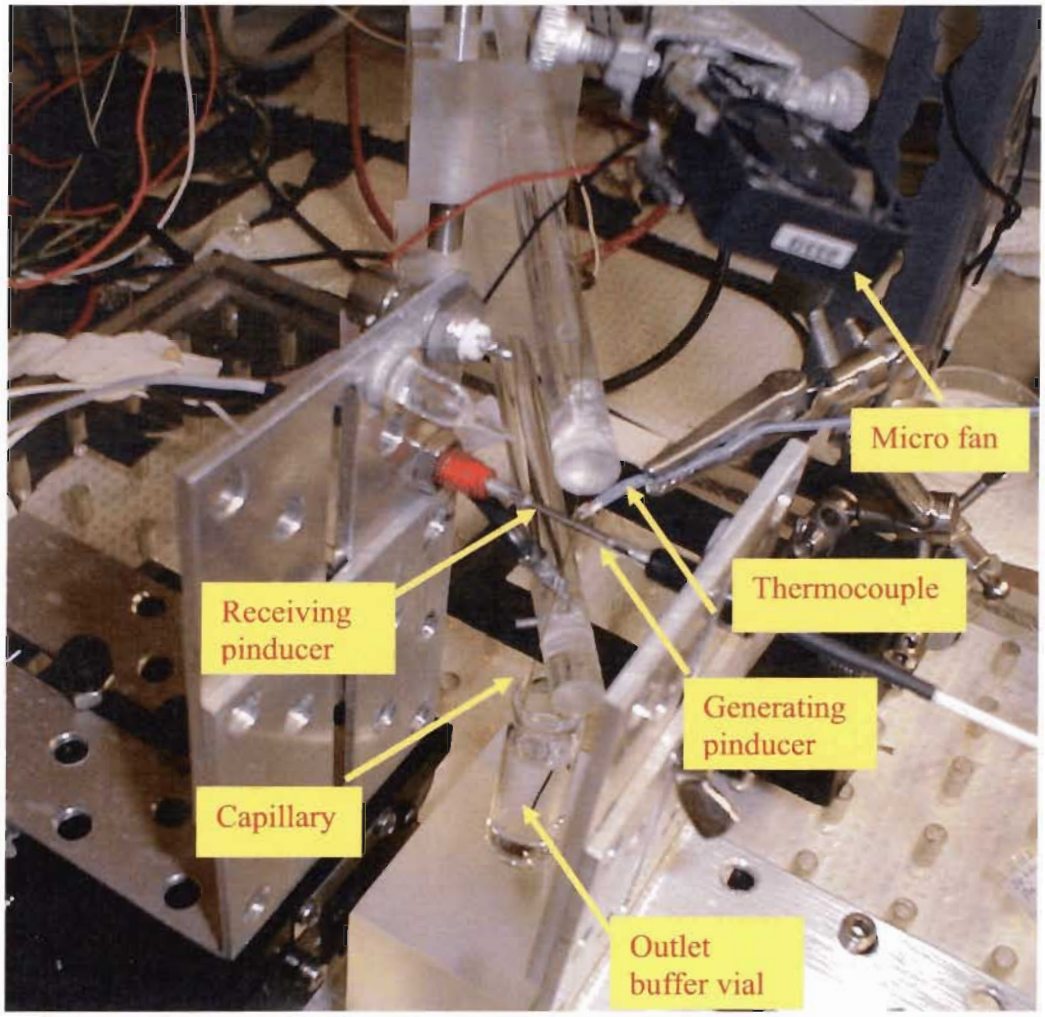

Plate 1. Experimental setup of the acoustic detector and thermocouple

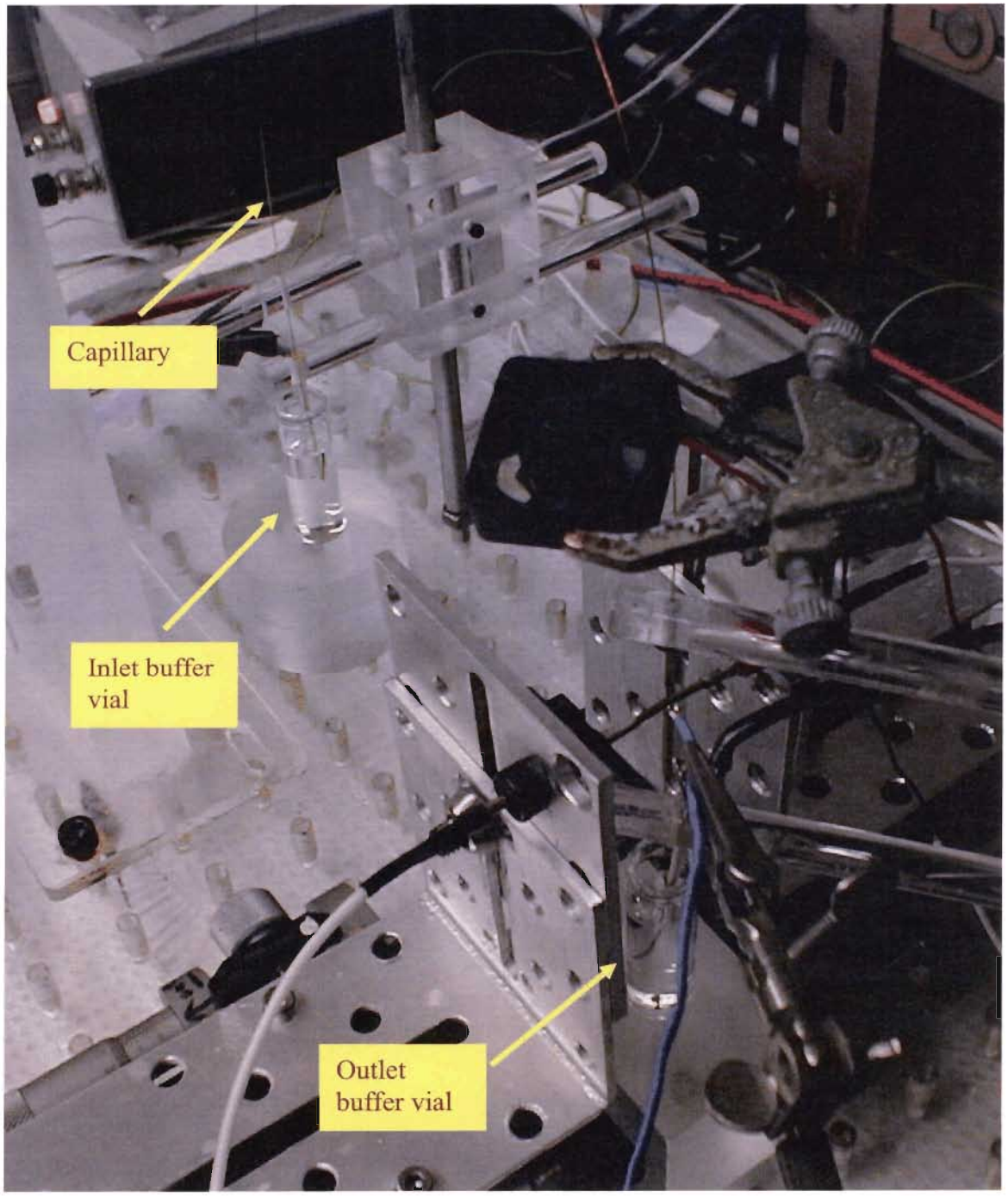

Plate 2. Experimental setup showing the capillary electrophoretic system

CHAPTER FOUR:
EXPERIMENTAL PROCEDURES

4.1 Acoustic wave generation and detection

The generating and receiving transducers were mounted on translation stages. This allowed the two glass horns or pinducers to be precisely aligned with the outer wall of the capillary and opposite to each other. The polyimide coating of the capillary was removed using a flame to create a direct contact between the surface of the glass horn tips / pinducer tips with the outer wall of the fused silica capillary. It was found that the coupling between the transducers and the capillary is enhanced, resulting in an increase in the signals. Once the alignment was precise, cyanoacrylate adhesive was applied to the contact surface of the tips and the capillary for bonding. This bonding ensured that the acoustic energy from the generating transducer travelled through the capillary to the receiving transducer. If disassembly was necessary, acetone was applied to dissolve the cyanoacrylate adhesive between the transducer surfaces and the outer wall of capillary.

4.2 Phase and insertion loss measurements

The insertion loss is related to transduction loss and propagation loss. Transduction loss is caused by the mismatch between the electrical impedance of the transducers and the acoustic impedance of the transducer glass-horn assembly and the capillary. Propagation loss is caused by the attenuation of the acoustic wave between the two transducers due to ultrasonic absorption. On the other hand, the change in phase angle is due to the change in the phase velocity, which is related to the density change of the solution in the capillary. These two measurements, insertion

loss and phase, provide information about the perturbation of the acoustic wave when the analytes pass through the capillary.

The network/spectrum analyzer was set in the network mode for both insertion loss and phase measurements. It was calibrated with an "open" and "through" connection using the BNC cables. All the calibrated parameters were saved in a "state" file using the built-in floppy drive. When the instrument was turned on for the day, the calibration parameters were loaded to the network analyzer for experiments. The network analyzer is able to measure the ultrasonic signals at 255 frequencies.

As for the excitation of the transducer, if it has a nominal frequency at 2MHz, we would set the frequency range of the instrument from 0 to 3 MHz. However, there were external mechanical factors, such as the coupling between the transducers and the capillary tubing, which would alter the frequency at which strong acoustic wave transmission occurred. In other words, the frequency that there was a strong acoustic transmission or low insertion loss was changed from the nominal frequency to some other frequencies. The insertion loss and phase profile of the 2MHz transducers coupled with the capillary is shown in Figure 4.1. The insertion loss in decibels (dB) was plotted on the left vertical axis against the frequency over a range of 0 – 3 MHz. As the acoustic power that could pass through the capillary increased, a lower (or less negative) value of insertion loss was observed; these situations were unusually depicted as local maxima on the insertion loss profile.

Before data acquisition, three frequencies were selected as depicted by three arrows on the local maxima shown in Figure 4.1. This experimental mode is called the manual-frequency mode at three frequencies. This mode is further discussed in section 4.3. However, the capability of the network analyzer allowed us to collect the data at 255 frequencies, which we called the sweep-frequency mode. From these data, the frequency at the local maxima of insertion loss might not

necessarily produce the large insertion loss changes in our experiments. For instance, from the insertion loss profile, the three high insertion losses occurred at around 330 kHz, 957 kHz and 1.48 MHz; whereas the large insertion loss change occurred at the frequencies of 343 kHz, 1.52 MHz and 1.77 MHz. Since it was desirable to obtain a large signal, the three frequencies that produced large changes of insertion loss were chosen for subsequent experiments. We called the frequency at which a large change in insertion loss occurred, the high-response frequency.

The selected frequencies were not exactly the same when the setup was re-assembled when re-bonding the glass horns with a new capillary was required. It was due to the non-uniform bonding and non-identical coupling between the glass horns and capillary. Hence, the insertion loss profiles were not exactly the same after various constructions. In any case, only the high-response frequencies were selected from the experimental data for each experimental configuration.

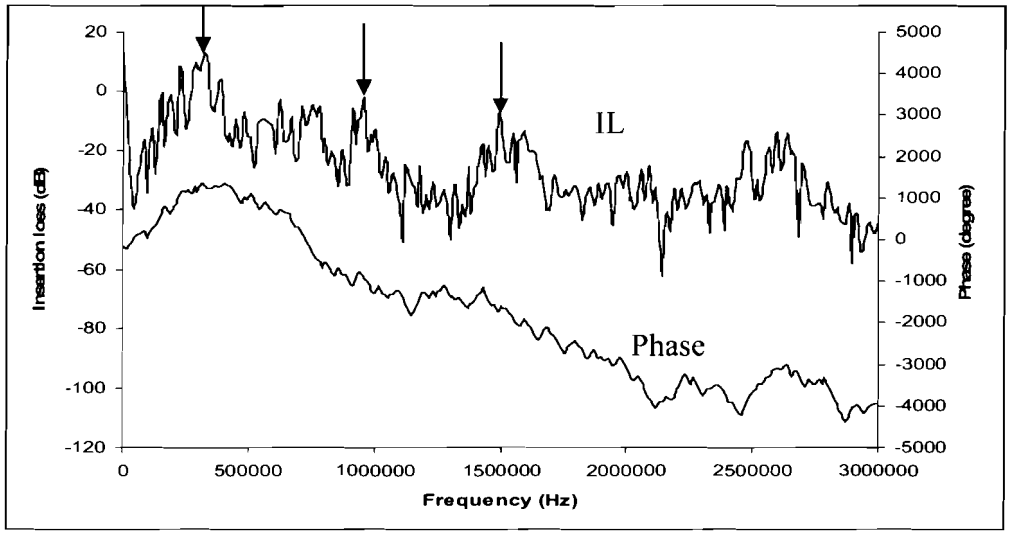

Figure 4.1. Insertion loss and phase profiles for 2 MHz piezoelectric transducer glass-horn assembly. Top trace shows the insertion loss and the bottom trace shows the phase profile (Negative insertion loss value refers to an insertion loss defined in equation (53)). The negative phase means the V_o vector lags behind the V_i vector.

4.3 Data acquisition

With the data from 255 frequencies monitored in the background, the acoustic wave insertion loss and phase at three high-response frequencies were monitored from the computer screen simultaneously with the temperature, current and voltage measurements. These data were stored in three different files for each experiment.

The LabVIEW 5.1 program used for the previous manual-frequency mode was modified to the present sweep-frequency mode. In the sweep mode, data from 255 frequencies were obtained in one experiment, rather than from only three frequencies as in the manual-frequency mode. The insertion loss and phase angles of different frequencies were simultaneously recorded. By obtaining information from different frequencies (say 255) using the sweep-frequency mode, it minimized the errors arising from many manual-mode experiments each at three frequencies (say 85, since 3 x 85 = 255). This was because the data obtained by sweep-frequency mode was collected under the same conditions of electrokinetic migration within the capillary. By comparing the data from the manual-frequency mode and sweep-frequency mode, similar migration time and shape of the peak(s) were obtained. Although better baseline and larger signal-to-noise ratio were obtained in the manual-frequency mode, the sweep-frequency mode was used since more frequencies could be obtained in one experiment, providing sufficient data for further analysis.

4.4 Capillary washing and conditioning

The capillary was washed and conditioned when it was mounted into the CE setup. The washing and conditioning processes ensured that a uniform negative charge was formed on the inner wall of the capillary. Washing solutions were introduced into the capillary using a syringe (3mL) connected to a glass adapter. The capillary was rinsed first with 0.1M HCl, followed by

deionized water, then with 0.1M NaOH, again followed by deionized water, and finally filled with the run buffer. Afterwards, both ends of the capillary were placed into buffer vials and the positions of the ends were kept at a similar height to minimize the liquid flow due to siphoning. A high-voltage power supply was switched on until a constant current was obtained at a constant flow. When there were spikes or baseline fluctuations obtained, the capillary was washed again with 0.1 M HCl, deionized water, 0.1M NaOH, and deionized water.

4.5 Sample introduction in CE

Small sample volumes (in the nanoliter range) were introduced into the capillary by the hydrodynamic method. This was carried out by putting the inlet end of the capillary into a vial containing the sample. Then the inlet end was raised by a height of 13cm for 100-μm-id capillary, or 6.5 cm for the 250-μm-id capillary. The difference in height between inlet and outlet ends of the capillary created a pressure difference between the two ends, and the sample was pulled into the capillary from the inlet end. The sample was introduced within a specific period of time and the inlet end of the capillary was placed back into the inlet buffer vial. Then the position of the inlet end was adjusted to the same height as the outlet end.

The volumes of sample introduced into the capillary could be altered with several factors (e.g. the introduction time (t) and the diameter of capillary (d)) in hydrodynamic introduction, as given in equation (67) and (68). Assuming a laminar flow occurred in the capillary, the volumetric flow rate, Q, was calculated using the Poiseuille's equation:

$$Q = \frac{\Delta P \pi (2a)^4}{128 \eta L} \tag{67}$$

where ΔP is the pressure difference across the capillary; a is the inner radius of the capillary; η is the viscosity of the sample; L is the length of the capillary.

Then, the sample volume introduced into the capillary, V, could be estimated by:

$$V = \frac{\rho g H \pi (2a)^4 t}{128 \eta L} \tag{68}$$

where ρ is the sample density; g is the acceleration due to gravity; H is the height that the sample is raised; a is the internal radius of the capillary; t is the time the sample is raised; η is the viscosity of the sample; L is the length of the capillary.

The sample plug length was another important parameter. If the sample plug is long, a broad peak will result. The separation of analytes would be impaired in terms of resolution and efficiency. As previously reported, the sample plug length should not be longer than one tenth of the total capillary length[2,3]. The sample plug length, L_p, is calculated by:

$$L_p = \frac{4v}{\pi (2a)^2} \tag{69}$$

where v is the sample volume and a is the internal radius of the capillary.

In our experiments, the inlet end of the capillary was raised by 13cm or 6.5cm for 100-μm-id and 250-μm-id capillary, respectively, relative to the outlet end of the capillary. The pressure difference caused the sample to be introduced into the capillary. The use of different sample introduction times resulted in different amounts of sample injected. For instance, the injected volume of the analyte was about 0.4 μL for both 250-μm-id and 100-μm-id capillary for the 3- and 60-second injections, respectively, see appendix 2. In addition, the corresponding sample plug lengths were 0.84cm and 5.3cm.

4.6 Electrophoretic migration and separation

After sample introduction, the LabVIEW 5.1 program was used to monitor and collect the data obtained from the network analyzer. The program was initiated with the record of experimental information, such as file name, sample name, sample introduction time, voltage applied, run buffer and temperature controlling condition. Then, the program started to collect and plot the data in real time. The high-voltage power supply was switched on when the time counter on the program reached 1.0 or 3.0 minute(s). Electrophoresis and sample separation occurred inside the capillary until the sample had migrated to the detection zone (41.1cm from the inlet), and finally appeared at the outlet. The power supply was then switched off and no current was obtained. The program was terminated, and the data was analyzed and plotted with Microsoft Excel.

4.7 Temperature controlling and monitoring

Temperature controlling and monitoring were necessary for the development of the acoustic wave detector. As a high voltage was applied to the CE system, an electric current flowed and Joule heat was generated in the capillary. Since an increase in temperature would affect the insertion loss and phase signals, the temperature of the capillary around the detection zone was controlled by employing a micro-fan. Therefore, the Joule heat generated by the CE system was dissipated. This decreased the variations of the insertion loss and phase measurements due to Joule heating. The temperature was monitored by the LabVIEW program.

CHAPTER FIVE:
RESULTS AND DISCUSSION

5.1 Optimization of acoustic wave detection system

The CE acoustic wave detector was constructed and optimized in three ways, the type of transducer, the buffer conductivity and the capillary diameter. First, the 2MHz -transducer glass-horn assembly was replaced with the 10MHz pinducers. It was found that the difference in the coupling surface between the transducers and the outer wall of capillary affected the acoustic wave insertion loss and phase signals. In addition, the frequency range was increased when the 10-MHz pinducers were used. Second, a low-conductivity buffer was used to minimize the Joule heat generated in the capillary. Hence, any interference of the acoustic wave signals by the thermal change was eliminated. Third, capillary electrophoresis was performed with two different internal diameter capillaries. It was found that the capillary with the larger diameter gave greater acoustic wave signals. The details of these optimizations are given in subsequent sections.

5.1.1 Transducer glass-horn assembly versus pinducers

One major parameter that was measured in the acoustic wave detection system was the insertion loss. This loss results from the energy loss due to imperfect transduction and the attenuated propagation. The former can be caused by the mismatch of the acoustic impedance between the transducers and the capillary; whereas the latter can be the result of the attenuation of the acoustic wave in the path between the two transducers. The mismatch and attenuation could be due to the coupling of each transducer with the capillary and the alignment of the two transducers.

Therefore, by reducing the mismatch between the transducers and capillary as well as the attenuation between the two transducers, the insertion loss and also the phase signals could be optimized.

In earlier work, a glass horn was glued to the transducer surface for coupling between the large transducer surface and the small capillary. The schematic diagram of the transducer glass-horn assembly is shown in Figure 5.1a. In later work, the experimental setup was constructed by replacing the transducer glass-horn assembly with pinducers. The pinducers were small and rod-like, with the piezoelectric materials on the tips (see Figure 5.1b). The pinducers were directly glued to the outer wall of the capillary, and so a glass horn was not needed. The use of pinducers resulted in a better coupling between the transducer and the capillary, and a lower insertion loss was resulted.

A comparison between the insertion loss profile from the pinducers and the transducer glass-horn assembly is shown in figure 5.2. Water was injected as a sample, and a peak in the CE was obtained in the insertion loss profile. The pinducers provided a signal that was 2-3 times stronger than that obtained from the glass-horn transducers. The signal-to-noise ratio obtained from the pinducers was also greater than that from the transducer glass-horn assembly. The change in insertion loss was caused by Joule heating, which will be described in details in section 5.1.2. The change in phase, which was due to the density difference between the water sample and the run buffer, was also enhanced.

Furthermore, the insertion loss was obtained in a wider frequency range of 0 – 20 MHz when the 10-MHz pinducers were used. The high-response frequencies for the pinducers were found to be 4.06 MHz, 4.13 MHZ and 5.04 MHz, with the signal from 4.06 MHz shown in Figure 5.2.

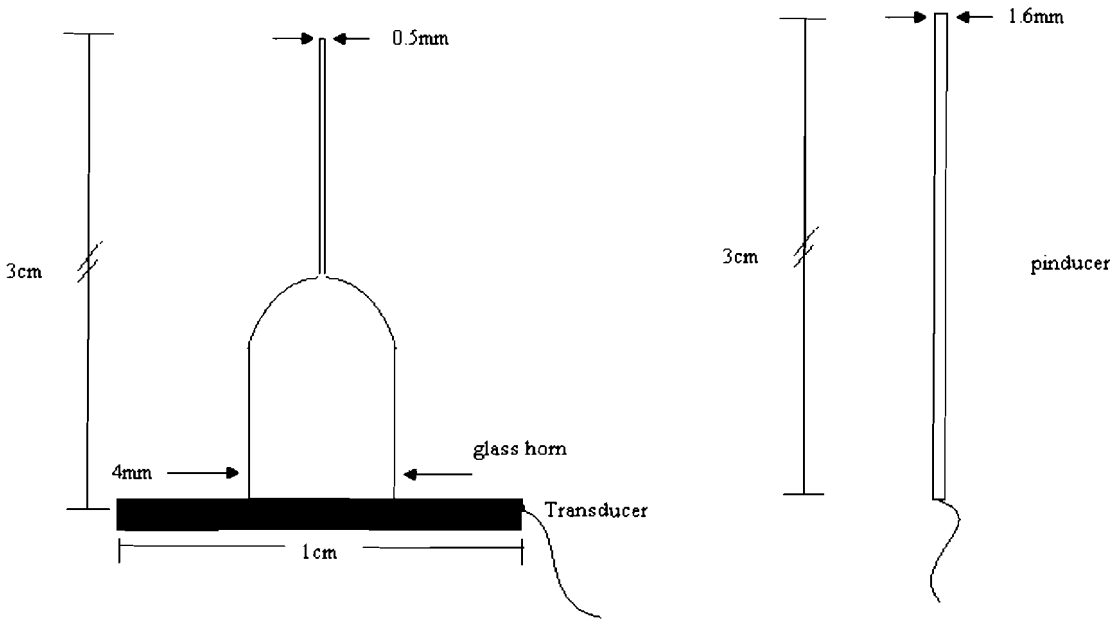

Figure 5.1. Schematic diagram of (a) transducer glass-horn assembly and (b) pinducer

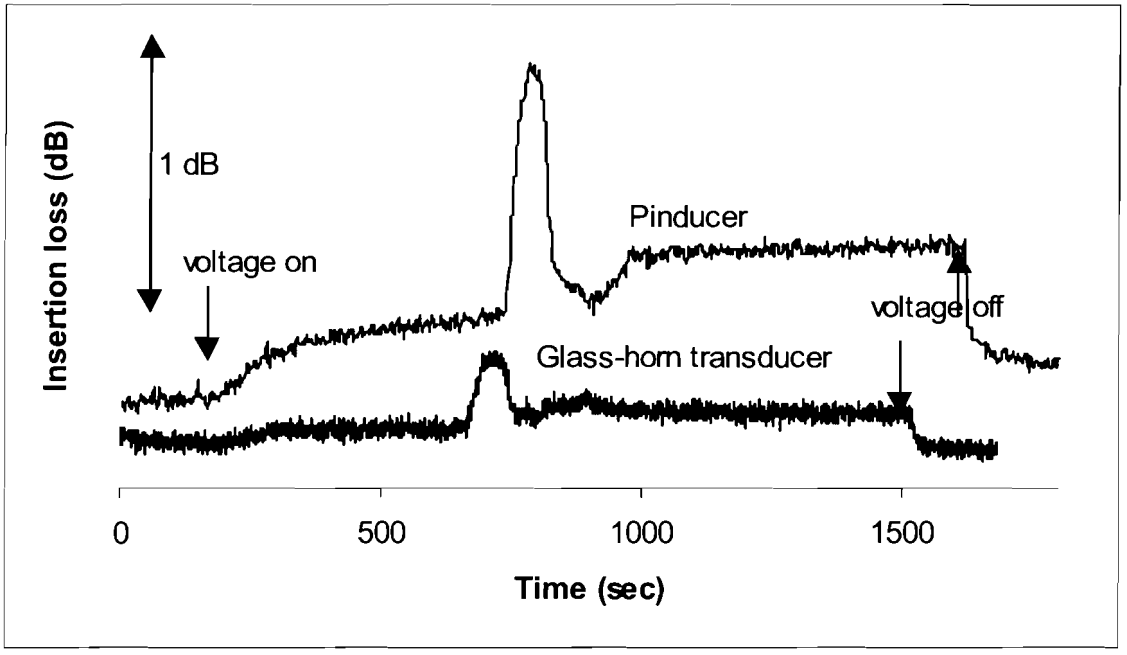

Figure 5.2. Comparison of insertion loss signals of a water plug using the transducer glass-horn assembly and the pinducers. Experimental conditions: capillary, 50.0 cm, id 100 µm, od 166 µm, distance to detector, 41.1 cm; applied voltage, 5kV; run buffer, 12.5 mM sodium carbonate/sodium bicarbonate, pH = 9.0; frequency, 4.06 MHz (pinducers), 1.52 MHz (transducer glass-horn assembly); injection time, 60s.

We concluded that the use of pinducers allowed for a better acoustic coupling of the ultrasonic wave, and there was a wider frequency region to monitor the changes in insertion loss. Therefore, the pinducers were used in all subsequent experiments.

5.1.2 The thermal effect

In order to describe the thermal effect on the acoustic wave measurement, we first describe the variations of capillary current and temperature during electromigration of the sample in the capillary. The measurements of current, voltage and temperature provided the necessary information. The voltage measurement was used to ensure that a stable voltage was provided to the CE system for migration of the injected sample from inlet to the detection zone and then to the outlet. The current measurement provided the information about the current when the analytes migrated and exited through the outlet. In figure 5.3a, the current was plotted against the time. When a high voltage was applied to the CE system at 180s, a current was generated inside the capillary (see Figure 5.3a situation A). The slow increase in current at the beginning was due to the solution plug movement inside the capillary tube, leading to a slow decrease in solution resistance to a steady state value. This is a well known phenomenon called stacking effect in CE separation (reference 3). Furthermore, there was gradual Joule heating effect occurring inside the capillary (see Figure 5.3a situation B). Then, there was a sharp current increase (see Figure 5.3a situation D) followed by a plateau (see Figure 5.3a situation E) and finally the current returned to zero. This plateau indicated that the injected sample plug in the capillary had left the outlet, resulting in a constant high-conductivity environment due to the buffer inside the capillary.

The sample plug was sandwiched by the run buffer and travelled towards the detection zone. As the sample plug arrived at the detection zone, the insertion loss and phase signals would change. In the mean time, the current was steady (see Figure 5.3a situation C). The current increased when the sample plug exited the capillary from the outlet (see Figure 5.3a situation D). The

increase of current was due to the increase of the solution conductivity inside the capillary when the lower conductivity sample plug exited through the outlet. Therefore, the increase of the current indicated the exit of the sample plug form the capillary. Note that the migration time of the sample plug exiting the capillary (~1000 seconds, see Figure 5.3a) and that of the sample plug arrival time at the detection zone (~800 seconds, see Figure 5.3b) are correlated with the distances from the inlet to detection zone (41.1cm) and the distance from the inlet to the outlet (50.0cm).

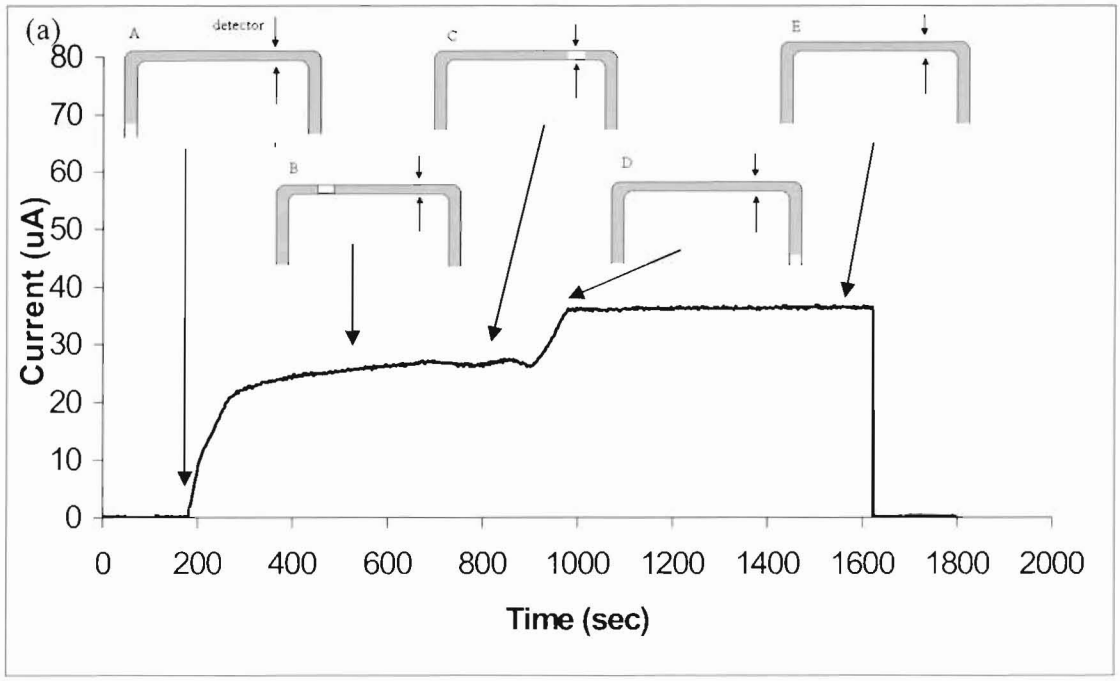

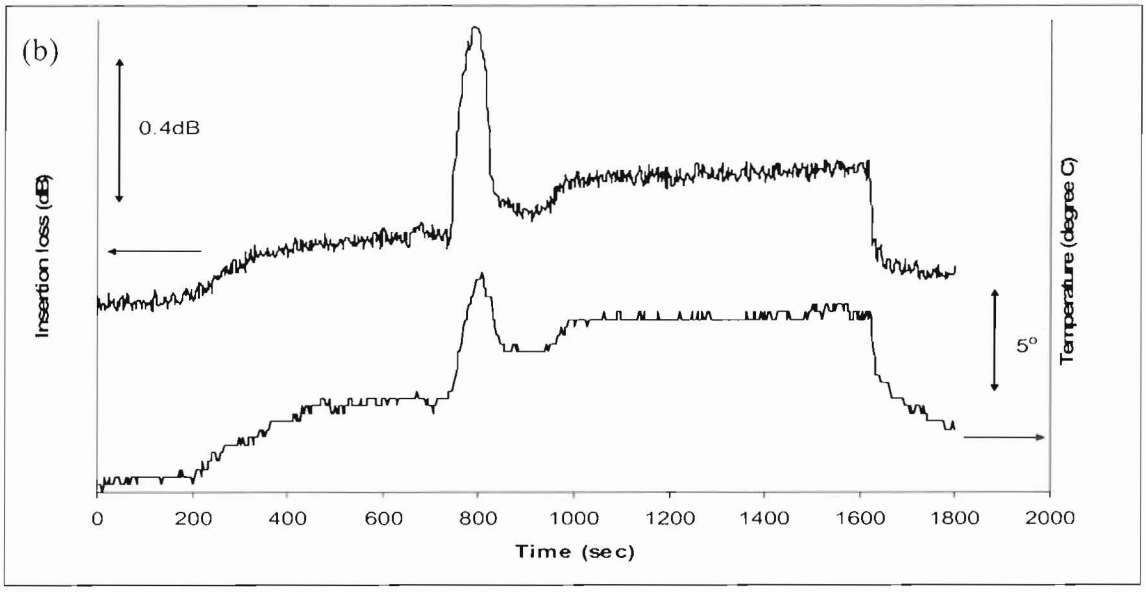

Figure 5.3. (a) Current profile and (b) insertion loss and temperature profiles of a water plug using the pinducers. Experimental conditions: capillary, 50.0 cm, id 100 µm, od 166 µm, distance to detector, 41.1 cm; applied voltage, 5kV; run buffer, 12.5 mM sodium carbonate/sodium bicarbonate, pH = 9.0, frequency, 4.06 MHz.

The temperature measurement was used to indicate the thermal variation occurring at the detection zone of the capillary. Due to the high voltage supplied to the CE system, Joule heat was generated in the capillary. A current versus voltage plot is shown in Figure 5.4. In the 0 to 5kV region, there was a linear relationship between the current generated in the system and the voltage applied to it. Beyond 5kV, the plot deviated from linearity. This deviation was due to excessive heating – Joule heating[2]. Therefore, in order to minimize the heating effect, CE was carried out at voltages below 5 kV.

Even though the heating effect is minimized, the Joule heating would increase the temperature of the sample plug to a greater extent than the surrounding buffer due to the conductivity difference between the surrounding buffer and the sample plug (see situation C in Figure 5.3a).[2] The differential temperature could cause an erroneous insertion loss reading, not by the alteration of acoustic energy loss, but by the change of acoustic velocity by heat. This effect can be seen in Figure 5.3b, in which the changes of insertion loss and temperature occurred at the same time. The effect from the differential Joule heat was termed as thermal effect, and so the peak was termed a thermal peak. This thermal effect can be minimized by further suppressing Joule heat by using a buffer with a low concentration. With the use of the low-concentration buffer (1mM), the Joule heat was minimized, and so was the differential heat. As shown in Figure 5.5, the thermal peak was not observed. In addition, a cooling fan was used. Although its use did improve the signal when a high conductivity buffer was used, it did not appear to provide additional benefits when a low conductivity buffer was used.

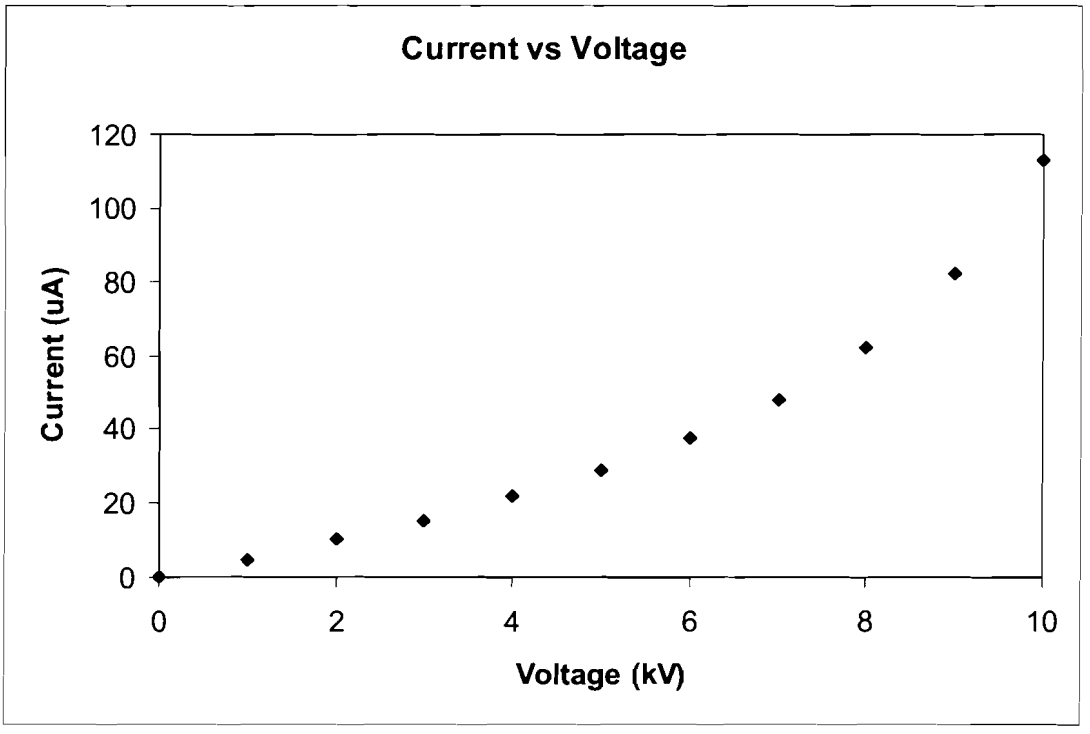

Figure 5.4. Current vs. voltage plot. Experimental conditions: capillary, 50.0 cm, id 100 µm, od 166 µm, distance to detector, 41.1 cm; applied voltage, 0-10kV; run buffer, 12.5 mM sodium carbonate/sodium bicarbonate, pH = 9.0.

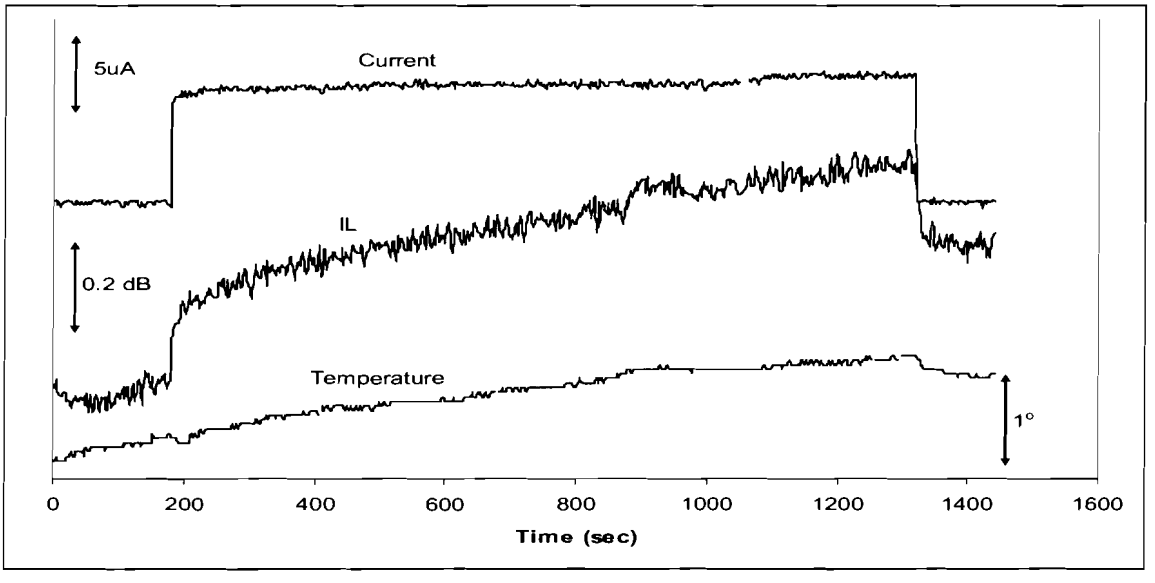

Figure 5.5. Current, insertion loss and temperature profiles of a water plug using the pinducers. Experimental conditions: capillary, 50.0 cm, id 100 µm, od 166 µm, distance to detector, 41.1 cm; applied voltage, 3kV; run buffer, 1 mM sodium carbonate/sodium bicarbonate; frequency, 16.46 MHz.

5.1.3 Capillary diameter

The diameter of the capillary has a significant impact on the acoustic wave detection. If the diameter was larger, the acoustic detection path length was increased. According to equation (26), the insertion loss measurement is due to few different parameters and one is capillary diameter.

As shown in Figure 5.6, the insertion loss and phase signals from the 250-μm-id capillary resulted in greater signals as compared with that of the 100-μm-id capillary. It should be noted that the migration time of the sample was different in the two capillaries; the sample migrated at ~900 s in the large capillary but at ~600 s in the small capillary (see the arrows in Figure 5.9). It was because a high voltage (10kV) was applied to the smaller capillary system, thus leading to a shorter migration time. The phenomenon that the signal peaks was either positive or negative was caused by the frequency response of the acoustic wave signal, as described in detail in section 5.2.4.

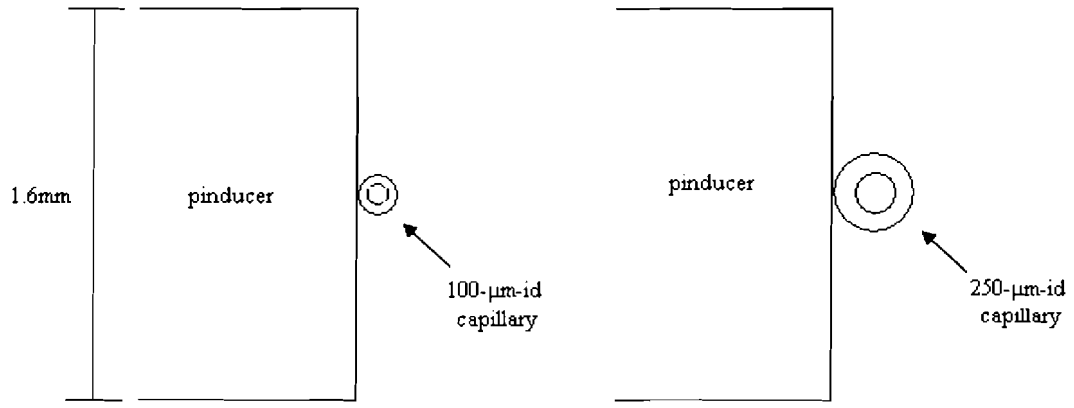

Figure 5.6. Coupling between pinducer and (a) 100-μm-id capillary (b) 250-μm-id capillary

Although experimental conditions had some differences, such as the monitoring frequencies and the sample introduction time, the two cases were still comparable. First, the frequencies compared were the high-response frequencies in each capillary configuration (16.46MHz in the 250-μm-id capillary versus 4.13MHz in the 100-μm-id capillary). Second, by calculations, the injected sample amounts were similar in the large and small capillaries using the sample injection times of 3 s and 60 s, respectively. We have calculated using equation (68), the injection time of 3s in 250-μm-id capillary was equivalent to 60s in 100-μm-id capillary in terms of sample plug volume (see appendix 2).

From a previous study,[38] as the internal diameter of the capillary increased, the insertion loss and phase angle measurements increased. According to the equation (66) in section 2.7, as the internal diameter of the capillary increases, the insertion loss change should increase as well, and the change should be about 2.5 times larger in the case of the larger capillary. However, the insertion loss change from the larger capillary was about 10 times larger than that from the smaller capillary (see Figure 5.7). A possible reason for the additional signal enhancement was a better coupling between the capillary wall and the pinducers. As shown in Figure 5.6, the curvature of the larger capillary was smaller, and the space for gluing the pinducer to the capillary was greater. Accordingly, this would result in a better coupling to the pinducer, thus further enhancing the acoustic signals.

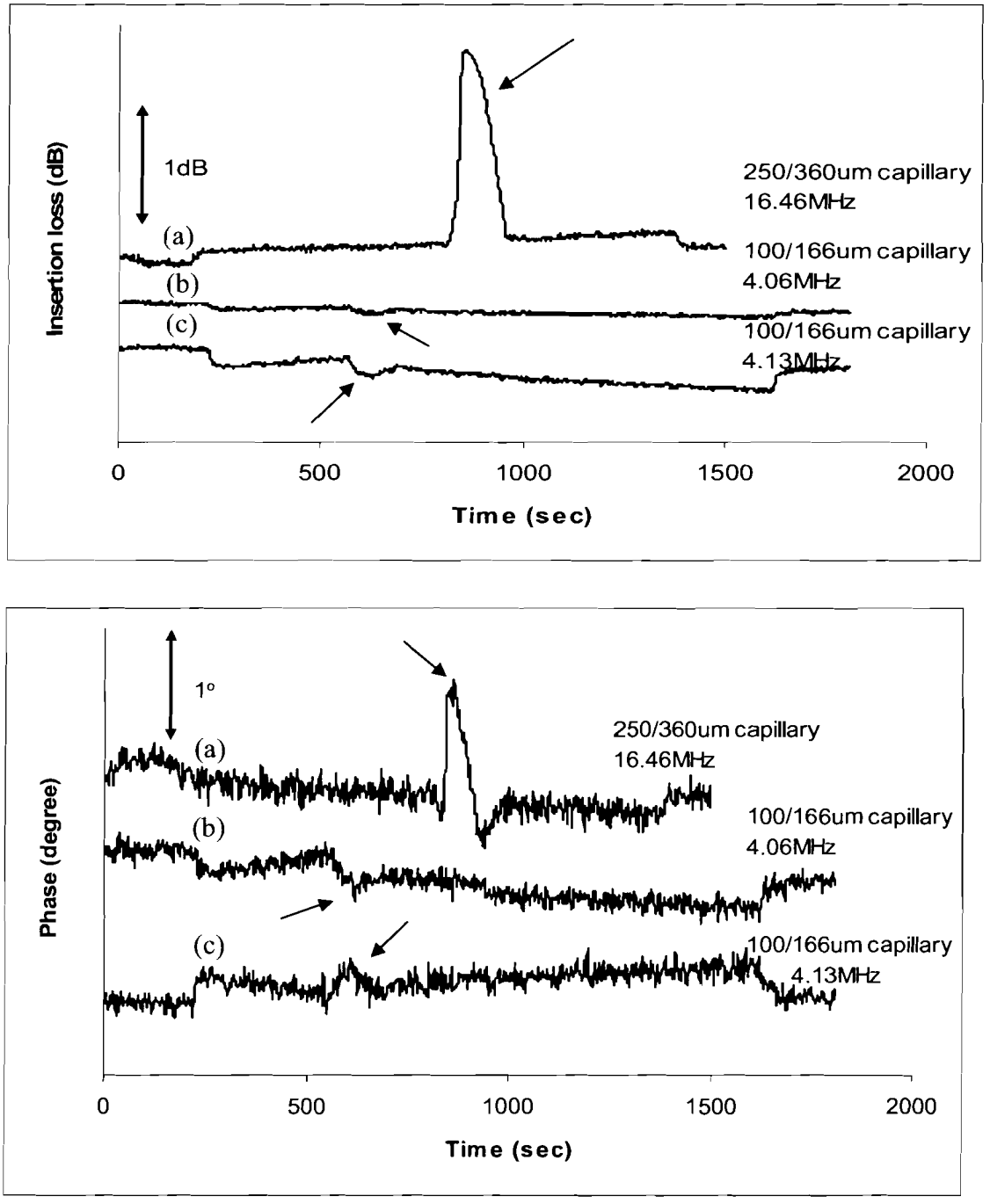

Figure 5.7. Comparison of (top) insertion loss and (bottom) phase profiles of 50mM leucine using the pinducers with different dimension of capillaries. Experimental conditions: capillary, 50.0 cm, (a) id 250 μm, od 360 μm, (b and c) id 100 μm, od 166 μm, distance to detector, 41.1 cm; applied voltage, (a) 3kV, (b and c) 10kV; run buffer, 1 mM sodium carbonate/sodium bicarbonate, sample introduction time, (a) 3s, (b and c) 60s, frequency, (a) 16.46 MHz, (b) 4.06 MHz, (c) 4.13 MHz

5.2 Acoustic wave detection of single underivatized amino acids

5.2.1 Detection of Leucine

A successful detection of 50mM leucine has already been shown in Figure 5.7. In this example, it was found that the use of the 250-μm-id capillary is essential to produce a strong signal in the insertion loss change. This was also the direct result of using the pinducers and a low-concentration buffer.

After optimization of the acoustic wave detection system by using pinducers, low-conductivity buffer and a larger internal diameter capillary, other parameters that would affect the acoustic detection of leucine were studied in detail. These parameters included the buffer concentration, sample concentration, acoustic wave frequency, buffer pH, and capillary geometry.

5.2.2 Effect of buffer concentration

The buffer concentration used in a CE system has a significant effect on acoustic detection. As there is current passing through the run buffer, Joule heat is generated, and the amount of which is proportional to the reciprocal of the solution resistance. The Joule heating led to a localized heat zone in a low-conductivity sample plug compared to the cool zone in the flanking high-conductivity buffer[2]. This has led to a thermal peak in our measurements. In our study, since a much larger internal diameter capillary (250μm) was used compared to a conventional CE capillary (50μm), the current as well as the Joule heat generated would be much larger than in a conventional system. This would have resulted in an undesirable CE separation and the occurrence of the thermal peak.

To avoid such problems, we chose to decrease the concentration of the run buffer from 12.5 mM to 1 mM in order to reduce the Joule heat generation and the elimination of the thermal peak. In this way, the conductivity of the run buffer as well as the generation of Joule heat was reduced. Two insertion loss profiles (water and leucine) are shown in Figure 5.8a. By the use of low-concentration of run buffer, as previously discussed in Section 5.1.2, no thermal peak was observed in the case of water. In the case of 50mM leucine, a peak was obtained. Similar observations were obtained in phase measurements. As shown in figure 5.8b, the phase profile of water had no observable peak; whereas the phase profile of 50mM leucine produced a change of about 1°. Since there was a difference in material properties between the run buffer and the sample injected, as the sample plug passed through the detection zone, the change of the insertion loss and phase angle was detected. Therefore, the presence of leucine was detected in both the phase and insertion loss measurements.

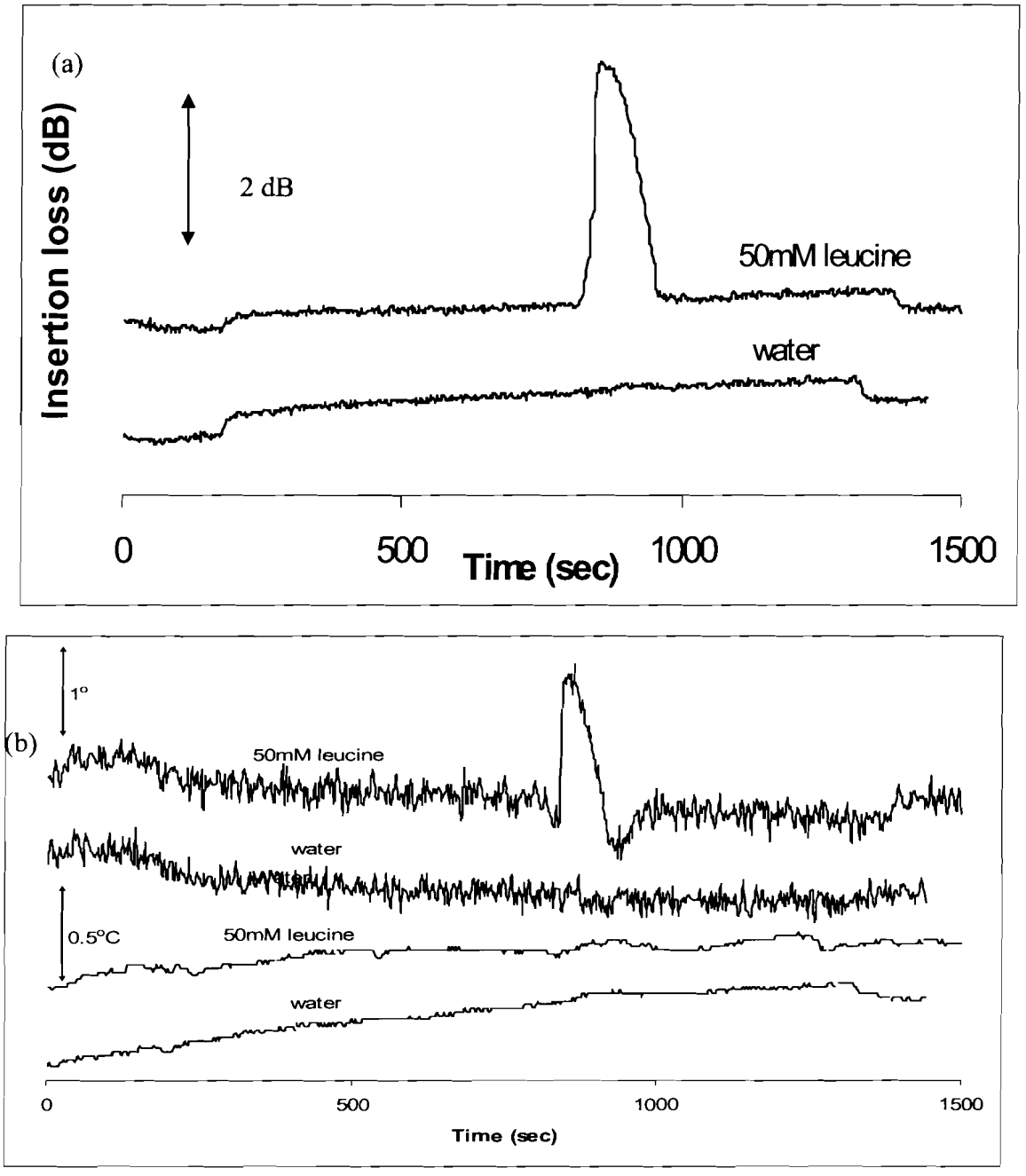

Figure 5.8. Ultrasonic detection of 50mM leucine (prepared in water) with negative control (water) (a) insertion loss (b) phase profile. Experimental conditions: capillary, 50.0 cm, id 250 µm, od 360 µm, distance to detector, 41.1 cm; applied voltage, 3kV; run buffer, 1 mM sodium carbonate/bicarbonate; frequency, 16.46 MHz.

5.2.3 Effect of sample concentration

To establish the success of the acoustic wave detection of leucine, its concentration dependence should be investigated. Various concentrations of leucine in water were introduced to the CE system in order to verify the expected linear relationship between the concentration of leucine and the peak area of insertion loss. The range of concentrations examined was from 5 mM to 50mM. The lower end, which was 5 mM, was selected due to the small magnitude of the signal peak obtained, whereas the upper end, 50 mM, was selected due to the limited solubility of leucine in water. In figure 5.9a, the peak area of the insertion loss signals were plotted against the concentration of leucine. It was found that as the concentration of leucine in water was increased, the insertion loss became greater accordingly. The peak area of insertion loss signals were estimated by multiplying the peak width and the half of the peak height. The error bars were assigned according to the peak-to-peak noise in the baseline. The linearity of the concentration dependence of leucine was very good, as given by an R^2 value of 0.9913. From the calibration curve, the detection limit of leucine was determined to be approximately 3.5mM. Similar concentration dependence was also found in the phase measurements with an R^2 value of 0.9876. When comparing the linearity of the concentration dependency of the experimental data with the theoretical model, the experimental data is not matching the model. The model deviated from linearity beyond 200mM (R^2 =0.9993 by omitting the 500mM point). The deviation is due to the τ term in the absorption which is inversely proportional to the concentration of the amino acid. The linearity observed from the experiments may be due to other factors, such as density of the sample. In addition, figure 5.9a showed retention time shifted in 50 mM and 5 mM leucine which could be due to the variation of EOF.

Figure 5.9b shows that there was no significant change in temperature (<0.1 ^{o}C) when leucine (of different concentrations) arrived at the detection zone. This again confirms that the thermal effect has been eliminated by the use of a low-concentration buffer. So it appears that the changes in insertion loss and phase are caused by non-thermal factors. On the other hand, it should be noted that the acoustic wave speed in water varies with temperature, and this would influence the standing wave pattern, leading to the variations in the insertion loss and phase measurements. According to Table 1, the sound speed in water is 1498 m s-1; as shown in reference 39, this value increases by 4 m/s for every degree C that the temperature is increased. In other words, the relative change in sound speed is of order 0.27%/deg C. Alternately, the phase of a wave propagating across the cell will change by 0.27%/deg C. Therefore, at frequencies of order 16 MHz, a 1 degree temperature change will result in standing wave patterns being shifted by frequencies of order 40 kHz. With reference to Fig. 5.10, shifting the buffer curve horizontally by ~20 kHz is sufficient to account for the observed changed in IL. This may indicate that the observed change in IL is yet - at least in part - a result of the thermal effect shown in Fig. 5.9.

The insertion loss change of 50mM leucine was measured to be 2.2dB (see Figure 5.8a). This value is much greater than the theoretical value predicted by equation (66), indicating the inadequacy of the theoretical model which does not account for thermal effect. Therefore, it is concluded that further investigation is needed to resolve the discrepancy and to identify any significant systematic biases.

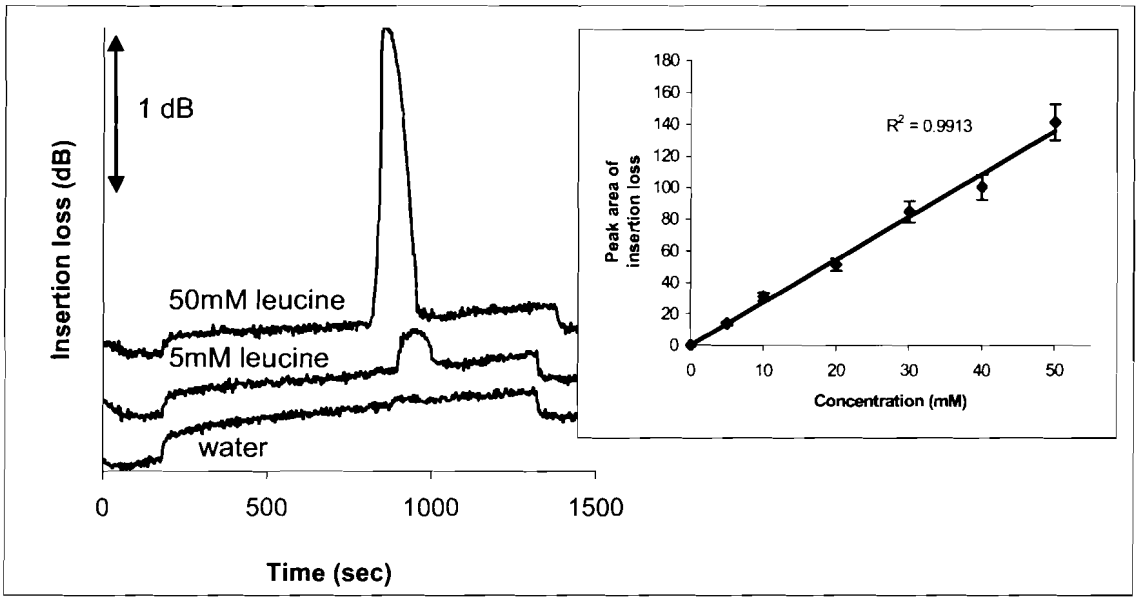

Figure 5.9a. Electropherograms (in insertion loss) of 50mM leucine, 5mM leucine (prepared in water) and water alone using the pinducers. (Inset) Insertion loss peak area vs. various concentrations of leucine (0 – 50 mM). Experimental conditions: capillary, 50.0 cm, id 250 μm, od 360 μm, distance to detector, 41.1 cm; applied voltage, 3kV; run buffer, 1 mM sodium carbonate/sodium bicarbonate, sample introduction time, 5 s, frequency, 16.46 MHz.

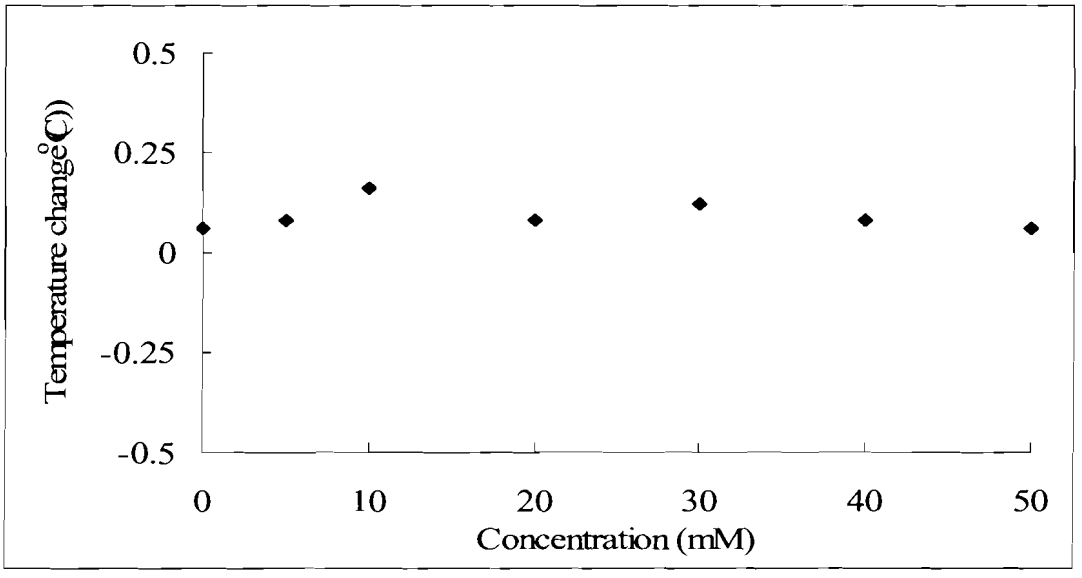

Figure 5.9b. Temperature change vs concentration of leucine during experiment using the pinducers with the same experimental conditions as Figure 5.9a.

5.2.4 Effect of acoustic wave frequency

The acoustic wave frequency had a significant effect in the detection in terms of insertion loss and phase measurements. It is informative to examine the effect of the acoustic wave frequency on the measured signals. Although the equipment allows us to collect the insertion loss and phase data at 401 different frequencies in a single experiment, our spreadsheet program can only handle 255 columns. Since this information is already quite substantial, no attempt was made to employ a more sophisticated spreadsheet program. Therefore, data at 255 frequencies were collected for each experiment. Figure 5.10 shows the plot of insertion loss against frequency of a leucine (50 mM) experiment. As shown in Figure 5.10, the two overlapping dotted-line curves represent the insertion loss of the run buffer before and after the sample arrival at the detection zone; whereas the solid curve represents the insertion loss curve of the sample that arrived at the detection zone. The times at which these curves were collected correspond to the migration times of approximately 800, 950 and 1100 s in Figure 5.10b. At some particular frequencies, say 16.46MHz, the insertion loss of the sample is greater than that of the buffer (see the left arrow in Figure 5.10a), resulting in a positive peak in Figure 5.10b. Owing to the crossover, at other frequencies, such as 16.69MHz (see the right arrow in Figure 5.10a), the insertion loss-time curve should result in a negative peak. This negative peak is associated with the temperature difference between the sample and the buffer which leading to a modification of wave pattern. Therefore, the difference in the insertion loss of the sample and the buffer depends on the frequency, which can be manifested as a positive or negative peak. In addition, the magnitude of the insertion loss difference, resulting in a different peak height, also depends on the frequency. The selection of 16.46 MHz, in Figure 5.10, has resulted in the maximal height of the leucine peak in this particular experiment.

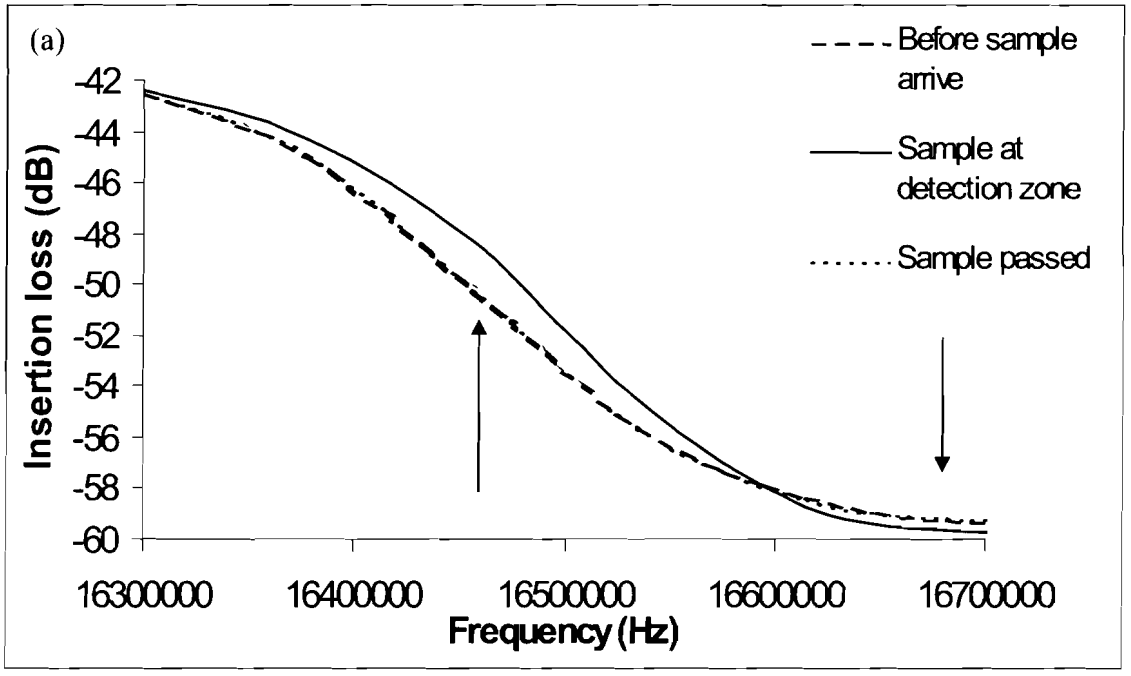

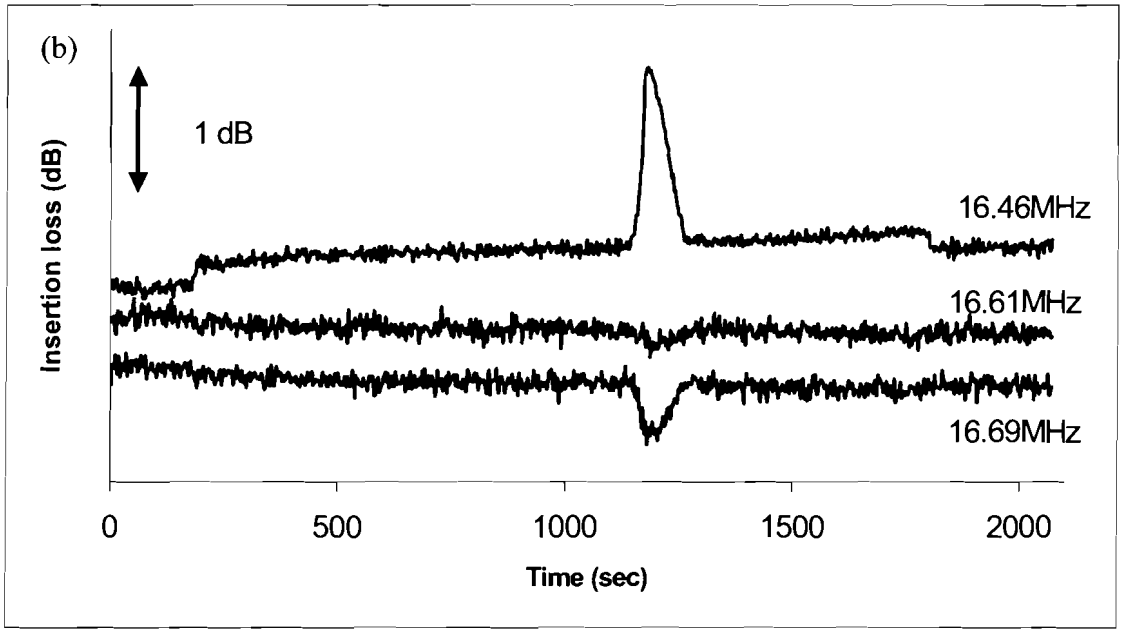

Figure 5.10. (a) Plot of insertion loss vs. frequency for the ultrasonic absorption of 50 mM leucine. (b) Electropherograms (insertion loss at 16.46 MHz, 16.61 MHz and 16.69 MHz) of the same experiment run as in (a). Experimental conditions: capillary, 50.0 cm, id 250 μm, od 360 μm, distance to detector, 41.1 cm; applied voltage, 3kV; run buffer, 1 mM sodium carbonate/sodium bicarbonate, pH = 9.0.

5.2.5 Effect of pH

As given in equation (15) in section 2.3, it is known that the ultrasonic absorption of amino acids is dependent on pH because the perturbation of the proton-transfer equilibrium of amino acids is the principal process causing the attenuation of the acoustic wave.

In our study, static acoustic wave measurements were also performed in which a high voltage was not applied to the capillary. This measurement indicated how the pH affected the ultrasonic absorption of the analyte in a static manner. The analyte was dissolved in the buffer and used to fill up the whole capillary for measurements. At the detection zone, the liquid content inside the capillary was static. The pH dependence of amino acids was performed with two amino acids, glutamic acid and aspartic acid. The ultrasonic coefficient of these two amino acids was studied in the pH range of 11.1 to 12.3. A parameter of frequency-normalized ultrasonic absorption coefficient (α/f^2) is defined by dividing the ultrasonic absorption coefficient (α) by the square of the acoustic wave frequency (f). The parameter α/f^2 is plotted against pH, as shown in Figure 5.11a and Figure 5.11b for glutamic acid and aspartic acid, respectively. It is estimated that the pH at which the maximum value of α/f^2 of glutamic acid occurred is 11.8. Similarly, the value for aspartic acid is estimated to be 11.5. These values were consistent with the values previously reported (11.73 and 11.55, respectively).[29]

Moreover, the maximum α/f^2 value of glutamic acid (at 5.51 MHz) is 215×10^{-14} dB sec^2 m^{-1}. By converting the unit of dB to Neper, this value becomes 247×10^{-15} Neper sec^2 m^{-1}, which has a similar order of magnitude to the literature value of 130×10^{-15} Neper sec^2 m^{-1} (5.21 MHz)[26,29]. Since the data point at 5.21 MHz was not obtained in my experiment, a close frequency (5.28 MHz) was chosen to compare with the literature value. The α/f^2 value obtained in 5.28MHz was 135×10^{-15} Neper sec^2 m^{-1}, which was closer to the literature value than the value

at 5.51 MHz did. A similar experiment was performed for aspartic acid. The maximum α/f^2 value of aspartic acid (at 5.51 MHz) is 200×10^{-14} dB sec^2 m^{-1}.

A similar experiment was performed for a leucine sample with a testing range from pH 2 – 12. The insertion loss versus pH was plotted in figure 5.12. The experiment was done at a high-response frequency, 16.46 MHz. The insertion loss values obtained in the plot were subtracted from the values obtained in the blank solution. From the plot, the highest difference of the insertion loss of leucine from the blank solution occurred around pH 3.5. Although the highest difference was found at pH 3.5, this pH was not easily employed in the CE system since EOF is very slow at low pH. This pH is also very close to the surface pka which may introduce a deprotonation of the surface problem. Furthermore, the low pH buffer was not obtained unless hydrochloric acid was added. The addition of hydrochloric acid would generate a huge current in the CE system, and thus resulting in interference in the acoustic measurements. These also worsened the thermal effect, and thus a thermal peak occurred. Hence, this pH was not used in the experiments. In contrast, the pH used in the experiment of leucine was 9.0. From Figure 5.12, this pH provided a modest, but not low, insertion loss response.

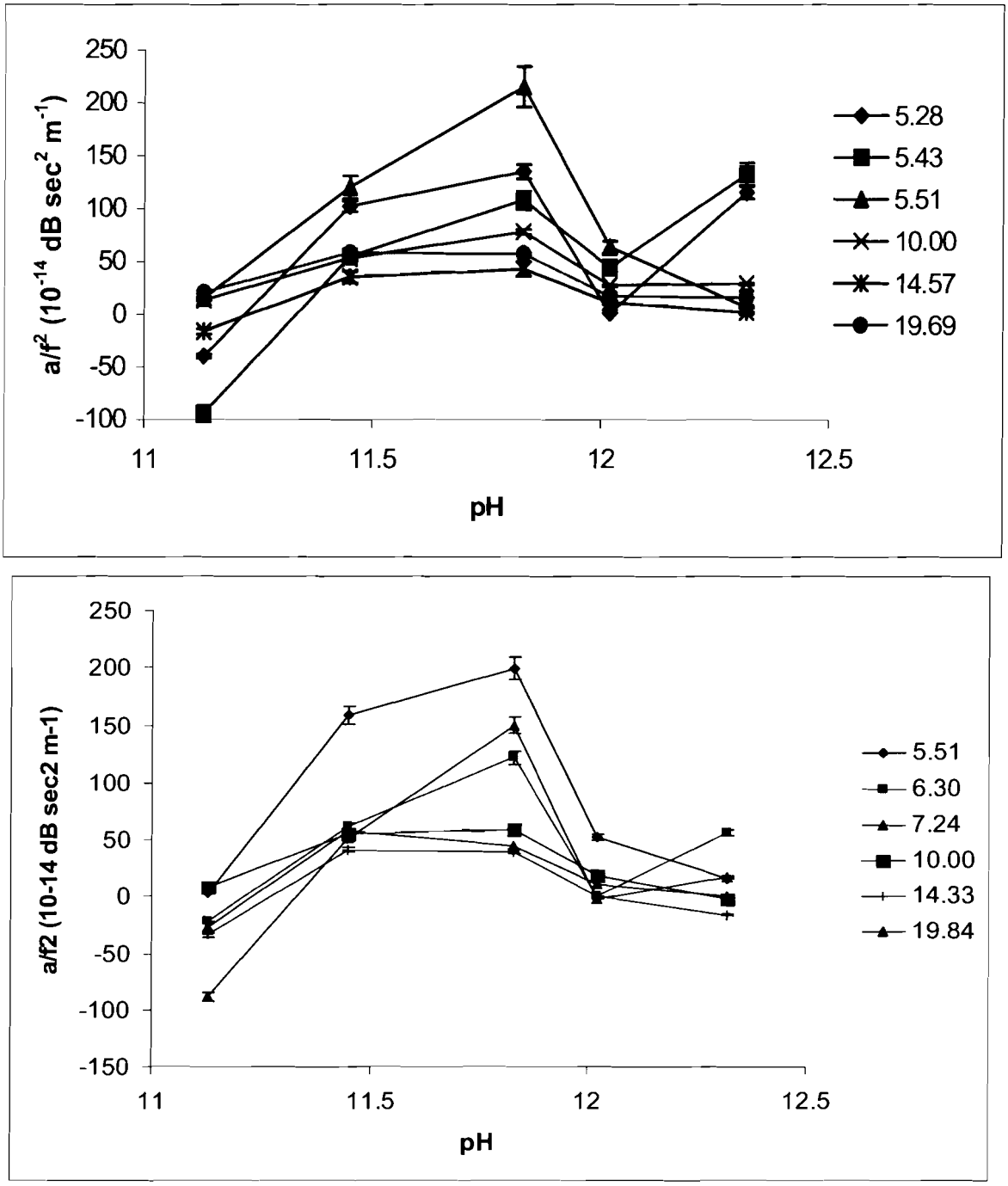

Figure 5.11. Ultrasonic absorption (expressed as α/f^2) of (a) glutamic acid (b) aspartic acid at various pH. Experimental conditions: capillary, 50.0 cm, id 250 µm, od 360 µm, distance to detector, 41.1 cm; capillary filled up by buffer and then replaced by sample ((a) 20 mM glutamic acid, (b) 20 mM aspartic acid. The legend represents the pinducer frequency in MHz. The lines are used to join data points for clarity.

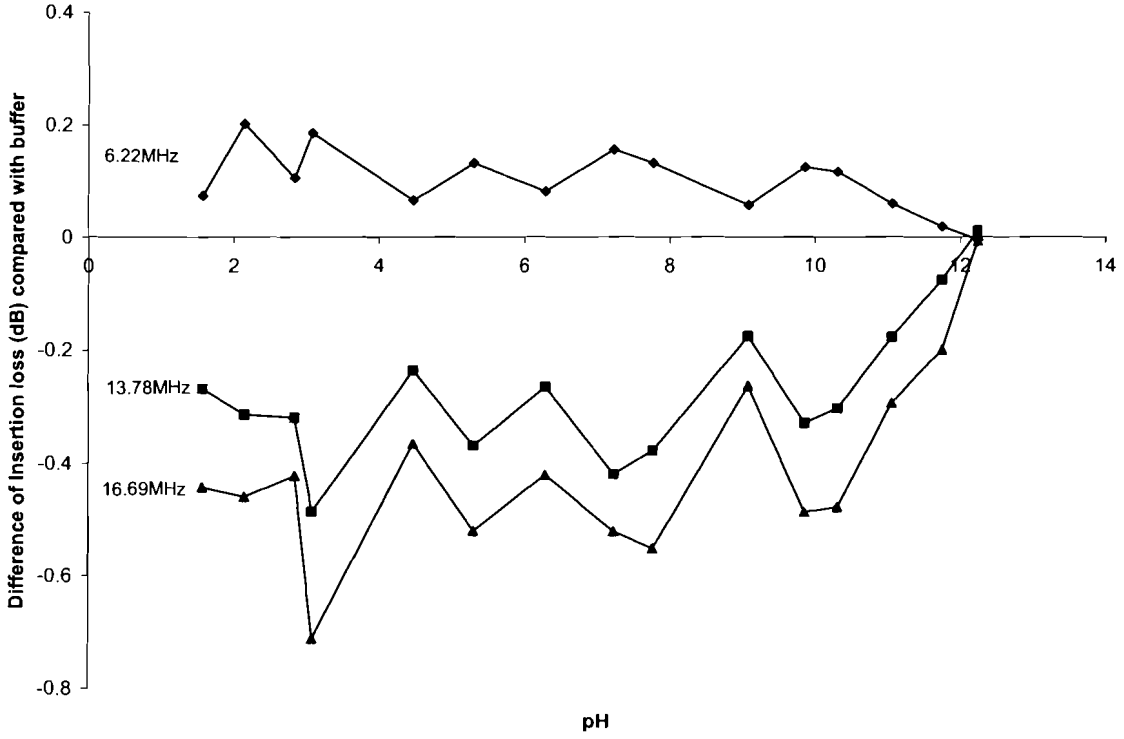

Figure 5.12. Differences in insertion loss between 20 mM leucine and buffer. Experimental conditions: capillary, 50.0 cm, id 250 µm, od 360 µm, distance to detector, 41.1 cm; capillary filled up by buffer and then replaced by leucine. Lines are used to join data points for clarity.

5.2.6 Effect of capillary geometry

The coupling between the pinducers and the outer wall of the capillary had a significant effect on the acoustic wave measurements. The geometry and dimension of the capillary were important concerns in the experimental setup. Two kinds of capillary geometry, square and circular, were used, as shown in figure 5.13. The circular polyimide coating in the square capillary was removed.

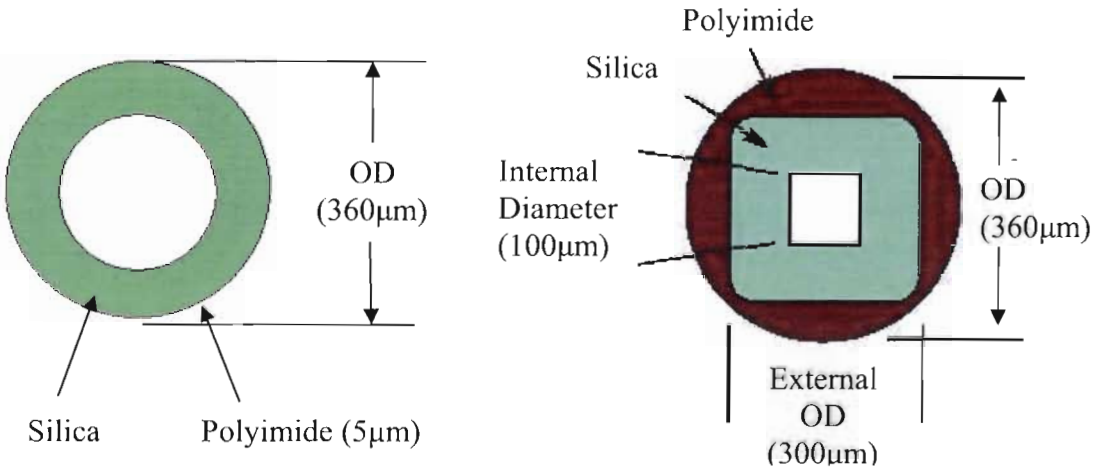

Figure 5.13. Cross-section diagrams of circular (left) and square (right) capillaries (OD: outer diameter; ID: internal diameter)

An acoustic wave propagates from the generating transducer to the outer wall of the capillary, and then travels though the liquid inside the capillary back to the receiving transducer. The propagation loss of the acoustic wave was due to the attenuation of the wave between the two transducers when the wave propagates. The coupling between the transducers and the outer wall of the capillary had an important effect on wave propagation. Since the wave propagation velocities in solid and air are very different, it might create changes in the insertion loss and phase

angle. To reduce this wave propagation problem, the polyimide coatings were removed. Since the pinducer's surface was flat, the best contacting surface would be a plane surface. The coupling of the pinducers with the circular capillary was not perfect. This was due to the curvature of the circular capillary (see Figure 5.14). It could have some trapped air in between the pinducers' surfaces and the outer wall of the circular capillary, therefore, the wave propagation might have been weakened by poor coupling. Any trapped air would create an interface, causing wave reflections. But there is a better contact between the pinducer and the outer wall surface of the square capillary. Therefore, the coupling between the pinducers and the square capillary was expected to be better than that of circular capillary.

The comparison of the performance of these two types of capillary was made using 20 mM leucine as the sample. In figure 5.15, three traces of insertion loss with the use of different capillaries are shown. The experiments were performed at frequencies (14.57MHz and 13.46MHz for square and circular capillaries, respectively) which gave the largest change of insertion loss. A larger insertion loss peak was obtained in the square capillary. Furthermore, the signal to noise ratio was better in the case of using a square capillary. These provided evidence for the assumption that the contact surface was very important for the acoustic wave measurements. Since the contact area for a square capillary is better than that of a circular capillary, the wave transmission was found to be better in a square capillary.

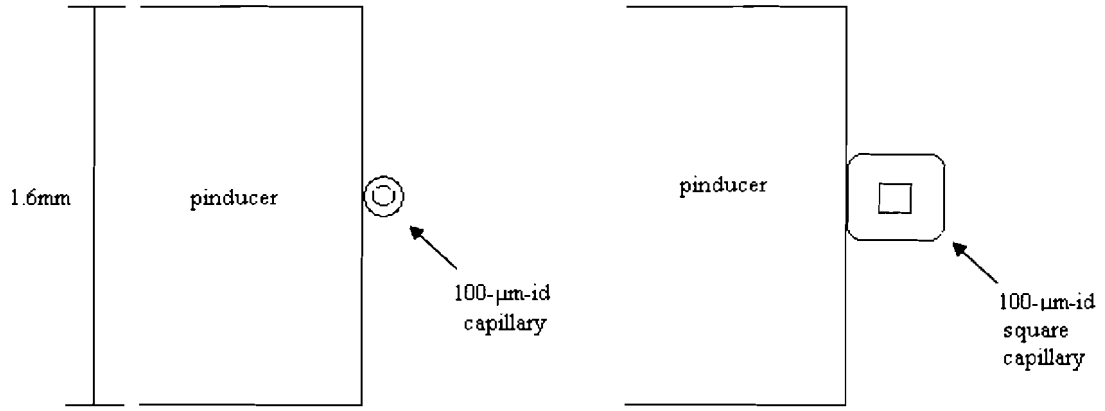

Figure 5.14. Coupling between the pinducer and (left) the 100-µm-id circular capillary, (right) the 100-µm x 100-µm square capillary

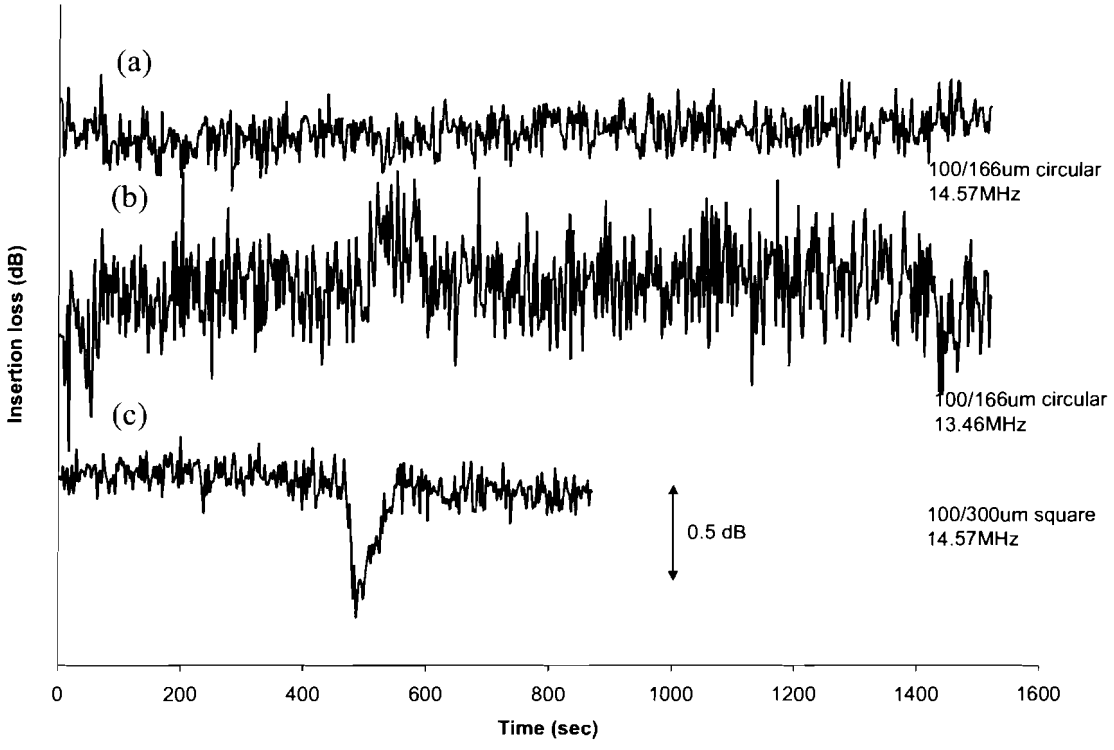

Figure 5.15. Electropherograms (in insertion loss) of 20mM leucine (prepared in water) in different geometry and internal diameters of capillaries. Experimental conditions: (a and b) id 100 µm, od 166 µm circular, (c) id 100 µm, od 300 µm square. Other conditions: capillary length, 50.0 cm, distance to detector, 41.1 cm; applied voltage, 5kV; run buffer, 1mM sodium carbonate/bicarbonate; frequency, (a and c) 14.57 MHz, (b) 13.46MHz; injection time, 60s.

5.3 CE separation of amino acids detected acoustically

Capillary electrophoresis was performed for the separation of amino acids. Different amino acids, histidine, leucine, tryptophan and proline, were used for separation. The separation performed in CE was based on the difference in the charge-to-size ratios of the analytes. The charge of the analyte was determined by the difference between the pI value and the buffer pH. The pI value is the pH at the isoelectronic point, i.e. the pH at which the analyte has the same degree of protonation at the NH_2 end as the deprotonation at the COOH end. If the buffer pH was larger than the pI value of the analyte, the analyte would have more deprotonation at the COOH end rather then protonation at the NH_2 end, and becomes negatively charged. In the case of leucine and tryptophan, their pI values are close (see Table 2), and this poses a challenge for their separation. Due to their similar pI, the degrees of deprotonation of the two amino acids were very close. These two amino acids cannot be separated with conventional buffer conditions. Therefore, surfactants were employed to improve their separation. Three different surfactants, SDS, Brij 35 and Triton X-100, were used to enhance the separation. Other experimental parameters, such as capillary geometry, separation voltage, and buffer composition were also examined.

5.3.1 Identification of amino acids

Leucine and histidine were separated in the 10mM HEPES buffer system. The electropherograms are shown in Figure 5.16. The top trace shows the separation of 20mM leucine and 10mM histidine. Histidine was eluted first, followed by leucine. Individual histidine and leucine samples were injected for identification of the analytes. The insertion loss changes were different in sign for histidine and leucine. The response of histidine was negative; whereas that of leucine was a positive change. The individual injection of leucine showed a smaller peak than that of

the mixture because the injection time was one second which could have a large variation, and hence the injected amount could be different in every injection.

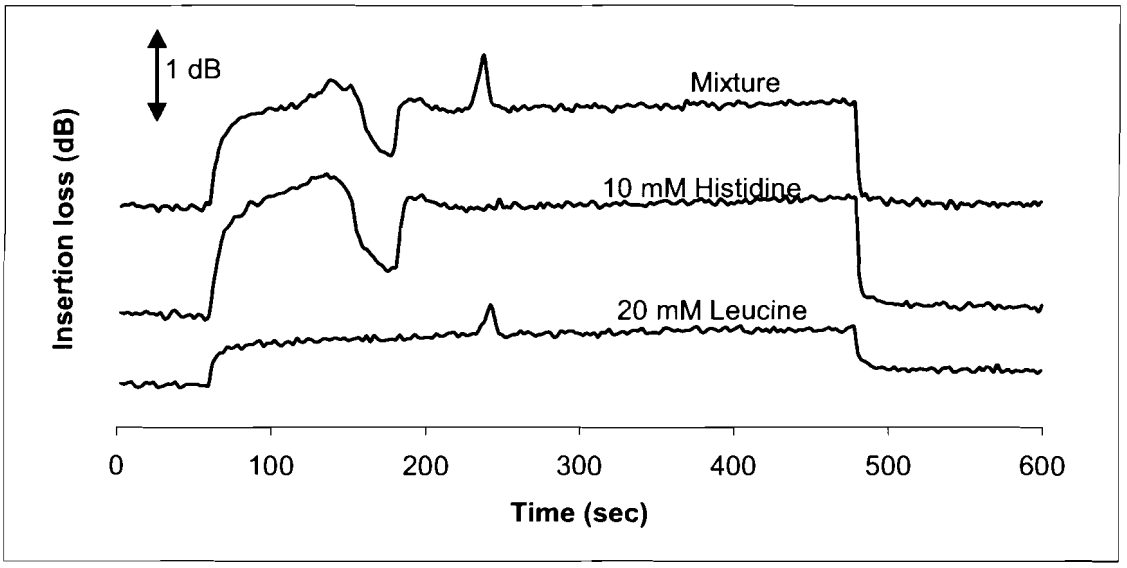

Figure 5.16. Electropherograms (in insertion loss) of a mixture of leucine (20 mM) and histidine (10 mM), and their individual components (all prepared in the run buffer). Experimental condition: capillary, 50.0 cm, id 250 μm, od 360 μm, distance to detector, 41.1 cm; applied voltage, 30 kV; run buffer, 10 mM HEPES; pH 7; frequency, 16.46 MHz; injection time, 1 s.

While the separation of histidine and leucine was straightforward, the separation of leucine and tryptophan was a challenge because their pI's are close (5.98 and 5.89 for leucine and tryptophan, respectively). With the addition of surfactants, the separation of leucine and tryptophan was accomplished. SDS was chosen to be the first surfactant tested as it is widely used in CE separations. The separation would be achieved as the concentration of the surfactant was above its CMC. In the case of SDS, the CMC was 8mM, or ~0.2% w/w.[9] The SDS micelles interacted with the chemical species in the sample forming micelle-analyte complexes, see Figure 1.1. This would alter the migration time of the analytes. Figure 5.17 shows the separation of 20mM leucine and 20mM tryptophan. In Figure 5.17a, as no SDS was added to the run buffer, there was no separation and only one peak was obtained. As 0.5% of SDS was added to the run buffer, two separated peaks were obtained (see Figure 5.17b). When the voltage was reduced, the migration

became slower, and the separation was enhanced (see Figure 5.17c). Further enhancement was obtained by reducing the sample injection time, and the injected amount (see Figure 5.17d). Spiking of the sample with an additional amount of one of the analytes (e.g. leucine) was used to identify the two peaks.

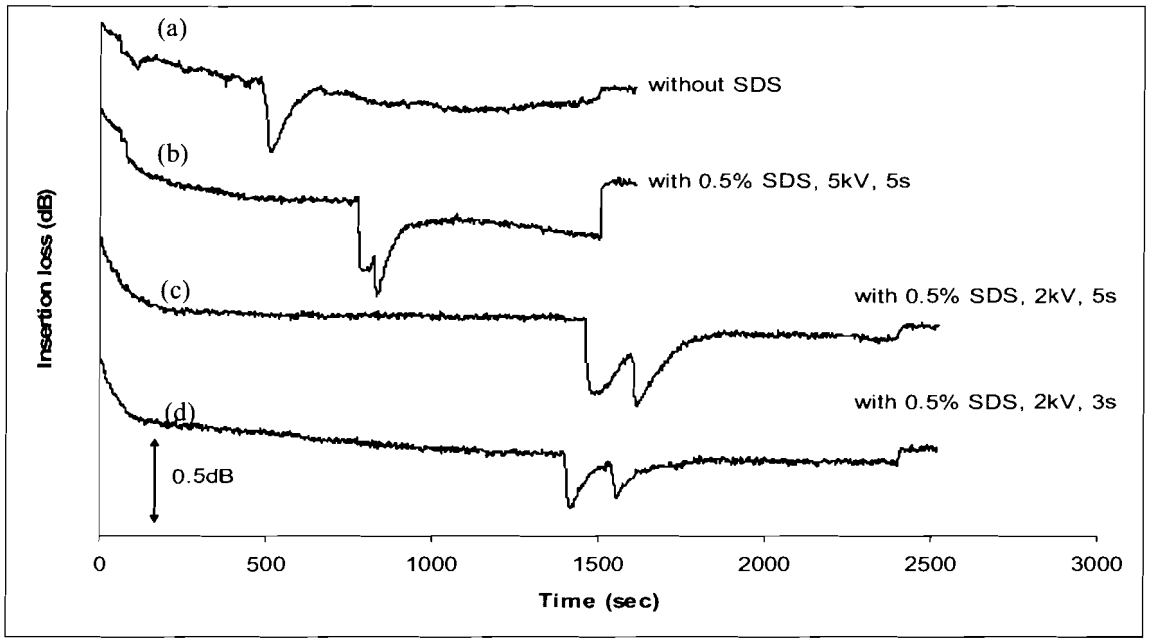

Figure 5.17. The use of SDS and various voltages and injection time for separation enhancement of a mixture of 20 mM leucine and 20 mM tryptophan. Experimental conditions: capillary, 50.0 cm, id 250 µm, od 360 µm circular, distance to detector, 41.1 cm; applied voltage, 5 kV/ 2kV; run buffer, 1mM sodium carbonate/bicarbonate (a) without SDS, (b, c and d) with 0.5% SDS ; frequency, 13.8MHz; injection time, (a, b and c) 5 s, (d) 3 s.

In the electropherogram shown in figure 5.18, by increasing the concentration of leucine from 40mM to 50mM, the first peak from the trace was increased in size. This indicates that the first peak is due to leucine, whereas the second peak is due to tryptophan. The migration times for the two traces were different because the EOF generated might not be the same since the samples injected into the capillary were of different conductivity.

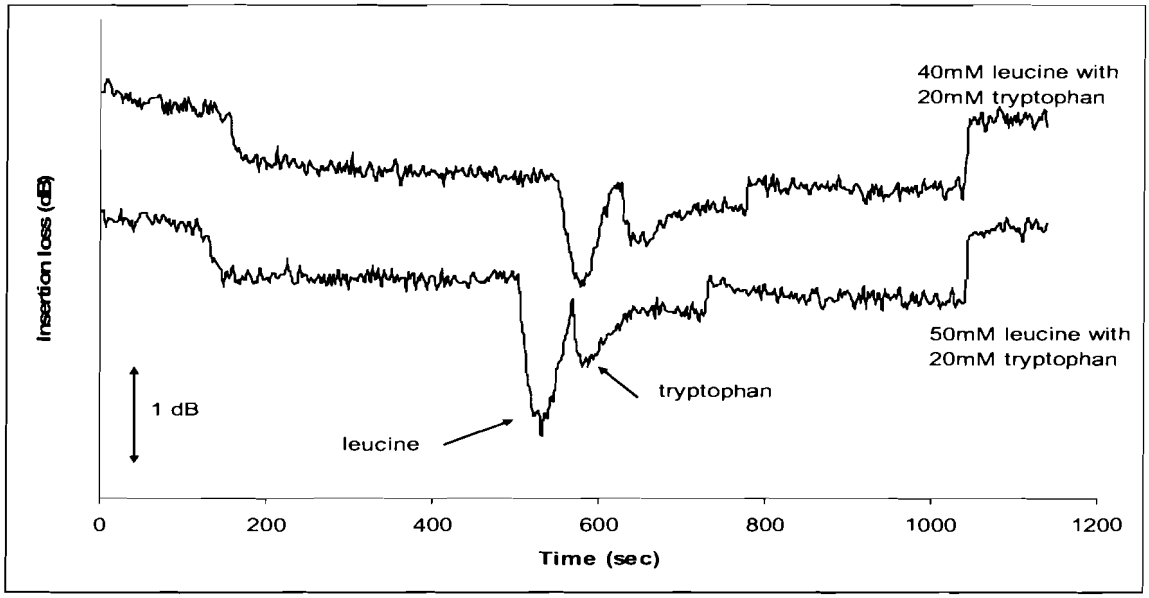

Figure 5.18. Identification of the sample mixture of leucine and tryptophan by spiking leucine. Experimental conditions: capillary, 50.0 cm, id 250 μm, od 360 μm circular, distance to detector, 41.1 cm; applied voltage, 5 kV; run buffer, 1mM sodium carbonate/bicarbonate + 0.5% SDS; frequency, 13.8 MHz; injection time, 5 s.

More variations of the concentrations of analytes were performed to verify the linear relationship between the concentrations of analytes and the peak size. Figure 5.19 shows the calibration curve of the leucine/tryptophan insertion loss peak area ratio versus the leucine/tryptophan concentration ratio at two frequencies. As the ratio of leucine/tryptophan concentration increased, the corresponding ratio of the peak area increased linearly. The R^2 values were found to be 0.9908 and 0.9924 for 13.8 MHz and 16.69 MHz, respectively.

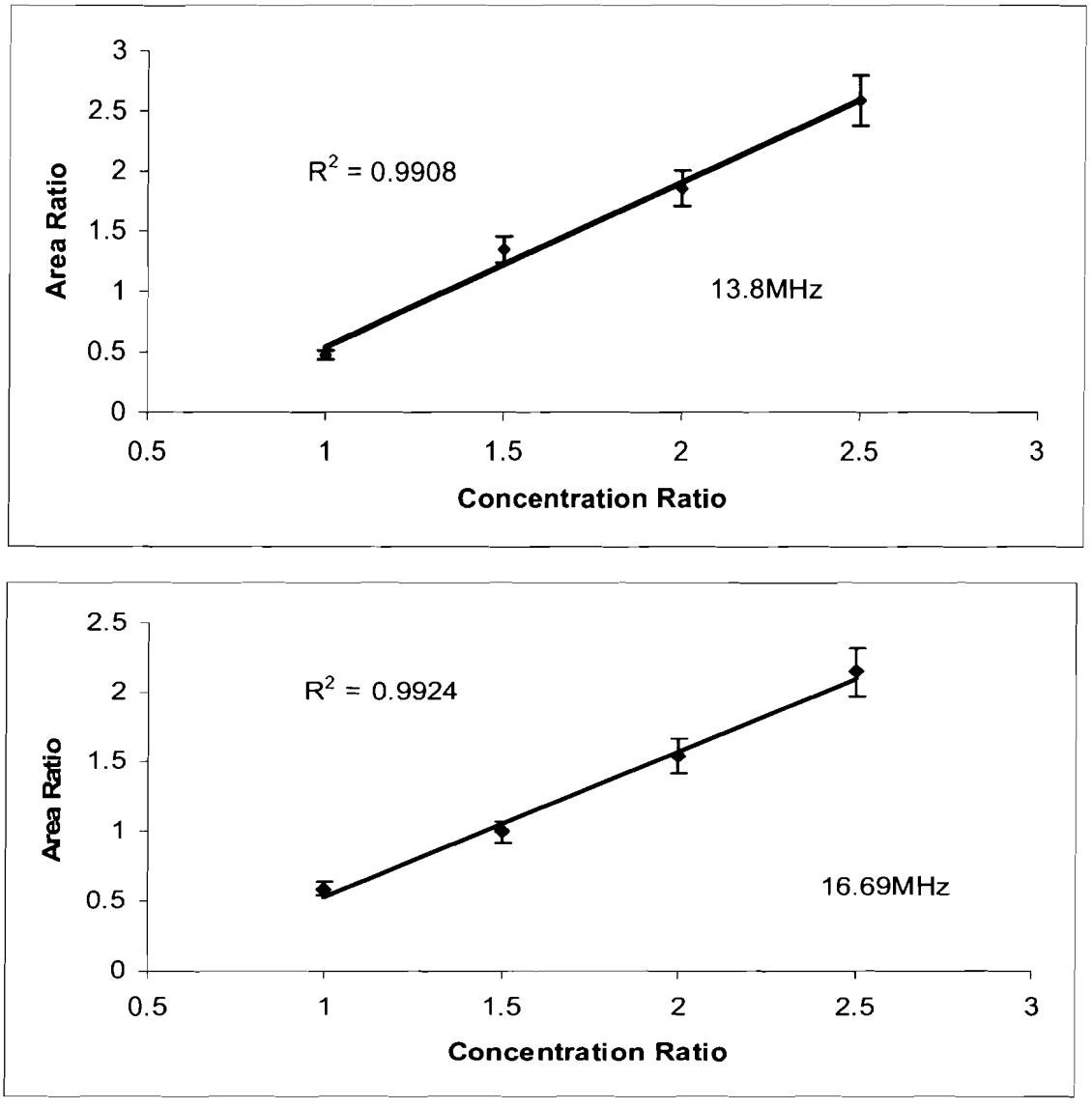

Figure 5.19. Calibration curve of various concentration ratios of leucine to 20mM tryptophan. Experimental conditions: capillary, 50.0 cm, id 250 µm, od 360 µm circular, distance to detector, 41.1 cm; applied voltage, 5kV; run buffer, 1mM sodium carbonate/bicarbonate + 0.5% SDS; frequency, (upper) 13.8 MHz, (lower) 16.69 MHz; injection time, 5s.

Separation between leucine and proline was not achieved with 0.5% SDS (see Figure 5.20a). By increasing the SDS concentration to 1% and increasing the applied voltage from 2 kV to 5 kV, leucine and proline are barely separated, as shown in figure 5.20b. The first peak is verified to be proline by spiking, see the subsequent paragraph. Figure 5.20c shows a control of the injection of water, indicating the absence of the thermal peak (see section 5.12).

The separation of three amino acids, leucine, tryptophan and proline, was also attempted (see Figure 5.21). Using the spiking technique, the elution order was determined to be proline, followed by leucine and then by tryptophan. For instance, the mixture of proline (20mM) and tryptophan (20mM) was spiked with an increasing amount of leucine (5-20 mM), indicating leucine was the second peak, see the arrows in Figure 5.21a. In this spiking experiment, the 20-mM proline peak was reproducible, since the relative standard deviation (RSD) of the peak area was found to be 4% (see Table 3 top). Thereafter, we examined how the peak area ratios of leucine, which were calculated by dividing the peak area of leucine by that of proline, varied with their concentration ratios. As shown in Figure 5.22, the linearity of the peak area ratio versus the concentration ratio of leucine was established, as given by the R^2 value of 0.9936.

In addition, the mixture was spiked with various concentrations of proline (20-50 mM), indicating it represented the first peak (see Figure 5.21b). When the concentrations of proline were low, leucine and proline could be baseline separated. This was due to the reduction of the peak width of proline, which freed the proline peak from being merged with the leucine peak.

In all cases, the peak shape of tryptophan is not symmetric. In fact it is more like a step rather than a peak. The use of 1% SDS (instead of 0.5%) for leucine/proline/tryptophan separation could have worsened the tryptophan peak shape, showing a strong tailing effect. This tailing effect could be due to the longer retention time of tryptophan when inside the micelles.

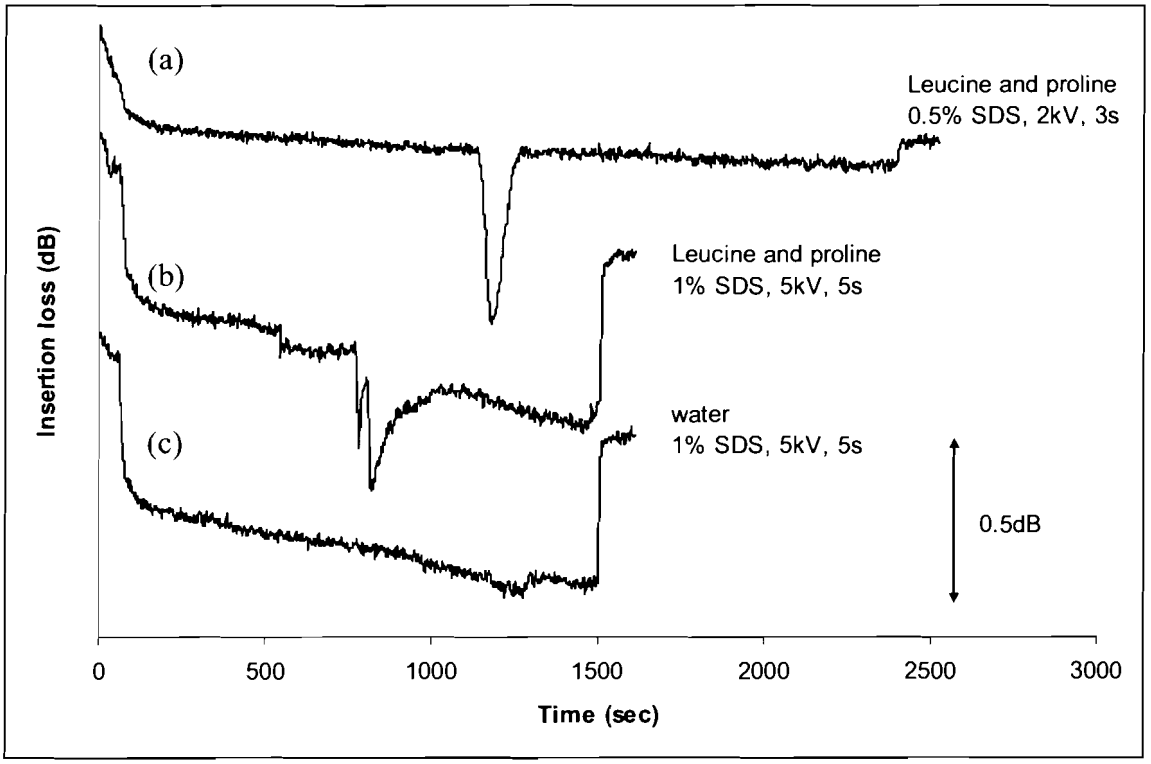

Figure 5.20. The use of higher SDS concentration for separation enhancement between leucine and Proline. Electropherograms (in insertion loss) of mixture sample of 20 mM leucine and 20 mM proline (prepared in water) and water. Experimental conditions: capillary, 50.0 cm, id 250 μm, od 360 μm circular, distance to detector, 41.1 cm; applied voltage, (a) 2kV, (b and c) 5kV; run buffer, 1mM sodium carbonate/bicarbonate (a) + 0.5% SDS, (b and c) + 1% SDS; frequency, 13.8 MHz; injection time, (a) 3 s, (b and c) 5 s.

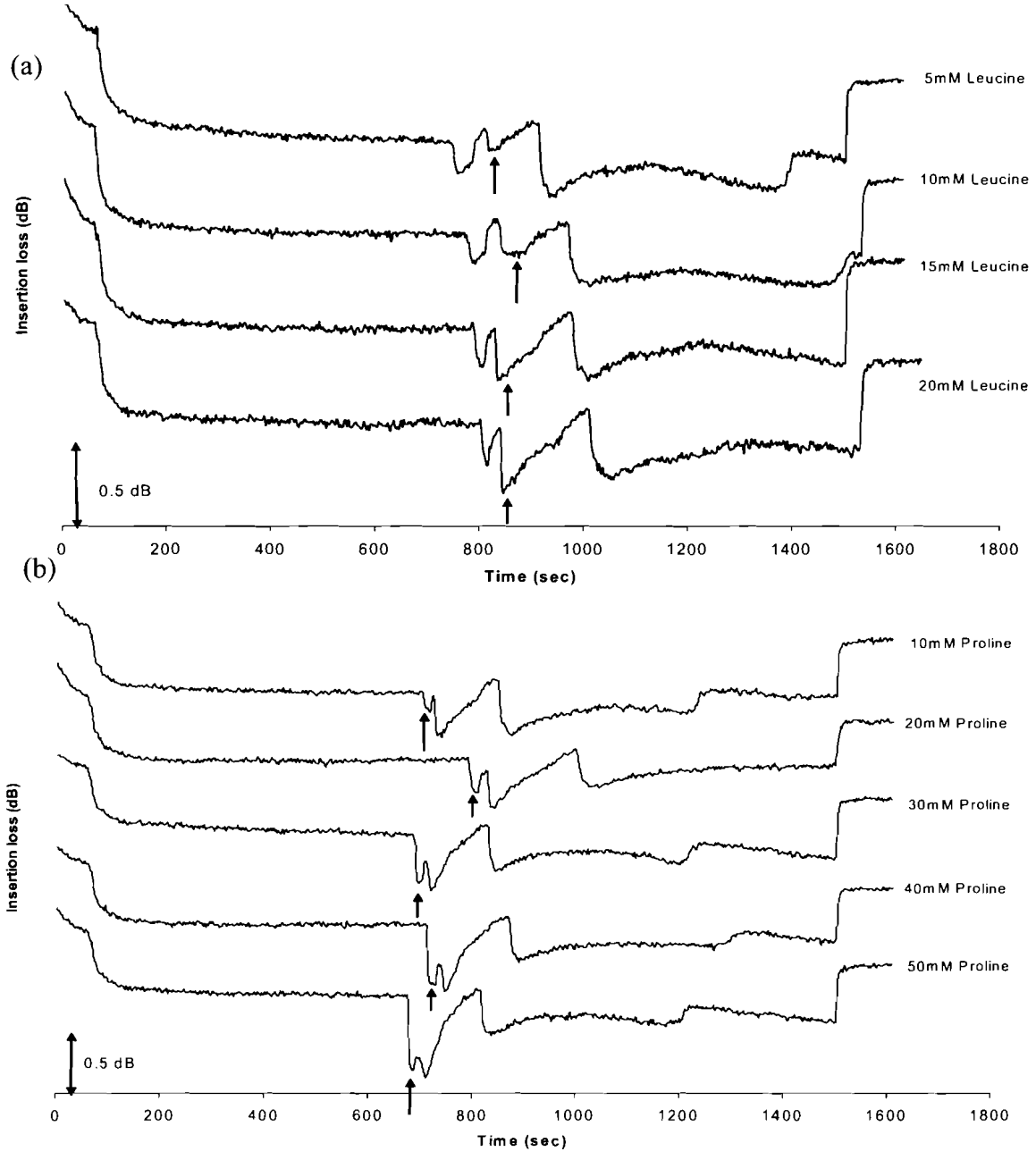

Figure 5.21. Electropherograms (in insertion loss) of mixture of (a) various concentration of leucine (5-20 mM) and 20 mM tryptophan and 20mM proline, (b) various concentration of proline (10-50 mM) and 20mM leucine and 20 mM tryptophan (prepared in water). Experimental conditions: capillary, 50.0 cm, id 250 μm, od 360 μm circular, distance to detector, 41.1 cm; applied voltage, 5kV; run buffer, 1mM sodium carbonate/bicarbonate + 1% SDS; frequency, 13.8 MHz; injection time, 5 s. Arrows pointing the various analytes.

Table 3. (Top) Summary of acoustic wave detection (in insertion loss) of 20 mM proline with various concentrations of leucine (5-20mM). (Bottom) Insertion loss data of various concentration of leucine (5-20mM) with 20 mM proline and tryptophan. Experimental conditions: capillary, 50.0 cm, id 250 μm, od 360 μm, distance to detector, 41.1 cm; run buffer, 1 mM sodium carbonate/bicarbonate + 1% SDS, frequency, 13.8 MHz.

	Peak width proline (sec)	Peak height proline (dB)	Peak area (dB*sec)
	68.82	0.16	10.67
	59.64	0.17	10.02
	42.79	0.24	10.23
	37.13	0.26	9.69
Average	52.10	0.21	10.15
RSD	28.19%	25.35%	4.03%

Concentration (mM)	Peak width leucine (sec)	Peak height leucine (dB)	Peak area (dB*sec)	Concentration Ratio	Area Ratio
5	83.37	0.09	7.50	0.25	0.70
10	92.66	0.16	15.10	0.50	1.51
15	102.22	0.27	27.91	0.75	2.73
20	98.75	0.35	34.76	1.00	3.59

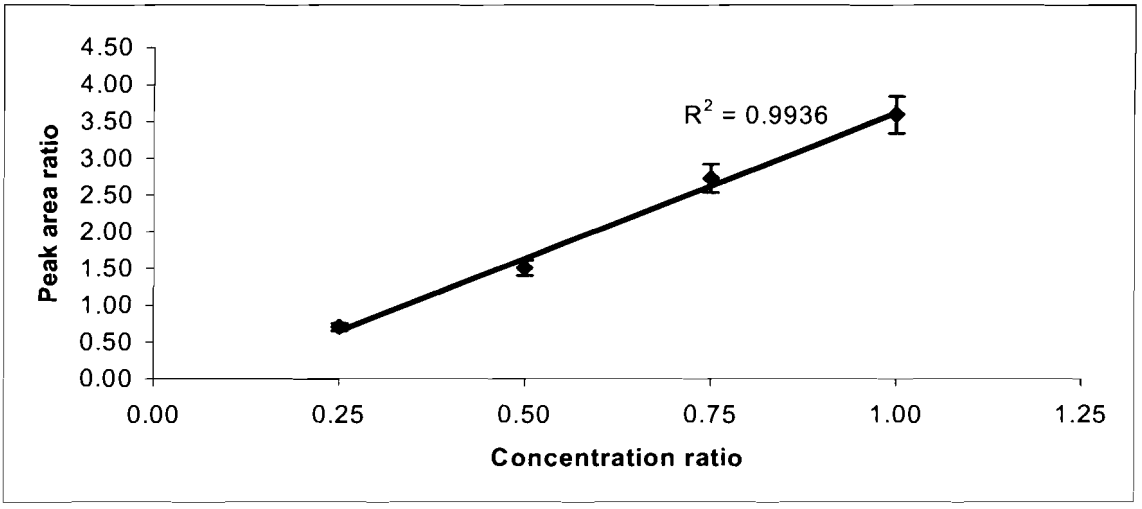

Figure 5.22. Calibration curve of various concentration ratios of leucine with 20 mM tryptophan and 20 mM proline. Experimental conditions: capillary, 50.0 cm, id 250 μm, od 360 μm circular, distance to detector, 41.1 cm; applied voltage, 5 kV; run buffer, 1 mM sodium carbonate/bicarbonate + 0.5% SDS; frequency, 13.8 MHz; injection time, 5 s.

5.3.2 Effect of capillary geometry

As discussed in section 5.2.6, the capillary geometry was significant to the wave propagation for the detection of leucine. The effect was also examined for the CE separation of two analytes, leucine and tryptophan. It was found that there were no signals detected from the circular capillary with a small internal diameter (Figure 5.23b), as it was compared with the square capillary at the same frequency of 14.57MHz (Figure 5.23c).

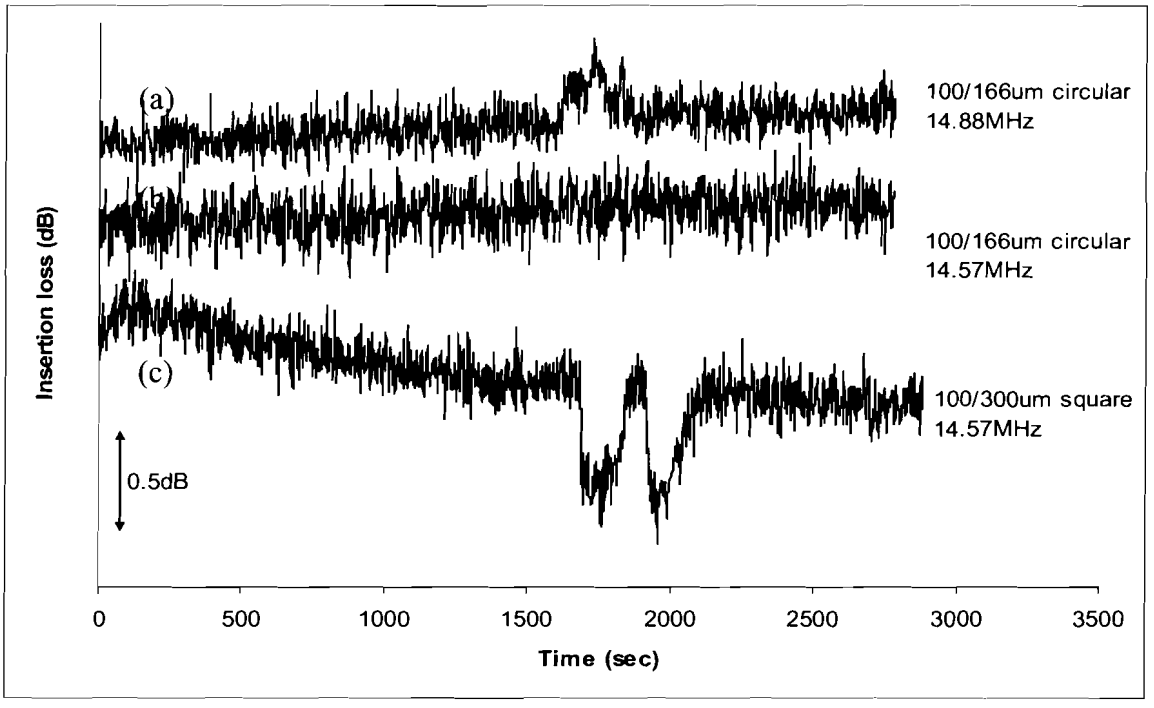

Figure 5.23. Comparison of different geometries of capillaries using a mixture of 20mM leucine and 20mM tryptophan (prepared in water). Experimental conditions: capillary, 50.0 cm, (a and b) id 100 μm, od 166 μm circular, (c) 100 μm x 100 μm square, distance to detector, 41.1 cm; applied voltage, 5kV; run buffer, 1mM sodium carbonate/bicarbonate + 0.5% SDS; frequency, (a) 14.88MHz, (b and c) 14.57MH; injection time, 60s.

But at a high-response frequency of 14.88 MHz with the circular capillary, it did show a signal, but it was like a bump, as shown in Figure 5.23a. Since the signal was not strong enough, no conclusion could be made about separation. With the square capillary, both insertion loss and phase were obtained and separation was achieved.

5.3.3 Effect of separation voltage

The optimal voltage for the separation of leucine and tryptophan were previously found to be 2kV in the circular capillary. The effect of the separation voltage was re-examined in the square capillary in Figure 5.24. In Figure 5.24a, a sample of 20mM leucine and tryptophan was separated with an applied voltage of 2 kV. In Figure 5.24b, only a shoulder peak was obtained when the voltage was reduced to 2.5 kV. In Figure 5.24c and 5.24d, with higher applied voltages (i.e. 3.5 kV and 5 kV), leucine and tryptophan were not separated at all. The use of 2 kV for optimal separation in the square capillary was consistent with the results obtained in the circular capillary.

Two main concerns in CE separation were the resolution and the analysis time. But there was a trade off between the resolution and the analysis time. When a better resolution is preferred, a lower voltage should be applied. However, the analysis time would be much longer. In this case, the diffusion of the sample plug inside the capillary would be larger, and thus the sample plug would be broadened. The spreading of the sample plug resulted in the widening of peaks and resulting in a poor resolution. On the other hand, if a high voltage was applied to the CE system, analytes would migrate faster, but the resolution might be decreased due to lack of separation time. Therefore, the applied voltage had a significant effect in the separation.

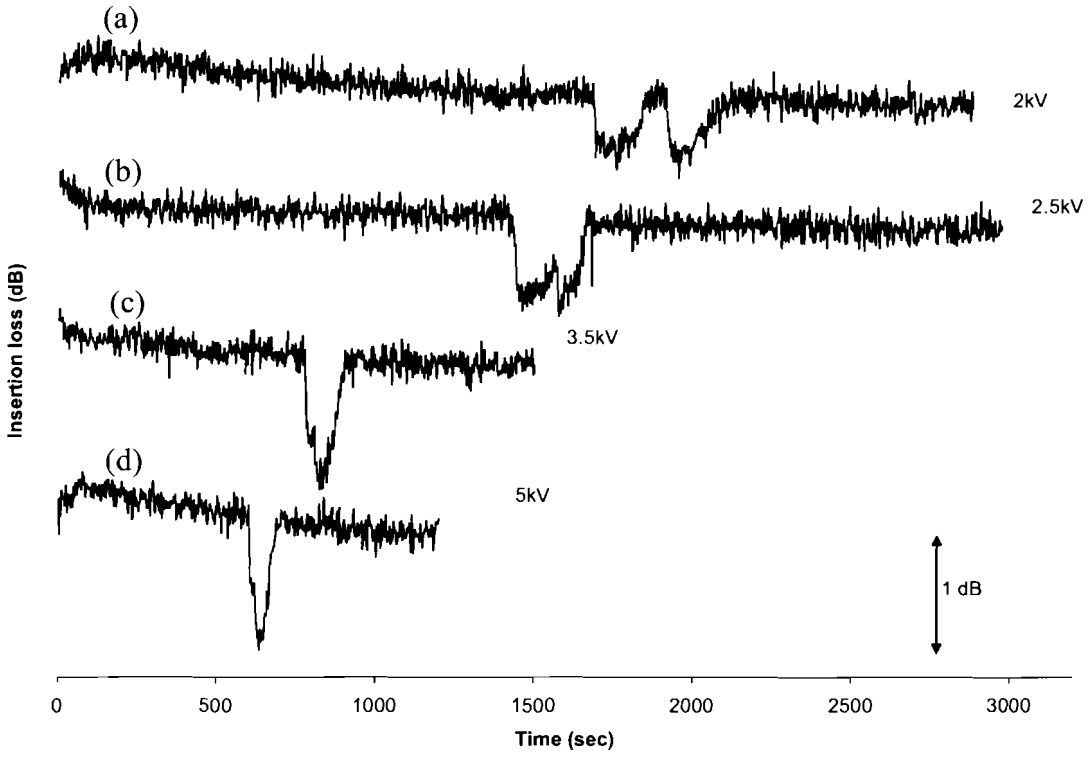

Figure 5.24. Separation enhancement of a mixture of 20mM leucine and 20mM tryptophan (prepared in water) by varying separation voltage. Experimental conditions: capillary, 50.0 cm, 100 μm x 100 μm square, distance to detector, 41.1 cm; applied voltage, (a) 2kV, (b) 2.5kV, (c) 3.5kV, (d) 5kV; run buffer, 1mM sodium carbonate/bicarbonate (c/b) + 0.5% SDS; frequency, 14.57MHz; injection time, 60s.

5.3.4 Effect of buffer composition

After the voltage optimization, the effect of the buffer composition was examined. The buffer pH was one of the considerations for successful CE separation. Since only low conductivity run buffer should be used to avoid thermal effect, only three buffers, such as sodium carbonate/bicarbonate, sodium borate, and HEPES, were used to test the effect of buffer pH on the separation. The buffer additive was 0.5% SDS for the separation of leucine and tryptophan.

Separations in these three buffer systems were monitored, as shown in Figure 5.25. In HEPES which had the lowest pH, 7.0, the separation between leucine and tryptophan was not achieved. In this case, a broad peak was obtained, which seemed to indicate a poor separation, if any. In the

case of sodium borate (pH 8.4), the separation was not accomplished either. With the sodium carbonate/bicarbonate buffer (pH 9.0) achieved a clear baseline separation. With the use of the highest buffer pH as compared with the other two run buffers, sufficient deprotonation of leucine and tryptophan occurred. This along with the interactions between SDS micelles and the analytes allowed the CE separation.

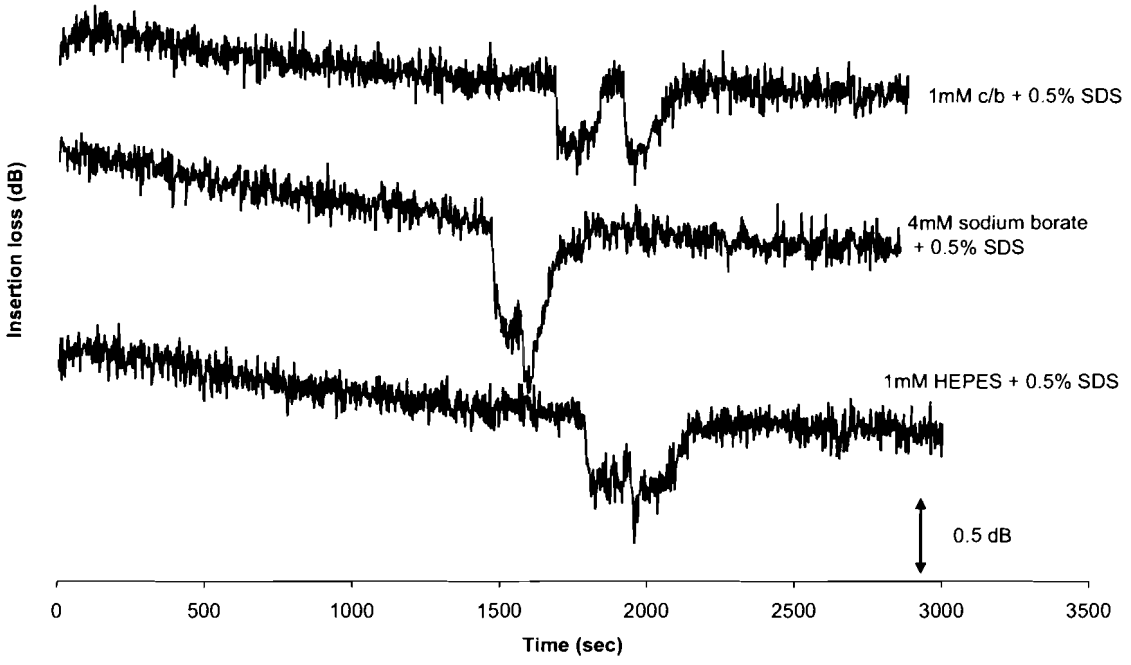

Figure 5.25. Separation efficiency under different buffer pH for separation of 20mM leucine and 20mM tryptophan. Experimental conditions: capillary, 50.0 cm, id 100 μm, od 300 μm square, distance to detector, 41.1 cm; applied voltage, 2kV; run buffer, (top) 1mM sodium carbonate/bicarbonate (c/b) + 0.5% SDS, (middle) 4mM sodium borate + 0.5% SDS, (bottom) 1mM HEPES + 0.5% SDS; frequency, 14.57MHz; injection time, 60s.

5.3.5 Effect of buffer surfactant

Other than SDS, two other commonly used surfactants, Brij 35, and Triton X-100, were also examined for CE separation. SDS is an ionic surfactant, which formed negatively charged micelles resulting in a high conductivity of the run buffer. Therefore, the concentration of SDS could not be too high; otherwise the current generated inside the capillary would be enormous, generating a large amount of Joule heat.

Brij 35 and Triton X-100 were both non-ionic surfactants. Since they do not add to the total solution conductivity, their use allowed for further increase in applied voltage and run buffer concentration in the optimization of CE conditions. Figure 5.26 shows the experiments using these three surfactants performed in a square capillary. All other experimental conditions were the same. Among these surfactants, the use of only SDS can achieve the separation of leucine and tryptophan. The use of Brij 35 and Triton X-100 could not help them because the interactions between the micelles and the analytes were either very small or the interactions between the micelles and the two analytes were very similar. In addition, the solutes in neutral non-ionic surfactant migrate in a similar manner as the free neutral solutes, resulting in no inherent separation enhancement.

Nevertheless, these non-ionic surfactants could be employed together with the charged surfactant to form mixed micelles. This method would result in the modified hydrophobicity of the micelles that migrate at a speed different from the bulk solution.

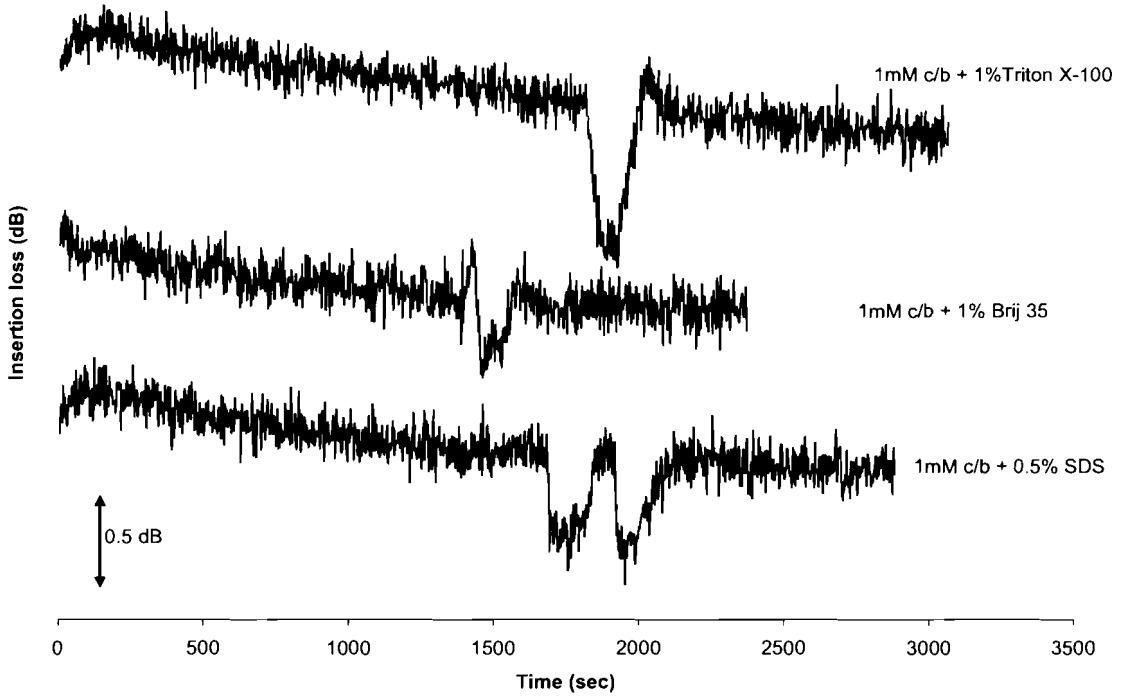

Figure 5.26. The effects of surfactants as buffer additives for the separation between 20mM leucine and 20mM tryptophan. Experimental conditions: capillary, 50.0 cm, id 100 µm, od 300 µm square, distance to detector, 41.1 cm; applied voltage, 2kV; run buffer, 1mM sodium carbonate/bicarbonate with the surfactant of (top) 1% Triton X-100, (middle) 1% Brij 35, and (bottom) 0.5% SDS; frequency, 14.57MHz; injection time, 60s.

This chapter summarised the optimization results of the acoustic wave detector coupled with the CE system by the use of pinducers, lower concentration buffer and larger diameter capillary. These experiments were carried out using both the single and CE-resolved underivatized amino acids. The effects of sample concentration, acoustic wave frequency, pH and the capillary geometry were demonstrated using leucine. Furthermore, the CE separation of leucine, histidine, proline and tryptophan were attempted with the use of the square capillary. In addition, the effects of capillary geometry, separation voltage, buffer composition and buffer surfactant were examined.

CHAPTER SIX:
CONCLUSION AND FUTURE WORK

I tried to develop an acoustic wave detector coupled to a capillary electrophoretic system. The detector is capable of detecting underivatized single and capillary electrophoretic resolved analytes. Analytes were detected by the acoustic wave method by the measurement of insertion loss.

Transducers and pinducers with higher or lower frequencies have been utilized to determine the effect on acoustic detection. 2MHz glass-horn transducers and 10MHz pinducers were used; however, pinducers achieved better acoustic wave detection. Hence, it may be advantageous to try pinducers with higher frequencies, which may further improve the detection.

With the employment of a buffer with a low concentration, Joule heat generated during CE was minimized and the interference of the thermal peak from water was eliminated. The signals obtained would be due to the presence of the analytes with better signal-to-noise ratio.

The geometry and internal diameters of the capillary were examined to deduce their effects on the acoustic detection. With the increase in capillary internal diameter, an increase in insertion loss and phase changes was observed. Altering the capillary geometry from circular to square increases the contact surface between the pinducer tip surfaces and the outer capillary wall, resulting in an increase in the signal.

The relationship between the concentration of analytes and the acoustic wave signals was determined. A positive linear relationship was obtained and the R^2 value was found to be 0.9913. By calculation, the lower detection limit was estimated to be approximately 3.5mM for leucine.

Furthermore, a positive linear relationship was obtained in the insertion loss peak ratios of the separated analytes versus their concentration ratios.

From section 2.6 on page 45, the theoretical values of the ΔIL of 50mM leucine has been estimated. The experimental value was found to be 2.2dB at 16.46MHz (see Figure 5.10) which is higher than the theoretical value (0.066dB). The change of insertion loss should be casued by non-thermal factor. This discrepancy indicates that the theory does not fully account for the experimental findings, which could be caused by the deficiency of the model used to analyse data or the presence of some systematic biases.

Further improvements in the lowest detectable amount and in peak width will be needed. These improvements will be focused on (1) the optimization of the transducer design (transducer size and shape, and acoustic wave frequency), which will reduce the angular dispersion of the acoustic wave that might have resulted in excessive peak width, and (2) the construction of the square capillary, which can increase the path length of the acoustic wave and hence enhance the detection signal. Both approaches can be realized by the integration of the acoustic detection detector in a microfluidic chip. A rectangular channel can be constructed to provide a greater path length needed for signal enhancement, but not undesirably increase the channel cross-section area and the Joule heating effect. This is essential to allow the use of various buffer additives to enhance separation resolution.

The microchip will be constructed using a polymeric material, poly (dimethylsiloxane) (PDMS). With the use of a positive relief structure of SU-8 (epoxy based negative photoresist) on a glass or silicon substrate, the microchannel can be created by molding. The ultrasonic wave detector will then be embedded in the channel. Therefore, the CE separation can be performed within the microfluidic channel for detection by the embedded detector. Figure 6.1 shows the schematic diagram of a SU-8 molding master and the alignment of the two pinducers. The channel patterns

are transferred by the photolithographic printing method on a supporting substrate (glass or silicon wafer) spin-coated with SU-8. SU-8 is cured by UV light and a positive relief is made on the substrate. Then the two pinducers are aligned opposite to each other and touch the flat surface of the SU-8 positive relief walls. Then, the PDMS pre-polymer is applied to the substrate and cured. After PDMS pre-polymer is dried, the PDMS microfluidic chip will be removed from the SU-8 relief substrate and is embedded with the pinducers.

The advantage of using PDMS chip is the use of a rectangular, rather than a circular, channel. According to Equation (66), as the internal diameter of the channel increases, the change of insertion loss increases. Therefore, a higher sensitivity would be obtained if the detection path increases. While increasing the detection path length, one does not want to increase the channel depth in order not to increase the channel current and Joule heating. Furthermore, with the embedment of the pinducers into the PDMS microchannel, a direct contact of the pinducers with the liquid phase may result in a strong acoustic coupling and significant signal improvement.

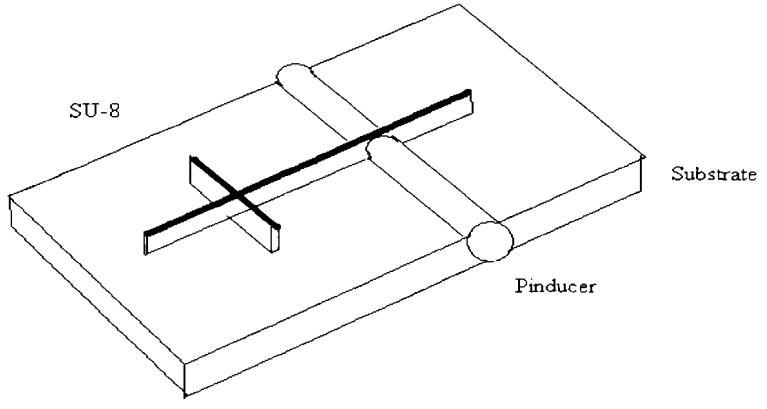

Figure 6.1. Schematic diagram of pinducers coupled with the SU8 molding master for the fabrication of the PDMS microfluidic chip

In summary, an acoustic wave detector had been coupled with the capillary electrophoresis system to detect single and capillary electrophoretically resolved underivatized amino acids. The

system was optimized by employing the pinducers to increase the wave transmission, by using a low concentration buffer to reduce the Joule heat, and by increasing the capillary diameter to enhance the detected signals. The equations that indicate the relation between the insertion loss, the capillary diameter, the operating frequency, and the ultrasonic absorption of the analyte are derived. The detection limit of leucine was estimated to be approximately 3.5 mM.

The amino acids, leucine, tryptophan, histidine and proline, were used for CE separations. With the addition of SDS in the CE buffer, a mixture of two amino acids was separated successfully. A linear relationship was obtained correlating the peak area ratio and concentration ratio. CE separations were carried out in square capillary with the optimization of various separation conditions: voltages, buffer additives, and buffer composition.

Throughout this project, one main concern is the sensitivity of the acoustic wave detection. Acoustic detection could be applied to the CE system to detect CE separated analytes, but the sensitivity was not high enough. The sensitivity of acoustic wave detection on CE is much lower than those conventional methods. For instance, the detection limits of some label-free methods were about 450 nM, 10 μM, and 32.9 μM for mass spectrometry[15], indirect chemiluminescent detection[18] and indirect fluorescent detection[19], respectively. The inadequate sensitivity of the acoustic wave detection was limited by the physical properties of the analyte, density and ultrasonic property. Since the difference between the density of run buffer and analytes was small, the signal was small too. Due to this limitation, the acoustic wave detection coupled with CE may not be sensitive enough to compete with other conventional methods. Drastic modifications and optimizations are needed to increase the detection sensitivity.

Appendix 1

Estimation of sample injection volume and plug length

The sample volume introduced into the capillary, V, could be estimated by equation (68), which is re-stated here:

$$V = \frac{\rho g H \pi (2a)^4 t}{128 \eta L} \tag{68}$$

where ρ is the sample density, g is the acceleration due to gravity, H is the height the sample is raised, a is the internal radius of the capillary, t is the time the sample is raised, η is the viscosity of the sample and L is the length of the capillary.

In our experiments, the inlet end of the capillary was raised by 13cm or 6.5cm for 100-μm-id and 250-μm-id capillary, respectively, relative to the outlet end of the capillary. The pressure difference caused the sample to be introduced into the capillary.

In the case of 250-μm-id capillary, sample volume V is estimated to be,

$$V = \frac{(0.998\times10^3 kg/m^3)(9.81 m/s^2)(0.065m)\pi[2(125\times10^{-6}m)]^4(3s)}{128(8.91\times10^{-4}kg/ms)(0.50m)} = 0.411\mu L$$

In the case of 100-μm-id capillary, sample volume V is estimated to be,

$$V = \frac{(0.998\times10^3 kg/m^3)(9.81 m/s^2)(0.13m)\pi[2(50\times10^{-6}m)]^4(60s)}{128(8.91\times10^{-4}kg/ms)(0.50m)} = 0.421\mu L$$

Therefore, the injected volume of the analyte was about 0.4μL for both 250-μm-id and 100-μm-id capillary for 3 and 60 second injections, respectively.

The sample plug length was another important parameter. If the sample plug is too long, a broadened peak will result, and the separation of the analytes would be impaired in terms of resolution. As previously reported, the sample plug length should not be longer than one tenth of the total capillary length[2,3]. The sample plug length, L_p, is calculated by equation (69) which is re-stated here:

$$L_p = \frac{4v}{\pi(2a)^2} \tag{69}$$

where v is the sample volume and a is the internal radius of the capillary.

In the case of 250-μm-id capillary, sample plug length L_p is estimated to be,

$$L_p = \frac{4(0.411\mu L)}{\pi\left(2\times 125\times 10^{-6} m\right)^2} = 0.84cm$$

In the case of 100-μm-id capillary, sample volume V is estimated to be,

$$L_p = \frac{4(0.421\mu L)}{\pi\left(2\times 50\times 10^{-6} m\right)^2} = 5.3cm$$

In addition, the sample plug lengths were 0.84cm and 5.3cm for 250-μm-id and 100-μm-id capillary for 3 and 60 second injections, respectively.

Appendix 2

Spreadsheet calculation of theoretical insertion loss curves

	A	B	C	D	E	F	G	H	I	J
1	ρ1 (kg/L)	7.8	υ1 (m/s)	2500	Z1 (kg m/L s)	19500	d1 (m)	0.004572	αs1 (m^{-1})	2.3
2	ρ2	2.2	υ2	5640	Z2	12408	d2	0.000055	αs2	2.3
3	ρ3	1.00535	υ3	1506.7	Z3	1514.761	d3	2.50E-04	t (sec)	8.8E-08
4	ρ4	2.2	υ4	5640	Z4	12408	d4	0.000055	ct (sec^2/m)	8.55E-12
5	ρ5	7.8	υ5	2500	Z5	19500	d5	0.004572	c (sec/m)	1.12E-05
6										

7	Frequency (MHz)		0.079
8	Frequency (Hz)		78740
9	k1 (m^{-1})	197.896	=2*PI()*C$8/$D1
10	k2	87.720	=2*PI()*C$8/$D2
11	k3	323.148	=2*PI()*C$8/$D3
12	k4	87.720	=2*PI()*C$8/$D4
13	k5	197.896	=2*PI()*C$8/$D5
14	Zin 1 real (kg m/L s)	19500.000	=$F$1
15	Zin 2 real	19499.333	=(C14*$F2+$F2*TAN(C10*$H2)*C14*TAN(C10*$H2))/($F2^2+(C14*TAN(C10*$H2))^2)*$F2
16	Zin 3 real	9530.116	=(C15*$F3+$F3*TAN(C11*$H3)*C15*TAN(C11*$H3))/($F3^2+(C15*TAN(C11*$H3))^2)*$F3
17	Zin 4 real	9530.207	=(C16*$F4+$F4*TAN(C12*$H4)*C16*TAN(C12*$H4))/($F4^2+(C16*TAN(C12*$H4))^2)*$F4
18	Zin1 imaginary	0	0
19	Zin2 imaginary	-87.984	=($F2*TAN(C10*$H2)*$F2-C14*C14*TAN(C10*$H2))/($F2^2+(C14*TAN(C10*$H2))^2)*$F2
20	Zin3 imaginary	-9685.302	=($F3*TAN(C11*$H3)*$F3-C15*C15*TAN(C11*$H3))/($F3^2+(C15*TAN(C11*$H3))^2)*$F3
21	Zin4 imaginary	24.549	=($F4*TAN(C12*$H4)*$F4-C16*C16*TAN(C12*$H4))/($F4^2+(C16*TAN(C12*$H4))^2)*$F4
22	exp (ikx1)	0.618+0.786i	=IMEXP(COMPLEX(0,C9*$H$1))
23	exp (ikx2)	1.00+4.82E-003i	=IMEXP(COMPLEX(0,C10*$H$2))

	A	B	C	D	E	F	G	H	I	J	
24	exp (ikx3)	0.997+8.07E-002i	=IMEXP(COMPLEX(0,C11*$H$3))								
25	exp (ikx4)	1.00+4.82E-003i	=IMEXP(COMPLEX(0,C12*$H$4))								
26	A1/A5	0.428	=(C14+$F$1)/(C14+$F$2)*(C15+$F$2)/(C15+$F$3)*(C16+$F$3)/(C16+$F$4)*(C17+$F$4)/(C17+$F$5)*IMREAL(IMPRODUCT((C22),(C23),(C24),(C25)))*EXP(-$J$1*$H$1)*EXP(-2*$J$2*$H$2)*EXP(-C27*$H$3)*IMREAL(C22)*IMREAL(C23)*IMREAL(C24)*IMREAL(C25)								
27	al (m^{-1})	0.053	=((k4/(1+(2*PI()*C8*k3)^2)+0.0000000000000318))*C8^2								
28	IL (dB)	-12.766	=10*LOG(C26^2)								

Note: Row 9-13: are calculated by $k_{nx} = \frac{\omega}{v_n}$

Row 14-17 are calculated by $Z_{in}^{(n)} = \left(\frac{Z_{in}^{(n-1)} - iZ_n \tan k_{nx} d_n}{Z_n - iZ_{in}^{(n-1)} \tan k_{nx} d_n} \right) Z_n$ (41c) and $\frac{a+bi}{c+di} = \left(\frac{ac+bd}{c^2+d^2} \right) + \left(\frac{bc-ad}{c^2+d^2} \right) i$ where a and b are the real and imaginary terms for nominator, c and d are the real and imaginary terms for denominator.

Row 18-21 are calculated by $Z_{in}^{(n)} = \left(\frac{Z_{in}^{(n-1)} - iZ_n \tan k_{nx} d_n}{Z_n - iZ_{in}^{(n-1)} \tan k_{nx} d_n} \right) Z_n$ (41c) and $phase = \arctan\left(\frac{bc-ad}{ac+bd} \right)$ where a and b are the real and imaginary terms for nominator, c and d are the real and imaginary terms for denominator.

Row 22-25 are calculated by e^{ikx} Row 26 is calculated by $\frac{A_1}{A_n} = \prod_{j=1}^{n} \frac{\left(Z_{in}^{j} + Z_j\right)}{\left(Z_{in}^{j} + Z_{j+1}\right)} e^{ik_j d_j} e^{-\alpha_j d_j}$ (46)

Row 27 is calculated by $\alpha = \alpha_{ex} + \alpha_{cl} = \frac{C \cdot f^2}{\left(1 + \frac{f}{f_r}\right)^2} + B \cdot f^2$ (26) Row 28 is calculated by $IL = 10 \log_{10} \frac{A_{1a}^2}{A_5^2}$ (59)

Acoustic wave propagation losses in solids are caused by different mechanisms such as scattering, thermal conduction and internal friction, and all these effects depend on temperature and frequency. In general, at 2 MHz, metals such as aluminum exhibit losses up to 10dB/m; other materials such as porous ceramics and plastics can have losses above 100 dB/m (VM Ristic, Principles of Acoustic Wave Devices, John Wiley & Sons 1983, Toronto, p 14).

Since in my work the capillary tube and piezoelectric pinducers remain the same and only the solution inside the capillary tube is changed, I use 10dB/m to represent the attenuation coefficients of quartz and PZT-5A for the curve fitting purpose. Note that for a 1-m path, 10dB loss indicates that A' is 0.1A in equation 34 on p29. Therefore, an α_s value of 2.3 m^{-1} was used.

Reference List

[1] Tiselius, A; **A new apparatus for electrophoretic analysis of colloidal mixtures;** *Trans. Faraday. Soc.* **1937.** 33, 524-531.

[2] Baker, D. R.; Capillary Electrophoresis, Wiley-Interscience Pub, New York, **1995.**

[3] Landers, J. P., Handbook of Capillary Electrophoresis, CRC Press, London, **1994.**

[4] Terabe S., Otsuka K., Ichikawa k., Tsuchiya A., and Ando T., **Electrokinetic separations with micellar solutions and open-tubular capillaries**, *Anal. Chem.* **1984**, 56, 111-113.

[5] Cohen, A. S., Terabe, S., Smith, J. A., Karger, B. L. **High-performance capillary electrophoretic separation of bases, nucleosides, and oligonucleotides: retention manipulation via micellar solutions and metal additives.** *Anal. Chem* **1987**, 59(7), 1021-7.

[6] Wenclawiak, Bernd W.; Hees, Torsten; Nagel, Thomas G.; **Use of capillary electrophoresis in noble metal analysis;** *GIT Labor-Fachzeitschrift.* **2004.** 48(1), 22-24.

[7] Madej, Katarzyna; Wozniakiewicz, Michal; **Application of capillary electrophoresis to analysis of tricyclic psychotropic drugs;** *Z Zagadnien Nauk Sadowych.* **2002.** 52, 52-63.

[8] Wang, Yong-mei; Yuan, Dong-xing; Deng, Yong-zhi; **Determination of vitamins B12, B6, and C in vitamin pills by micelle electrokinetic capillary chromatography;** *Xiamen Daxue Xuebao, Ziran Kexueban.* **2001.** 40(6), 1260-1264.

[9] McIntire, G. L., *Crit. Rev. Anal. Chem.* **1990.** 21, 257.

[10] Pramanick, D.; Mukherjee, D., **Molecular Interaction of Methylene Blue with Triton X-100 in Reverse Micellar Media;** *J. Colloid and Interface Sci.* **1993.** 157, 131.

[11] Swinney, K.; Bornhop, D. J., **Detection in capillary electrophoresis**, *Electrophoresis*, **2000**, 21, 1239- 1250.

[12] Jakeway, S. C.; De Mello, A. J.; **A single point evanescent wave probe for on-chip refractive index detection;** *Micro Total Analysis Systems 2001.* **2001.** 347-348.

[13] Deng, Yanzhuo; Li, Bincheng; **On-column refractive-index detection based on retroreflected beam interference for capillary electrophoresis;** *Applied Optics.* **1998.** 37(6), 998-1005.

[14] Swinney, Kelly; Pennington, Jana; Bornhop, Darryl J.; **Ion Analysis Using Capillary Electrophoresis with Refractive Index Detection.** *Microchemical Journal.* **1999.** 62(1), 154-163.

[15] Moini, M.; Schultz, C.L.; Mahmoon, H. **CE/Electrospray Ionization-MS Analysis of Underivatized D/L-Amino Acids and Several Small Neurotransmitters at Attomole Levels through the Use of 18-Crown-6-tetracarboxylic Acid as a Complexation Reagent/Background Electrolyte;** *Anal. Chem.* **2003**, 75, 6282-6287.

[16] Schultz, CL.; Moini, M. **Analysis of Underivatized Amino Acids and Their D/L-Enantiomers by Sheathless Capillary Electrophoresis/Electrospray Ionization-Mass Spectrometry;** *Anal. Chem.* **2003**, 75, 1508-1513.

[17] Qu, J.; Chen, W.; Luo, G.; Wang, Y.; Xiao, S.; Ling, Z.; Chen, G. **Rapid determination of underivatized pyroglutamic acid, glutamic acid, glutamine and other relevant amino acids in fermentation media by LC-MS-MS**; *Analyst*, **2002**, 127, 66-69.

[18] Tsukagoshi, K.; Nakahama, K.; Nakajima, R. Direct **Detection of Biomolecules in a Capillary Electrophoresis-Chemiluminescence Detection System;** *Anal. Chem.* **2004**, 76, 4410-4415.

[19] Murno, N. J.; Huang, Z.; Finegold, D. N; Landers, J. P., **Indirect Fluorescence Detection of Amino Acids on Electrophoretic Microchips;** *Anal. Chem*, **2000**, 72, 2765-2773.

[20] Lange, K.; Bender, F.; Voigt, A.; Gao, H.; Rapp M., **A surface acoustic wave biosensor concept with low flow cell volume for label-free detection**; *Anal. Chem.* 2003, 75, 5561-5566.

[21] Kundu, P.K.; Cohen, I.M.; *Fluid Mechanics*, Academic Press, New York, **2002.**

[22] Blandamer, M.J., *Introduction to Chemical Ultrasonic*, Academic Press, New York, **1973.**

[23] Zitzawitz, Neff & Mark Davids. *Physics: Principles and Problems*, New York: Glencoe, **1995,** 308.

[24] *Handbook of Chemistry and Physics*. Ohio: Chemical Rubber Co., **1967-1968**, E37.

[25] Vigoureux, P., *Ultrasonics*, Chapman & Hall, London, **1952**.

[26] Edmonds, P.D., *Methods of experimental physics vol. 19, Ultrasonics*, Academic Press: New York, **1981**.

[27] Behrends, R.; Cowman, M.K.; Eggers, F.; Eyring, E.M.; Kaatze, U.; Majewski, J.; Petrucci, S.; Richmann, K.H.; Riech, M., **Ultrasonic Relaxation and Fast Chemical Kinetics of Some Carbohydrate Aqueous Solutions** *J Am. Chem. Soc.* **1997**, 119, 2182-2186.

[28] Uhlendorf, V.; Richmann, K.H.; and Berger, W., *J. Phys. E: Sci. Instrum.* **1985**, 18, 151.

[29] Applegate, K.; Slutsky, L.J.; Parker, R.C. **Kinetics of proton-transfer reactions of amino acids and simple polypeptides;** *J. Am. Chem. Soc.* **1968**, 90, 6909-6913.

[30] Stuehr, J.E. *Investigation of rates and mechanics of reactions, Part 2, 4th ed.*, **1986**, 247

[31] Behrends, R.; Eggers, F.; Kaatze U.; Telgmann, T., **Ultrasonic spectrometry of liquids below 1 MHz. Biconcave resonator cell with adjustable radius of curvature.** *Ultrasonics* **1996**, 34, 59.

[32] Farber H. and Petrucci S. in R.R. Dogonadze, E. Kálmán, A.A. Kornyshev and J. Ulstrup eds, *The Chemical Physics of Solvation*, Elsevier: The Netherlands, **1986**, 445.

[33] Chinnery, P. A.; Humphrey, V. F., **Fluid column resonances of water-filled cylindrical shells of elliptical cross section**, *J. Acoust. Soc. Am.*, **1998**, 103 (3), 1296.

[34] P.A. Chinnery; V. F. Humphrey, **On the overlapping acoustic resonances of a fluid-filled cavity: Schlieren visualization of an insonified circular-cylindrical shell**; *J. Acoust. Soc. Am.*, **1997**, 102 (3), 1383-1387.

[35] L.M. Brekhovskikh, Wave in Layered Media, 1980, 2nd ed.

[36] V.M. Ristic, *Principles of Acoustic Wave Devices,* John Wiley & Son, **1983**, p14.

[37] Uchino, K., *Piezoelectric Actuators and Ultrasonic Montors,* Kluwer Academic, Boston, **1997**.

[38] Li, Paul C.H.; Prasad, R. **Acoustic wave detection of chemical species electrokinetically transported within a capillary tube;** *Analyst*, **2003**, 128, 706-711.

[39] N. Bilaniuk and G.S.K. Wong, "Speed of sound in pure water as a function of temperature", J. Acoust. Soc. Am. 93 (3), 1609-1612.